TECHNISCHE UNIVERSITÄT WIEN
Vienna University of Technology

DIPLOMARBEIT

Synthesis and characterisation of $CeRu_4Sn_6$ and CeBiPd single crystals

zur Erlangung des akademischen Grades

Diplom-Ingenieurin

im Rahmen des Studiums

Materialwissenschaften

eingereicht von

Judith Benkö
Matrikelnummer 01126798

ausgeführt am Institut für Festkörperphysik
der Fakultät für Physik der Technischen Universität Wien

unter der Anleitung von
Univ.Prof. Dipl.-Ing. Dr.rer.nat. Silke Bühler-Paschen
und
Dr.rer.nat. Xinlin Yan

Wien, 27.10.2020

Abstract

Strongly correlated electron systems are a rich playground to discover new quantum phenomena. This is particularly true if combined with effects of nontrivial electronic topology. The resulting properties show promise for novel quantum applications. Very interesting in this respect are heavy fermion systems. A material setting with several candidate topological heavy fermion compounds are ternary intermetallics in which a rare earth element is combined with elements of the p or d series. The physical properties of a number of them have been investigated, but many more remain to be explored. A well-developed and controllable synthesis process is a prerequirement for conducting systematic and detailed research on them. For advanced studies, single crystals are needed but their growth can be challenging. In this work the synthesis of the two intermetallic compounds $CeRu_4Sn_6$ and CeBiPd was investigated. In previous studies they were found to exhibit the Kondo effect. On the other hand the role of nontrivial topology is mostly unexplored, thus calling for further investigations. Additionally to the many experiments that were conducted in this work to adjust the parameters of the single crystal growth, some physical properties were measured to explore the composition/structure vs. property relationship.

For $CeRu_4Sn_6$ the charge carrier mobility was studied in the past. There were indications that defects in the sample could have reduced the mobility. Therefore, in this work, high-quality $CeRu_4Sn_6$ single crystals were synthesised by the floating zone method and by flux growth. However, in all measured samples the charge carrier mobility did not increase significantly compared to previous results, which might suggest that the mobility in this material is intrinsically low. For CeBiPd previously reported resistivity measurements showed a large spread of results, which prompted the question whether the physical properties are highly influenced by the composition. In this work CeBiPd single crystals were synthesised using flux growth. A number of relationships between the stoichiometry of the material and the resulting properties could be revealed. However, to achieve a full control of the composition and thus the properties will require further investigations. The physical property measurements in this work showed that instead of a superconducting transition previously reported in polycrystalline CeBiPd samples an antiferromagnetic transition takes place.

Zusammenfassung

Elektronisch hochkorrelierte Materialien zeigen eine Fülle interessanter Quanteneigenschaften. Dies ist besonders dann der Fall, wenn die starken elektronischen Korrelationen gepaart mit nichttrivialer Bandtopologie auftreten. Derartige Materialien zeigen überraschende Eigenschaften, die sie interessant für neuartige Quantenanwendungen machen. Eine Materialklasse, in der solche Eigenschaften beobachtet wurden, sind Schwere-Fermionensysteme. Ternäre intermetallische Verbindungen mit einem Element der Seltenen Erden und zwei Elementen der *p*- oder *d*-Reihe sind ein vielversprechender Ausgangspunkt. Für die Untersuchung dieser Materialien ist es essenziell, über ein gut kontrollierbares Syntheseverfahren zu verfügen. Insbesondere die Herstellung von Einkristallen ist schwierig, aber dennoch notwendig, um eingehende Studien der Materialeigenschaften zu ermöglichen. $CeRu_4Sn_6$ und CeBiPd sind zwei solche ternäre Verbindungen, bei denen der Kondoeffekt nachgewiesen werden konnte. Um das spärliche Wissen um ihre Eigenschaften erweitern zu können, wurden in dieser Arbeit umfangreiche Experimentreihen über ihre Syntheseverfahren aufgesetzt. Anschließend wurden diese durch Messungen einiger physikalischer Eigenschaften ergänzt.

$CeRu_4Sn_6$-Einkristalle wurden bisher im Zonenschmelzverfahren hergestellt, um unter anderem ihre Ladungsträgerbeweglichkeit zu messen. Aufgrund der Vermutung, dass die Qualität dieser Kristalle durch das verwendete Verfahren durch Defekte limitiert ist, wurde in dieser Arbeit sowohl durch Erweiterung des Zonenschmelzverfahrens als auch durch das Flussmittelverfahren versucht, die Qualität der hergestellten Einkristalle zu verbessern. Allerdings konnte in den so produzierten Proben bisher keine signifikante Erhöhung der Ladungsträgerbeweglichkeit nachgewiesen werden. Dies lässt den Schluss zu, dass die niedrige Beweglichkeit eine intrinsische Materialeigenschaft ist. An CeBiPd-Einkristallen wurden zuvor schon Untersuchungen des elektrischen Widerstandes durchgeführt, allerdings schwankte der gemessene Widerstand stark von Probe zu Probe. Durch das Flussmittelverfahren wurde in dieser Arbeit versucht, die Zusammensetzung der hergestellten Proben genau zu kontrollieren, um herauszufinden, ob es einen messbaren Zusammenhang zwischen der Zusammensetzung und dem elektrischen Widerstand gibt. Einige interessante Zusammenhänge konnten aufgespürt werden. Um einen völlig reproduzierbaren Syntheseweg zu etablieren, sind aber weitere Untersuchungen nötig. Eine neue Entdeckung ist ein antiferromagnetischer Übergang bei niedrigen Temperaturen.

Acknowledgements

Firstly, I would like to thank Dr. Xinlin Yan for generously sharing his knowledge with me and for his prompt availability whenever I needed his support. I would also like to thank Prof. Silke Bühler-Paschen for giving me the opportunity to be a part of her research group and offering me a place in such an interesting project. I am grateful to Dr. Gaku Eguchi for helping me with setting up and conducting some of the measurements, even teaching me background knowledge; and to Prof. Andrey Prokofiev for enlightening discussions of some puzzling material behaviours, sharing his vast expertise with me. I would like to thank Mag. Snežana Stojanovic for her help in learning to operate several different devices in several different labs. Many thanks to the SEM technicians Monika Waas and Robert Svagera for their enthusiasm with analysing my samples. Also, I am grateful to Dr. Diego Zocco and Diana Kirschbaum for sharing their findings with me on the samples that I grew.

Naturally, I would like to thank my family who cultivated my interest in science from the beginning of my life and then patiently supported me throughout my study years. Big thanks to all my friends in Austria, Sweden and elsewhere who continuously offered me encouraging words. And finally, I am grateful to Bodor Enikő who has always had faith in me in all the years I have been fortunate enough to know her.

Contents

1 Introduction

The characterisation of new materials requires high-quality single crystals. Although many different techniques have been developed for their synthesis over the last decades, each new material needs its own adjustments of the methods. A great number of influencing factors can be varied in the growth process. In flux growth, for instance, these include the temperature profile and initial composition. Additionally, there are several challenges such as unwanted secondary phases or undesirable growth shapes that can inhibit a successful growth experiment. This makes crystal growth a very complex task.

Strongly-correlated electron systems are at the forefront of research in condensed matter physics. A materials class where correlations can become extreme are the heavy fermion compounds. They typically contain a rare earth element with incompletely filled $4f$ shell and, in addition, elements of the p or d series. Ce-based compounds are the simplest example: Ce has one unpaired $4f$ electron. In a metal, it tends to interact with the conduction electrons via the Kondo effect. This leads to strongly renormalised bands, with very heavy quasiparticle masses, at low temperatures. In some cases, an energy gap at the Fermi level results from the interaction, defining the class of Kondo insulators. In order to investigate these, knowledge about the synthesis of high-quality single crystals of these materials is needed.

One compound that was studied in this work is $CeRu_4Sn_6$. Previous studies have come to the insight that additionally to being a Kondo insulator, it might also show unusual topological properties [1, 2]. Its physical properties have been described in several reports, including [3], [4], [5] and [6]. A feature that makes it stand out among other Kondo insulators is its tetragonal and quasi-cubic crystal structure [7, 8]. This structure can also be described as a cage compound. In this work, an attempt was made to answer the following question: Can the charge carrier mobility be significantly enhanced by improving the quality of the $CeRu_4Sn_6$ samples? Two different crystal growth methods were investigated. Firstly, the floating zone method was upgraded by an annealing process. Secondly, a series of flux growth experiments was conducted to find the ideal parameters for the growth of large single crystals. Selected samples were used for measurements of electrical transport properties.

The second compound studied and described herein is the half-Heusler compound CeBiPd. Only a few reports on this compound have been published previously [9–12]. Ref. [9] reports a superconducting transition in a polycrystalline sample. In the same study indications for the presence of Kondo properties were found. In [12], the single crystal growth and physical properties of CeBiPd were investigated. The obtained resistivity curves showed some differences and so did the compositions of the samples. In this work, the following question was posed: Is there a correlation between the slightly varying compositions and very different resistivity curves exhibited by previously studied single-crystalline CeBiPd samples? Polycrystalline samples were produced by induction heating that gave useful information for subsequent flux growth experiments. A series of the latter experiments was conducted in an attempt to produce samples containing different amounts of Pd. Some samples were selected for physical property measurements.

In Chapter 2, some basic information on the materials and their synthesis is provided. In Chapter 3, the various analysis methods used for investigations of the composition as well as physical properties of the samples are described. In Chapter 4, the research done on $CeRu_4Sn_6$ and in Chapter 5 investigations on CeBiPd are presented. In the last Chapter a summary and an outlook are given.

2 Chemical basics

2.1 Crystalline materials

2.1.1 Atomic structure

Crystalline materials are distinguished by their long-range atomic ordering. A crystal structure is made up of a lattice and a basis. The lattice describes the positions where the elements of the basis (one or more atoms) can be located. Different lattice types have different amounts of symmetry elements and thus complexity. The smallest entity of the lattice that is repeated periodically is the unit cell. The size of the unit cell is represented by the lattice parameters.

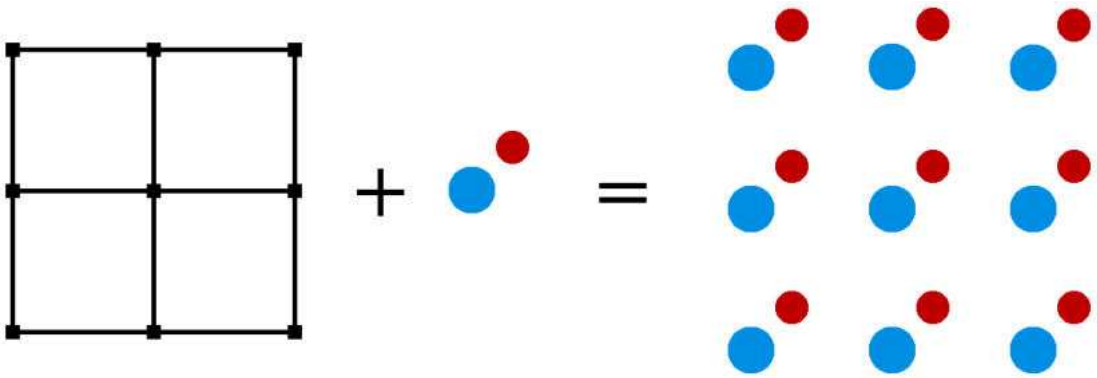

Figure 2.1: A lattice and a basis make a crystal structure

The crystal structure is determined by the interactions of the elements and influences the electronic structure. By this, it also influences the properties of the material.

Additionally there can be defects in a lattice. One type of defect is the substitution of an atom of one type by another type. Another defect is a vacancy, where an atom is missing. There can also be an additional atom between the regular atom positions, which is called an interstitial. All these defects influence the physical properties to some degree, depending on their type and amount. With a high enough deviation from the regular structure the overall composition of the material can be altered by defects.

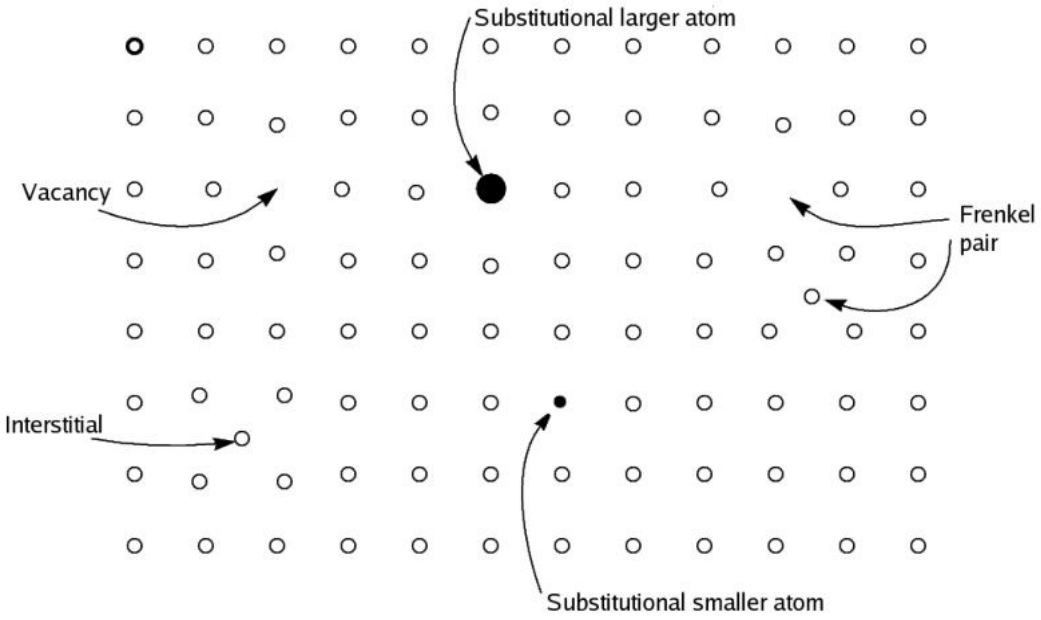

Figure 2.2: Defect types

Lattice structures can be very simple like a primitive cubic structure, but also very complex with different elements and complicated structures. Materials that have structures with differences between the directions and thus also have different properties depending on the direction are called anisotropic. An example for more complicated structures are cage compounds, where one type of atom is in the centre of a cage-shaped structure built by the other atoms.

2.1.2 Ternary intermetallic compounds

The materials studied in this thesis are intermetallic compounds made up of three different elements. The different kinds of atoms cause many different interactions which can result in the emergence of complex phenomena like the Kondo effect or the coexistence of different behaviours. There is a large number of compounds in this material class that can be synthesised.

Material properties such as excessive sensitivity to air or high brittleness can lead to difficulties in studying it. Despite this, strong efforts are being made to investigate promising members due to the interesting properties. Often, their synthesis is also challenging.

Some of these compounds can occur as materials with so many defects that a crystal becomes detectably non-stoichiometric, that is, the element ratios manifestly deviate from the normal stoichiometry. An example is $CeBiPd_{1-x}$, in which a detectable amount of Pd atoms is missing from a CeBiPd crystal. Non-stoichiometric materials give favourable conditions to investigate the correlations between the composition and the physical properties.

The possible phases in a three-component system can be depicted in a ternary phase diagram (such a phase diagram can be seen in figure 4.17 on page 32). Each point represents a compound by the atomic percentages of its components. The connecting lines between these points are called tie lines and represent regions where the two different phases that are at either end of the line coexist. An area of a triangle delimited by three tie lines is a region that contains three different phases found at each corner of the triangle.

2.1.3 Microstructure

The microstructure of a material is the structure on a polished surface made visible by a microscope. It contains information about the phases and grain boundaries between the crystallites in a sample as well as bulk defects such as inclusions or cracks. Crystallites are parts of the volume and consist of a continuous lattice. A solid containing several crystallites is called polycrystalline. A piece that consists of just one crystallite, that is, it has a continuous lattice throughout its whole volume, is called a single crystal. A sample's crystallinity and the orientation of the crystallite(s) can be investigated by performing a metallographic or a Laue measurement. Additionally, by using metallography, bulk defects can also be discovered. In figure 4.1 on page 20 a metallographic picture shows cracks in the sample.

2.2 Crystal synthesis

In this work different techniques were used for sample preparations. Techniques for the production of both single- and polycrystalline samples were used.

2.2.1 Synthesis in the high frequency (HF) furnace

In the induction crucible furnace (see figure 2.3) metallic materials are melted and subsequently cooled down to produce a polycrystalline piece. The sample is placed in a pit in a water-cooled copper tube. The copper tube is enclosed in a quartz tube which is evacuated and rinsed with Argon several times. The following melting process is done in an Argon atmosphere. A solenoidal induction coil is placed around the sample and the quartz tube. When turning on an AC current in the coil, an alternating magnetic field is produced in the conducting sample material inside the coil. This field induces eddy currents in the material. The resistance causes the sample to heat up.

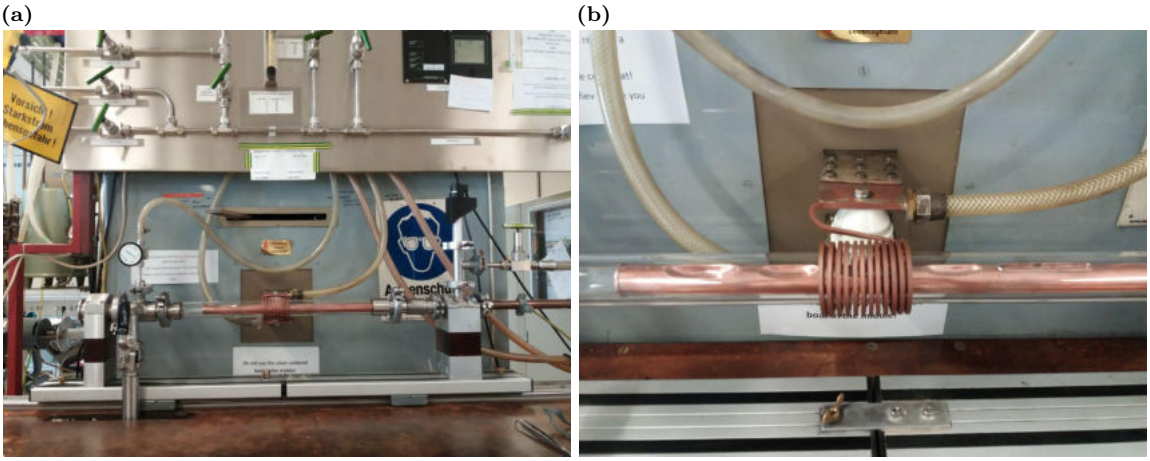

Figure 2.3: (a) HF furnace with (b) a close-up of the copper tube and induction coil

The HF furnace at the Institute of Solid State Physics at the Vienna University of Technology (IFP-TU Wien) is powered by a Hüttinger generator (30kW, 600 kHz). The copper tube that functions as a crucible has several differently-shaped pits. The shape of the resulting piece can be chosen to be ellipsoidal or rod-shaped. The homogeneity of the composition of the resulting sample can be influenced in different ways. The order in which the elements are added and the

applied power can be important factors. An improvement of the homogeneity can be achieved by doing several iterations of breaking the resulting piece and remelting after turning them around. However, phase-purity is not guaranteed with this method.

2.2.2 Single crystal growth from flux

In this method all components of the desired compound and the flux are mixed in a crucible, heated up to high temperatures in order to melt them and then cooled down according to a specified cooling rate to allow the growth of single crystals out of the melt. A low cooling rate allows stable crystal growth. In the course of this work this method was improved and refined for $CeRu_4Sn_6$ and $CeBiPd_x$, $x \approx 1$.

Preparation procedure

For the preparation of a sample from the elements the required masses of the sample components and the flux are calculated from the molar ratios or volume percentages and weighed out. Then the components can be melted together in the HF heater to facilitate melting in the later heating period. Subsequently they are sealed in an Al_2O_3 crucible in an evacuated quartz glass tube. Then the tube is put in a furnace which is programmed to heat up the sample with a specified rate, hold the high temperature for a specified time and then cool it down again with a low rate.

Two different furnaces were used in this step. When using the box furnace (see figure 2.4a), after finishing this temperature programme the sample is removed from the furnace and quickly put in a centrifuge to spin off the still liquid flux. When cooling down the sample to room temperature it solidifies. The grown crystals are kept separate from the spun-off flux in the quartz tube by use of quartz wool and can be accessed by breaking open the quartz tube after cooling.

The vertical furnace (see figure 2.4b) was used when cooling rates needed to be specified with 0.1°C/h accuracy. This furnace exhibits a temperature gradient depending on the vertical sample position (see figure 2.5). When the temperature programme is finished the samples are removed from the furnace. Because here the removal takes a longer time the samples cannot be put in the centrifuge while the flux is still liquid. Therefore they have to be reheated in the box furnace before decanting.

The as-grown constitution of a sample batch can have varying appearances. It may be made up of just one crystal that is several mm big or of several crystals of different sizes and compositions, depending on how refined the growth process is for the desired compound. Some crystals exhibit irregular shapes like in the case of hopper growth (see figure 2.7). The shapes of crystals that were grown under ideal circumstances and are thus regularly shaped indicate the lattice type of the compound. Some of the batches contained remains of the flux and/or the quartz wool even after the decanting process, which was, however, not found to influence the crystals themselves.

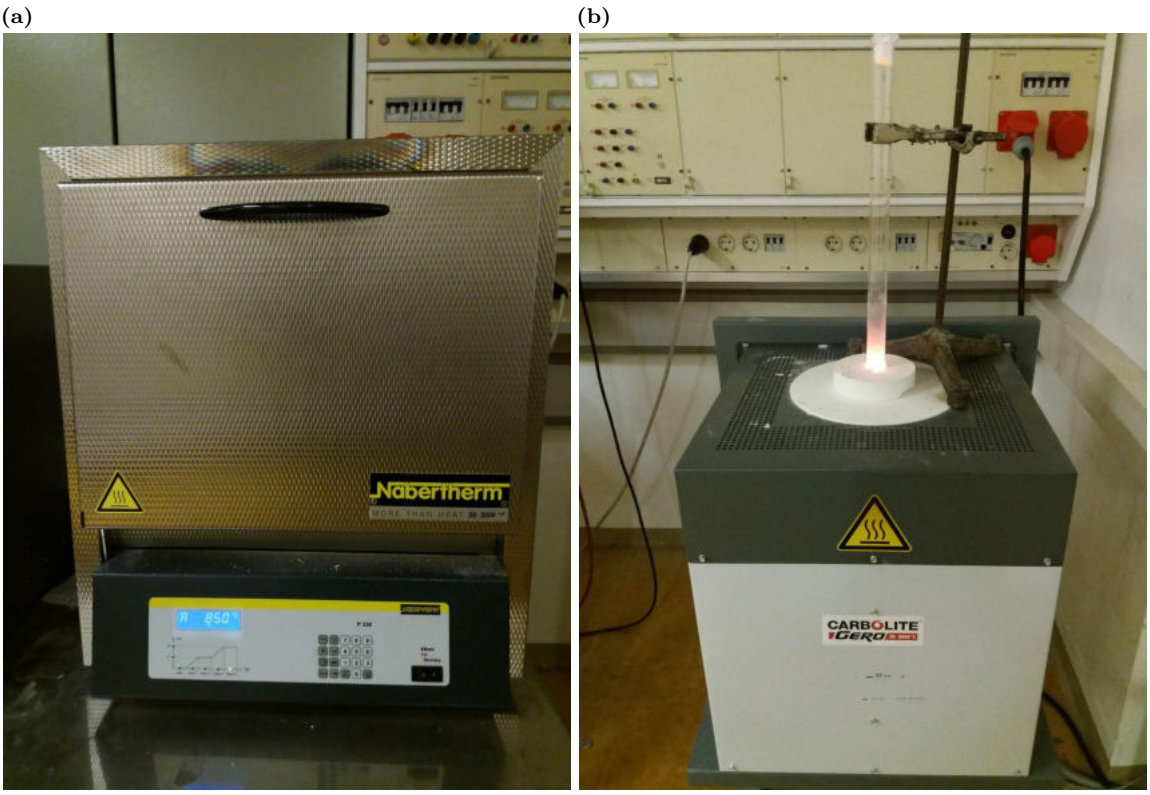

Figure 2.4: (a) Box furnace and (b) vertical furnace

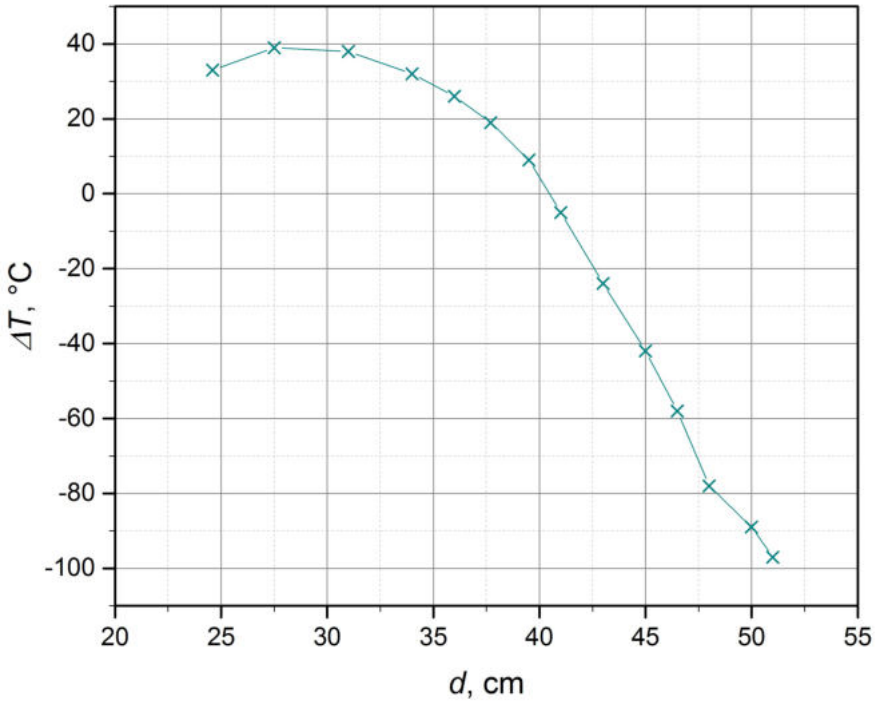

Figure 2.5: The temperature difference between the measured and the programmed temperature (= 600°C) as a function of depth in the vertical furnace.

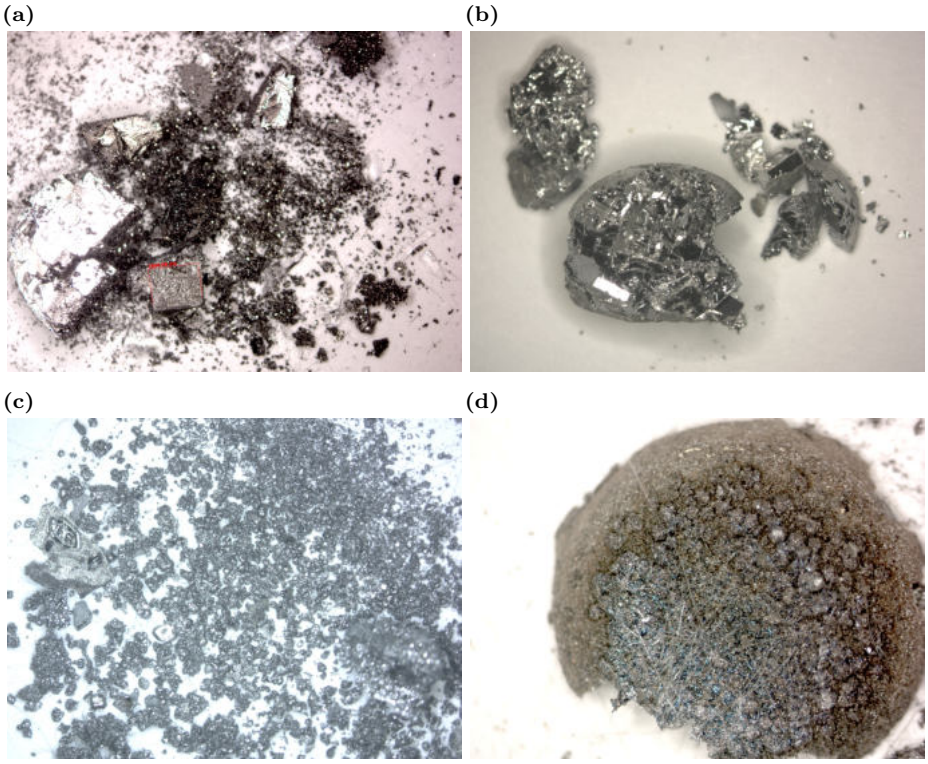

Figure 2.6: Examples of as-grown single crystals in different sample batches; (a) is from a CeBiPd growth experiment and (b), (c) and (d) are from $CeRu_4Sn_6$ growth experiments.

Growth mechanisms

Many factors influence the growth of crystals in the crucible. Some factors concerning the composition of the solution are: its viscosity, the ratio between solute and flux and whether or not there are seed crystals of the desired compound present. Concerning the temperature sequence the following are important factors: the cooling rate, the decanting temperature and temperature instabilities.

A key variable in crystal growth is supersaturation. It describes the willingness of crystalline material to form in a certain ratio of material to flux and at a certain temperature. It is influenced by both solution composition and temperature sequence. It has to be kept at an ideal value to enable the growth of high-quality crystals. If the supersaturation is too low, nucleation cannot happen. If it is too high, many small crystals will grow instead of fewer big ones. Additionally, this can lead to hopper growth (see figure 2.7). New layers nucleate on top of incomplete layers, forming a step pattern. At an even higher supersaturation dendritic growth can happen. For appropriate supersaturation the atoms attach preferably at a kink or edge which results in a layer by layer growth. Spiral growth caused by a screw dislocation continually provides such a kink and thus promotes smooth surfaces. Growth that is faster than the diffusion of the flux away from the crystal surface presents another problem. In this case inclusions of flux material are likely to develop. [13, 14]

When the composition of a compound changes with the temperature, a single crystal of this compound may show a composition gradient in a radial direction due to the temperature change during the growth process. In this case the measured composition of a surface depends on the depth the crystal has been polished to.

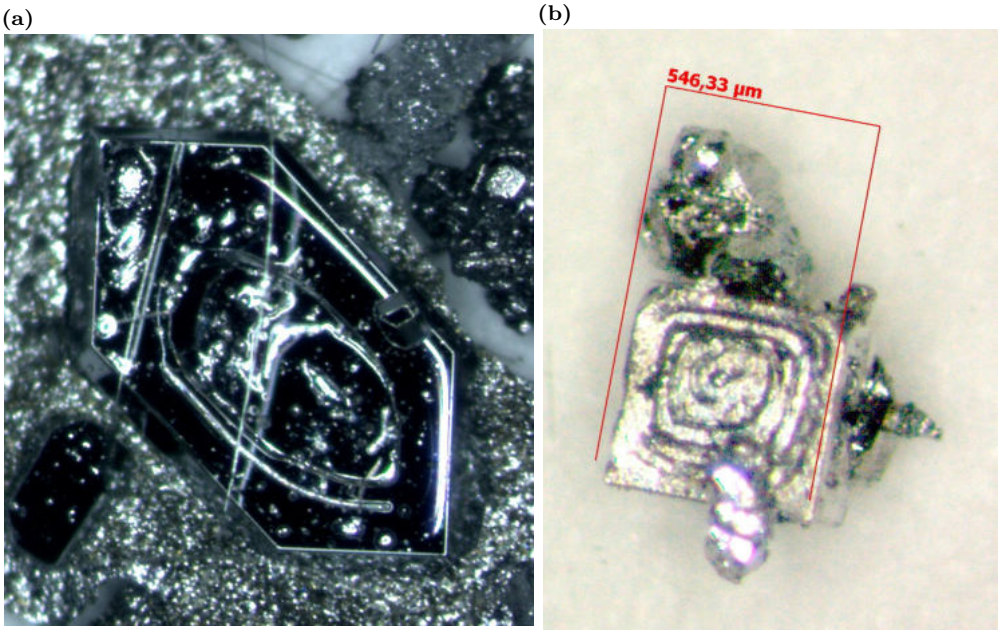

Figure 2.7: Unfavourable crystal shapes from $CeRu_4Sn_6$ growth experiments

Flux

A flux is used as a solvent for single crystal growth. For incongruently melting compounds it enables growth at lower temperatures than the decomposition temperature of the compound [15].

Low-melting materials are therefore suitable as flux, though they also evaporate easily. For this reason the solution needs to be sealed during the heating process.

Flux materials can be either other materials than the elements in the required compound or elements of the compound (self-flux). They can also be a combination of several elements. The choice of flux material also depends on its relation to the other materials involved in the growth process. It should not tend to be built into the structure of the desired compound. Also, the difference between the melting temperature of the flux and the melting temperature of the other elements has to be sufficiently large to facilitate their separation after the growth process.

Since the flux functions as a solvent, its mass should be about ten times the mass of the alloy components. One of the goals for using a flux is to lower the melting temperature of the mixture. Heating up the mixture to a high temperature and holding that temperature for several hours facilitate the complete melting of all components and their mixing. After crystal growth there are several options for cleaning the product of the flux. One method is decanting the flux by placing the sample upside-down in a centrifuge while the flux material is still liquid and spinning it off from the produced samples. Another method is placing the sample in acid for some time until the flux material is dissolved.

Choosing the temperature programme

The temperature programme of the heating and cooling process has an impact on the result in several ways. The highest temperature has to be held long enough for all the components to melt completely and mix homogeneously. The cooling rate influences the crystal growth itself. If it is high, the result will be rather many smaller crystals than fewer large ones. An experiment with a high cooling rate can be used for a quick analysis of the compounds yielded by a certain starting composition. On the other hand, a lower cooling rate extends the duration of the experiment. Finally, the finishing temperature has to be in the range well below the freezing point of the compound and above the freezing point of the flux. Considering all these factors most experiments were conducted using a simple heat up – hold – cool down – hold type sequence. A few differing sequences were also tried using varying cooling rates in different temperature ranges. Another aspect to consider is the fact that quartz glass starts disintegrating at temperatures close to those needed to melt the constituent material. For this reason the highest temperature that was used in the experiments in this work was 1150°C.

2.2.3 Single crystal growth using the optical furnace floating zone method

Two polycrystalline rods of the growth material were synthesised in this work in the HF furnace. One of them which operates as the seed rod is placed below the second one which is the feed rod. Between the two, a flux material may be added in order to enhance the crystal growth process. At the interface of the two rods a joined molten zone is created by heating. Four curved mirrors around the sample focus light to a focal point to optically heat the area where the rods touch. This liquid zone is only held together by the surface tension of the liquid. Throughout the process the two rods are moved downwards to change the relative position of the melting zone on the rods. When a part of the feed rod enters the melt zone it becomes liquid. At the same time the seed rod is pulled out slowly from the molten zone, forming a single crystal. The growth is ended by the separation of the two rods.

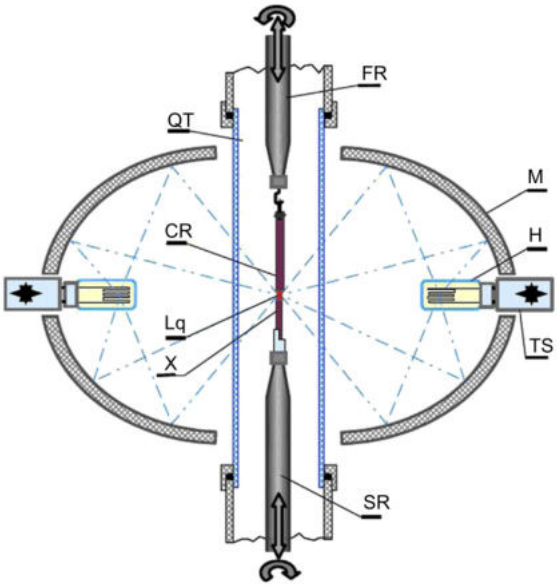

FIGURE 8.1.1 The schematic drawing of the optical floating zone. M, elliptical mirror; H, halogen tungsten lamp; TS, x-y-z micrometer translation stage for filament adjustment; QT, vitreous silica tube (quartz glass); FR, upper translation/rotation rod; CR, ceramic "feed rod"; Lq, liquid bridge "floating zone"; X, "seed rod" and crystal; SR, lower translation/rotation rod.

Figure 2.8: Schematic representation of an optical furnace taken from [16]

3 Analysis methods

A variety of methods was used in the course of this work for the analyses of phases, structures and compositions as well as for physical properties. In the following an overview of these methods is given.

3.1 Powder x-ray diffraction

The powder x-ray diffraction method is used for determining the phase constitution of samples. By the Rietveld refinement method parameters of the crystal structure in each phase such as the lattice parameter can be computed from the resulting intensity pattern. In this work this method was used for nearly all samples.

Theory

The analysis method of powder x-ray diffraction (XRD) is based on Bragg's law:

$$\lambda = 2\, d_{hkl} \sin\theta, \tag{3.1}$$

where λ is the wavelength of the x-rays, d_{hkl} is the distance between lattice planes in the investigated crystal and θ is the angle between the incoming x-ray and the lattice plane (see figure 3.1).

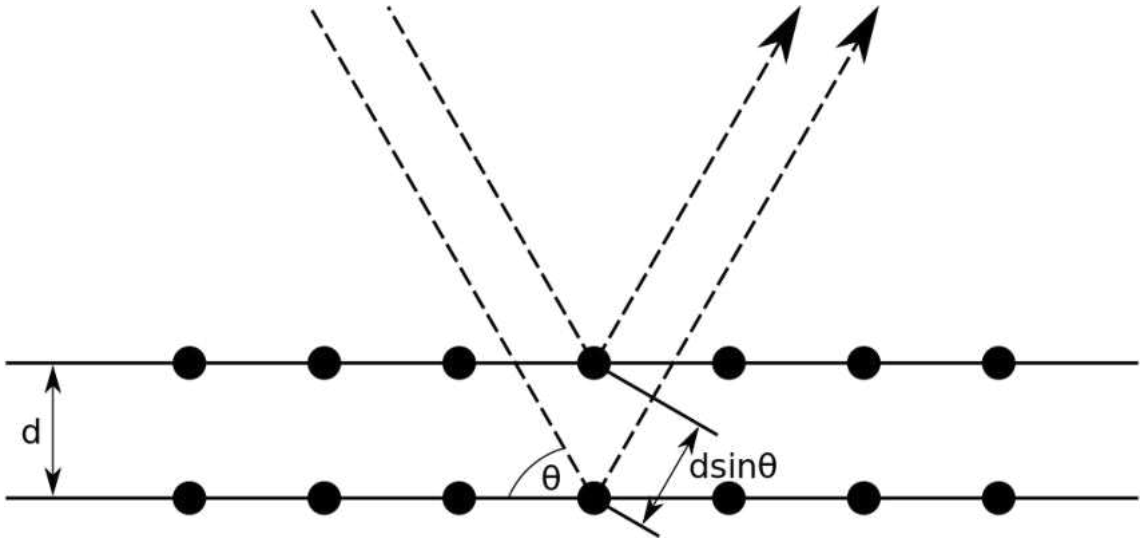

Figure 3.1: Illustration of Bragg's law

In the powder diffraction method the wavelength of the x-rays is constant (in the present work, we used Cu $K_{\alpha 1}$, $\lambda = 1.54056\,\text{Å}$), and the intensity is measured as a function of angle (normally $2\theta \leqslant 100°$). The result of such a scanning of the angles is an intensity spectrum as a

function of the angle; intensity peaks appear when Bragg's law is fulfilled. The positions of the peaks are connected to the structure type and the lattice parameters, and the peak heights are related to the site preferences and occupations. [17]

Sample preparation and equipment

For performing an XRD measurement of a sample synthesised by flux growth some crystals are selected under the microscope. If needed only crystals of a given shape are selected to find out the phase constitution. These crystals are crushed to a powder using a mortar and the powder is then put onto a sample carrier which can be inserted in the x-ray diffractometer.

Two diffractometers were used in the course of this work: a Guiner-Huber image plate system at the Faculty of Chemistry of the University of Vienna and a Philips/PANalytical X'pert^2 Pro-MDP Powder Diffractometer at the TU Wien. Due to the measurement quality the patterns acquired by the latter can only be refined in respect to the peak positions.

Rietveld refinement

After acquiring an x-ray diffraction data set the resulting pattern can be compared with known patterns to find out which phase(s) is (are) contained in the sample. Then the structural parameters of each phase can be refined by the so-called Rietveld refinement. A good initial structural model is necessary in order to avoid refinement divergence or a false minimum (instead of a global minimum). A previously identified structure model is used to fit the measured data by a least-squares method. Hereby the parameters of the sample, most importantly the lattice parameter, are computed. [18, 19]

3.2 Metallography

Metallography is a visual analysis method to study the microstructure of a crystal surface. The sample is prepared by grinding and polishing to obtain a smooth surface. Then the microstructure can be made visible by various means. When looking for different phases the surface can be etched so that different softnesses lead to different elevations on the surface. Phases can then be recognised through a microscope by different colours. When looking for grain boundaries, polarised light can be used to find the grains with different lattice directions on the polished surface. In the microscope the angle of an analyser can be changed to cause the grains to reflect or transmit different amounts of light. However, this method can only give information on the surface that is observed, and not on the volume of the sample.

3.3 SEM imaging and SEM-EDX

Scanning electron microscopes (SEM) are used to produce images of the microstructure of a material. Information on phase constitution and topography of the surface can be gathered.

A focused and high-energy electron beam (primary electrons) is directed at the sample surface. The interaction of the electrons and the sample atoms causes several different emission processes in the sample surface.

The following are used in SEM-EDX imaging: [20]

- The primary electrons can be scattered and deflected from the surface and detected as backscatter electrons (BSE). The amounts of these electrons can be depicted as an image

of the surface. In this image different elements or phases are depicted by a difference in brightness.

- The electron beam can cause sample electrons to leave the surface as secondary electrons (SE). They can be detected to understand the surface topology.
- When an inner shell electron is emitted, an outer-shell electron takes its place. In this process a characteristic X-ray is emitted. By detecting all X-rays of different energies (energy-dispersive X-ray spectroscopy, EDX), the elemental composition of the specimen is identified. [21]

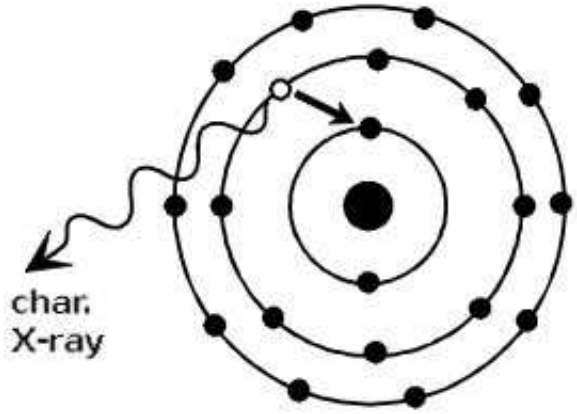

Figure 3.2: The emergence of a characteristic X-ray

Some error sources and limitations of this method are the electron beam spot size, the difficulty of detecting light elements and the strict conditions for the sample which should be thick with a well polished surface strictly perpendicular to the electron beam. The resolution can be slightly varied by adjusting the accelerating voltage and hence spot size of the electron beam.

To prepare the sample, in most cases it has to be polished to have a surface that is as smooth as possible. The prepared sample is attached to a special sample holder with a carbon adhesive tape, keeping the surface of interest perpendicular to the electron beam.

3.4 Laue measurements

The Laue method is used to test whether a sample is a single crystal or not and to orientate a single crystal to a desired direction.

The sample is illuminated with x-rays of a spectrum of different wavelengths. Diffraction leads to constructive interference to certain points on a photoplate, where this pattern is captured. Constructive interference happens when Bragg's law (3.1) is fulfilled by a combination of fitting values of the wavelength of the x-ray, its incident angle and the plane distance in the crystal.

This results in an array of dots in a pattern specific to the crystal structure. The dots are arranged on sectors of ellipses. Each ellipse corresponds to a crystal plane, and each dot at an intersection of ellipses corresponds to a crystallographic direction. If there are several different structures in the illuminated area the patterns overlap in the result. In the case of a polycrystalline sample a white patch in the centre of the image can be seen.

Additionally, the orientation of the crystal is reflected in the position of the dots. From a captured image and the structural data of the material the orientation can be determined with the program OrientExpress 3.4. The program compares the position of the dots to calculated patterns.

A problem with this can be that the patterns of some directions in a crystal look very similar. This can make it impossible to determine the orientation of a crystal using only a Laue measurement. Another limit of this method is the small volume that is studied, therefore investigating a large piece needs a series of measurements in different directions to determine if it is one single crystal or a combination of several crystals.

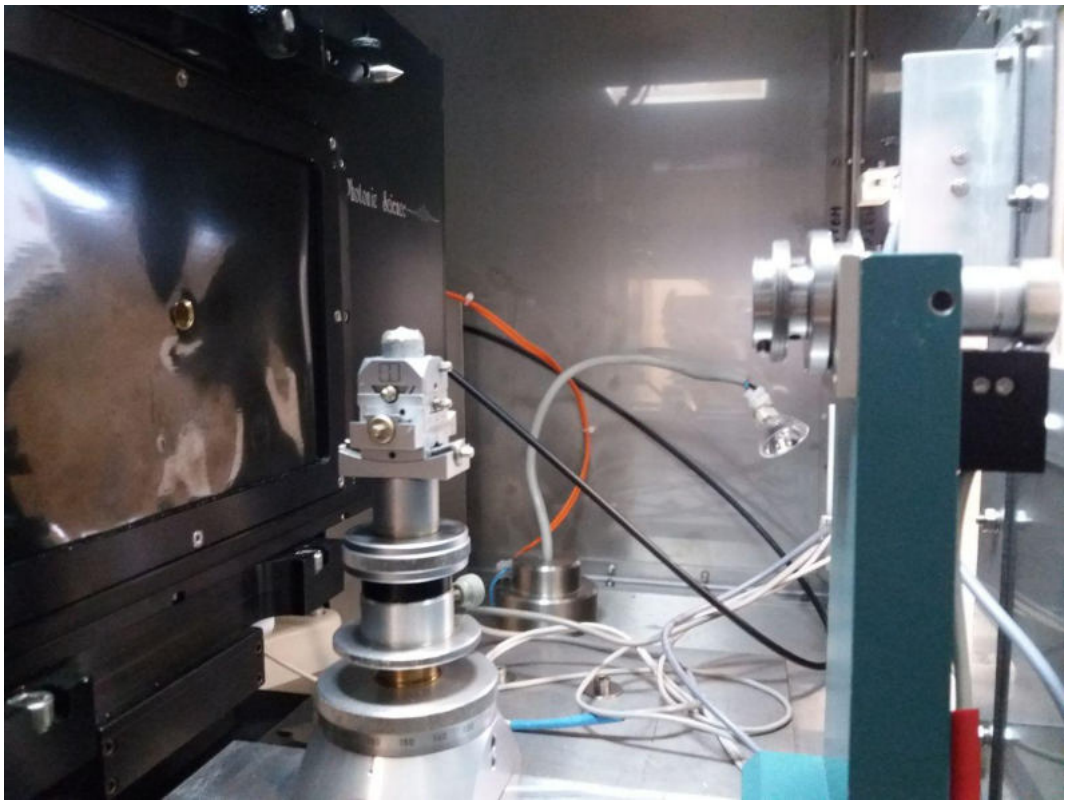

Figure 3.3: Interior of the Laue device

3.5 Low-temperature resistivity measurements

One of the two devices for measuring the resistivity in this thesis is the so-called „GUNDI“ which was built at the IFP-TU Wien. The measurement principle is to use a standard four-point setup. A single-phase sample is prepared by shaping it into a cuboid and polishing its surface. Four gold wires (25 or 50 μm in diameter) are connected to the sample by spot-welding or silver paint (depending on the material's properties) and the sample is then attached to a sample holder by GE varnish. The cryostat can be cooled down to 2 K using liquid He and pumping on it. The resistivity curves used in this thesis were taken from the measurements during the warming up process. One source of measurement error comes from the uncertainty in the geometric measurements of the sample.

3.6 Hall-effect measurements

Another kind of measurement that is conducted to obtain knowledge about the electrical transport properties of a material is a Hall-effect measurement. In this work these measurements were conducted using a Quantum Design Physical Property Measurement System (PPMS) 6000. This is the second device with which the electrical resistivity was measured.

Theory

When a current is applied to a sample situated in a magnetic field, a voltage will be created in the direction perpendicular to the current and the magnetic field. This effect is called the Hall effect.

The trajectories of the charge carriers in the current are changed from a straight to a curved line by the magnetic field, as described by the Lorentz force law. Therefore there is a higher charge carrier density on one edge of the sample which induces a so-called Hall voltage (here in y-direction)

$$V_H = \frac{I_x B_z}{n d e}, \tag{3.2}$$

where I_x is the current applied along the x-direction, B_z is the magnetic field along the z-direction, d is the thickness of the sample and e is the electron charge. By measuring V_H the charge carrier density n can be computed. Then the mobility μ and the Hall constant R_H can be calculated as well using the relation $R_H = \mu\,\rho = \frac{1}{n\,e}$, where ρ is the resistivity of the sample. Note that this simple relation describes the case of one single conduction band.

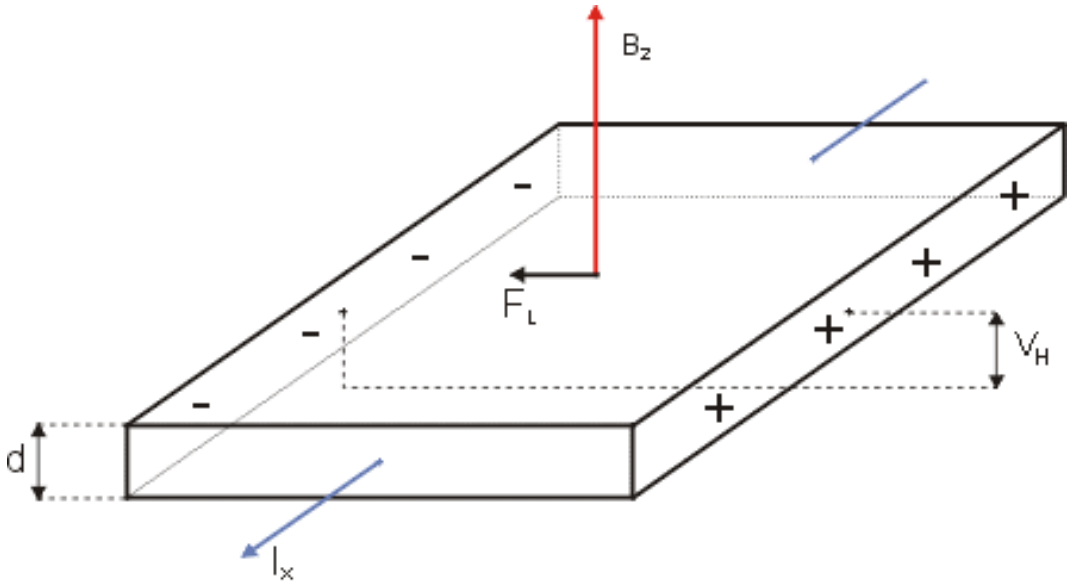

Figure 3.4: Sketch of the Hall effect with the current I_x, the magnetic field B_z and the Hall voltage V_H. F_L indicates the Lorentz force.

Sample preparation and equipment

Since the Hall effect can be anisotropic the sample has to be oriented using Laue measurements prior to Hall-effect measurements. The sample holder is similar to the ones used in the GUNDI. In this case six contacts must be applied to the sample.

These measurements were conducted in a temperature range of 2 to 300 K.

3.7 Magnetisation measurements

Magnetic properties were measured with the Quantum Design PPMS 6000 using the Vibrating Sample Magnetometer option. The measurements were conducted in a temperature range between 2 and 300 K.

The sample is mounted on a quartz sample holder. When inserted in the measuring chamber it is vibrated in a direction perpendicular to an applied magnetic field. The response of the sample creates a time-dependent magnetic field which induces a voltage in a pick-up coil. From the response of the sample in varying magnetic fields the susceptibility χ can be calculated: $\chi = \frac{M}{H}$ where M is the measured magnetisation of the sample in a magnetic field H.

3.8 Heat capacity measurements

The heat capacity C_P is defined as the amount of heat needed to increase the temperature of an investigated object by 1 K. In this work the values are expressed in terms of the molar heat capacity, that is, the heat capacity per mole of a material.

The measurement device used was a Quantum Design PPMS 6000. The temperature range for these measurements was 0.4 to 20 K. The lowest temperatures can be reached by ^{3}He technology. The sample is mounted on a sample holder using vacuum grease. In the PPMS a heater sends pulses of heat to the sample, increasing its temperature. After the pulse the sample temperature decreases again and is measured during this process. From the duration of the cooling the heat capacity can be determined.

Before the sample measurement, so-called addenda measurements had to be conducted, so that the heat capacity of the sample holder can be taken into account. The calibrations were not made for all different magnetic field strengths used in the sample measurements. Therefore testing measurements were conducted to determine the viability of the addenda for field strengths other than were used in the calibration. The results showed that the field strength at which addenda measurements were taken had little influence on the measured sample heat capacity (see figure 3.5).

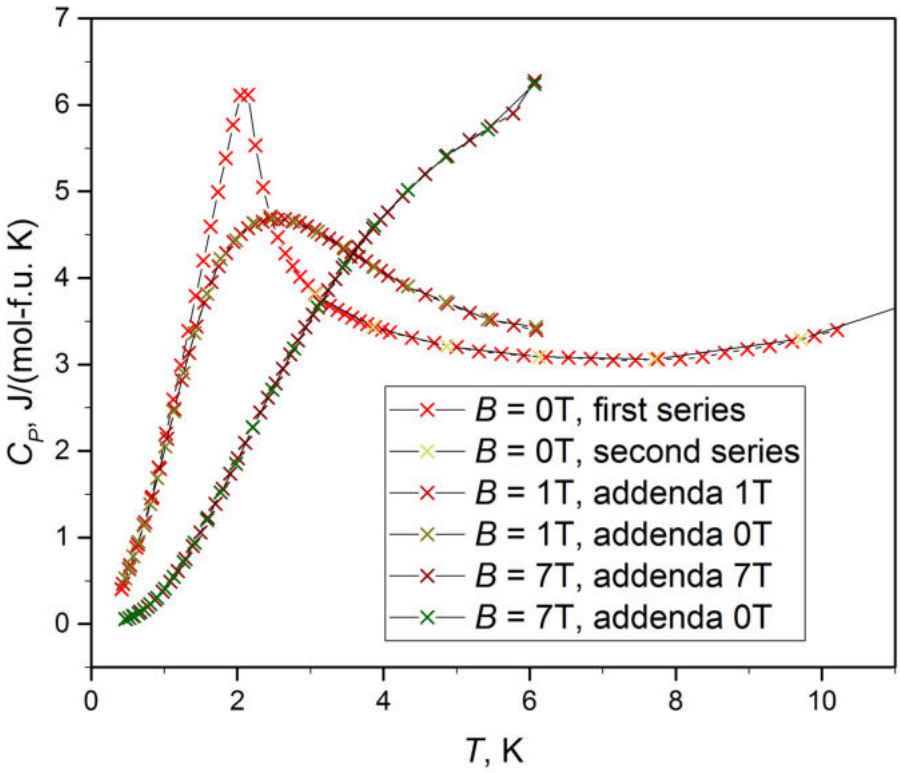

Figure 3.5: Heat capacity measurements performed on a CeBiPd sample with different addenda measurements and from different measurement series

4 Experiments with $CeRu_4Sn_6$

4.1 Introduction

$CeRu_4Sn_6$ is a Kondo semiconductor that crystallises in a tetragonal I-42m structure with the lattice parameters $a = 6.8810\,\text{Å}$ and $c = 9.7520\,\text{Å}$. One feature of this is that the length of the a-a plane diagonal $c' = \sqrt{a}$ differs from c by only 0.2%. This results in a so-called quasi-cubic structure [5].

Building on available knowledge about the synthesis of this compound, an optimisation of the processes will be attempted in order to produce single-crystalline samples of outstanding quality. One goal is to enhance the charge carrier mobility in the material. Another aspect that must be taken into account is the size of the crystals. To be able to collect data about the charge carrier mobility of a material by Hall-effect measurements a sample size of at least 0.7 mm is necessary.

So far, in studies dealing with Hall-effect measurements of $CeRu_4Sn_6$ [22] the floating zone technique has been used for the synthesis of single crystals. In this work, two methods will be implemented for the synthesis of high-quality, large-sized single crystals.

Firstly, the floating-zone technique will be used and the produced sample will be annealed. The idea behind this is that defects such as residual thermal stresses could exist in crystals grown by this technique, which could be annealed out. Secondly, the flux growth method will be used. So far only crystals of smaller sizes have been reported as results of this method [23], thus not providing a possibility to perform Hall-effect measurements.

Flux growth of single crystals is hard to control due to the interplay between a large amount of variables, of which many have not been systematically researched. Through a series of experiments adjusting these variables single crystals with the required size and quality could be grown in the course of this work.

During these flux growth experiments $Ce_3Ru_4Sn_{13}$ single crystals emerge as a by-product. $Ce_3Ru_4Sn_{13}$ crystallises in a cubic Pm-3n structure [24] with the lattice parameter $a = 9.7068\,\text{Å}$. It is closely related to the isostructural compound $CeRuSn_3$, the only difference being the occupation of one site by a Sn or a Ce atom, respectively. It has been postulated [25] that these two are only variants of one $Ce_{3+x}Ru_4Sn_{13-x}$ compound, with $0 \leqslant x \leqslant 1$.

$Ce_3Ru_4Sn_{13}$ has not been researched extensively, and no study of the physical properties of single-crystalline samples has been published. Furthermore it has been suggested [26] that $CeRuSn_3$ is a more stable compound than $Ce_3Ru_4Sn_{13}$. Therefore basic resistivity measurements were performed on these samples as well.

This chapter will be structured as follows: In the first two sections the $CeRu_4Sn_6$ crystal growth by the floating-zone method and annealing as well as the physical property measurements of this sample will be presented. In the following section a flux growth series of experiments including the results for $CeRu_4Sn_6$ and $Ce_3Ru_4Sn_{13}$ will be described.

4.2 Growth by floating zone method and annealing

In previous physical property measurements of $CeRu_4Sn_6$ single crystals the samples had been prepared by the floating-zone method. However, crystals grown by the floating-zone method may contain internal stresses and strains. In order to minimise the influence of these stresses and strains on the characterisation of the material an experimental design was set up as follows. On a sample grown using the floating-zone method two series of physical property measurements were performed, first in the as-grown state and then in its annealed state.

In the first step to produce the sample, two polycrystalline rods of $CeRu_4Sn_6$ were synthesised by melting together a stoichiometric mixture of Ce, Ru and Sn in the HF furnace. They were then used as seed and feed rods for the single crystal growth process. After their installation in the mirror furnace the process was conducted as described in 2.2.3. In the course of the process the relative position of the seed and feed rods had to be adjusted several times in order to stabilise the molten zone. After four days the feed rod was separated from the seed rod, concluding the growth process. The resulting sample will be called SJ02 in the following.

The resulting crystal was polished on the side shown in figure 4.1 to determine the microstructure. For this purpose, metallography and Laue measurements were conducted. Viewing the crystal through the polarising microscope showed one solid coloured, presumably single-crystalline area and some smaller areas with different colours (grains of different orientations). Laue pictures also show the uniform pattern with identical orientation of a single crystal in this larger area (see figure 4.2a). When examining the sample outside of that area several superimposed patterns can be seen (figure 4.2b).

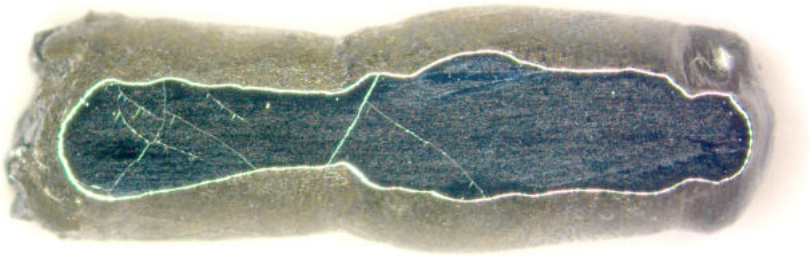

Figure 4.1: Polished surface of the $CeRu_4Sn_6$ sample SJ02 used for the determination of the microstructure

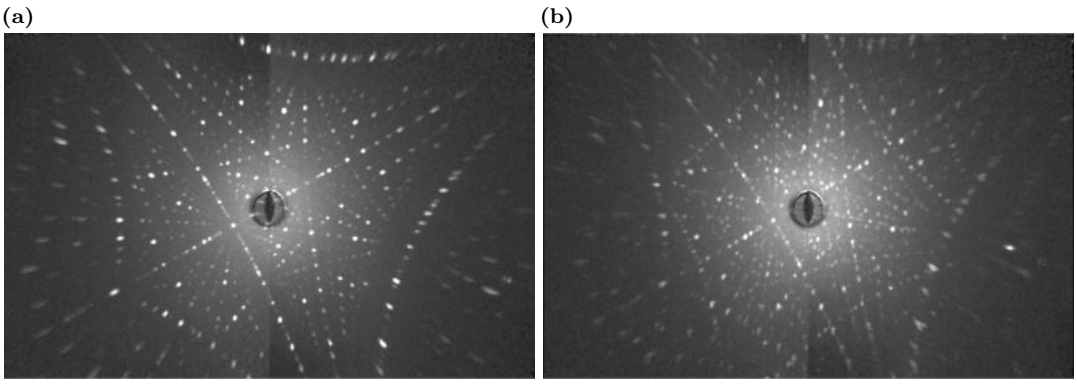

Figure 4.2: Laue pattern pictures of as-grown $CeRu_4Sn_6$ sample SJ02: (a) single-crystalline area, as can be seen from the clear pattern, (b) area with multiple overlapping patterns

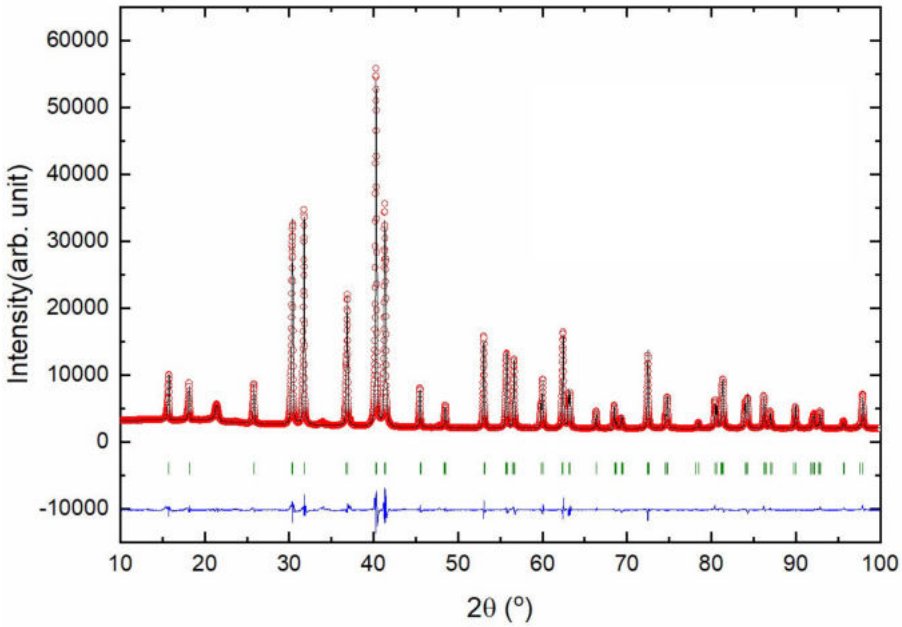

Figure 4.3: Refined XRD pattern of the $CeRu_4Sn_6$ SJ02 single crystal. The red dots show the measured intensities. The black line shows the pattern calculated in the refinement. The green vertical lines represent the Bragg positions for $CeRu_4Sn_6$. The blue line represents the difference between the measured intensities and the calculated pattern. The peak at 20.5° is an artefact of the measurement device. The weak peak at 34° can be caused by an impurity phase or inclusion.

The part of the crystal which was determined to be one single crystal was cut out with an Accutom-5. Since the charge carrier mobility is anisotropic in $CeRu_4Sn_6$ the orientation of the thus acquired single crystalline piece had to be determined. This was done by Laue measurements and with the help of the Laue pattern analysing programme OrientExpress 3.4. Due to the quasi-cubic structure of $CeRu_4Sn_6$ the c and c' directions could not be distinguished prior to the resistivity measurement. Instead, the crystal was cut in the three perpendicular directions that were determined to be either the c or the c' direction in the Laue measurements. Due to the brittleness of the material and cracks in the sample volume it broke into several pieces while cutting. A sufficiently large piece (see figure 4.4) was used for the measurements.

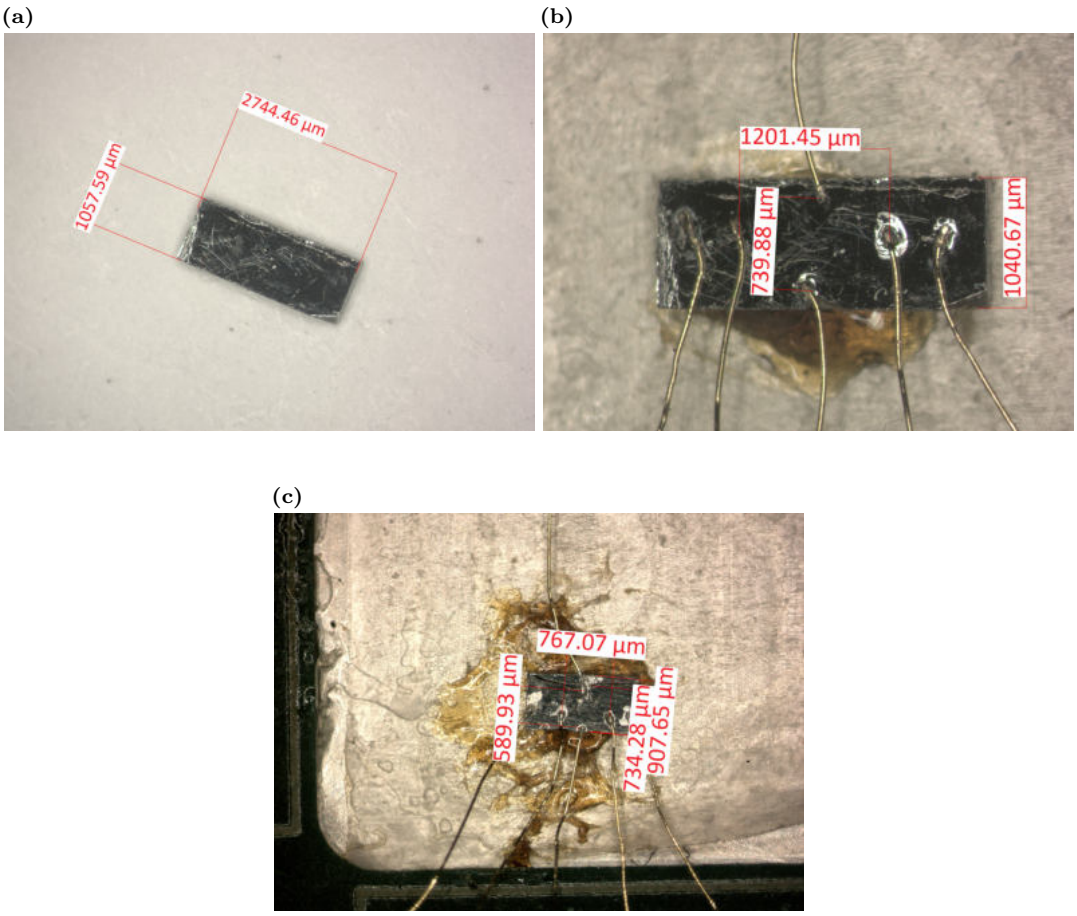

Figure 4.4: As-grown and annealed SJ02 prepared for Hall-effect measurements: (a) Polished as-grown sample. (b) As-grown sample contacted by spot welding. (c) Annealed sample contacted by using silver paint. Due to the brittleness of the material a piece broke off after the first measurements. To avoid further breaking silver paint was used instead of the spot welding method to apply the wires.

After conducting the measurements on the as-grown sample it was removed from the sample carrier and sealed in a quartz tube in vacuum. It was then put into a furnace at 750°C. After 14 days it was cooled down in the furnace with opened door and subsequently the surface was polished to remove any oxides. The physical properties were then again measured. The results of the measurements are presented in the following section.

4.3 Physical properties

On sample SJ02 both measurement series (before and after annealing) were conducted with the Quantum Design PPMS.

The field-dependent resistivity for the as-grown sample can be seen in figure 4.5 and for the annealed sample in figure 4.6. With decreasing temperature the resistivity increases until about 12 K. In zero field it decreases after a maximum and shows a slight upturn at the lowest temperatures. With increasing magnetic field this semiconductor-like behaviour is replaced by insulator-like behaviour as the energy gap is enlarged.

The resistivity of the annealed sample is lower than that of the as-grown sample. In addition,

the resistivity at low temperatures in the annealed state is not so pronouncedly influenced by the magnetic field as in the as-grown state (see figure 4.8).

The results of a study on a flux-grown $CeRu_4Sn_6$ single crystal [23] are shown in figure 4.7. The resistivity curve at $B = 0\,\mathrm{T}$ has a similar shape as well as very similar values to the as-grown crystal investigated here. In [23] a plateau following the upturn of the resistivity was measured below a temperature of 2 K. As these temperatures were not reached in the measurements on SJ02 this behaviour cannot be observed here.

In the temperature range of about 200 to 80 K the slope has a slight supralinear deviation from linearity. This hump is more distinct in the curve of the annealed sample than in that of the as-grown sample. It can also be found in previous measurements of $CeRu_4Sn_6$ resistivity in c-direction (see [27]).

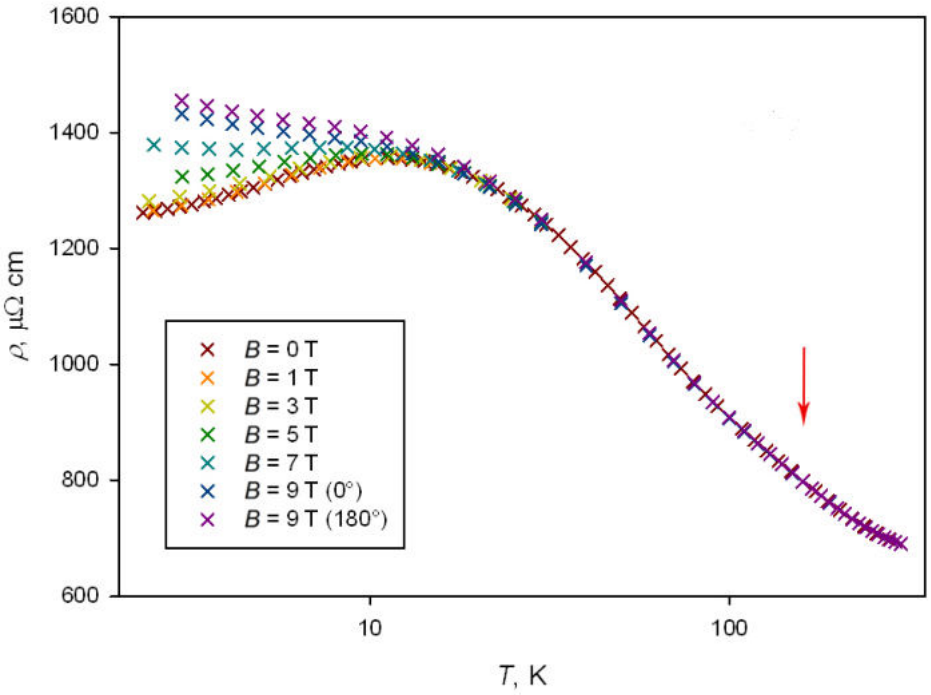

Figure 4.5: Measured resistivity of the as-grown $CeRu_4Sn_6$ sample SJ02 in different magnetic fields. As can be seen below, it is oriented in c-direction. The arrow indicates the position of the centre of the hump.

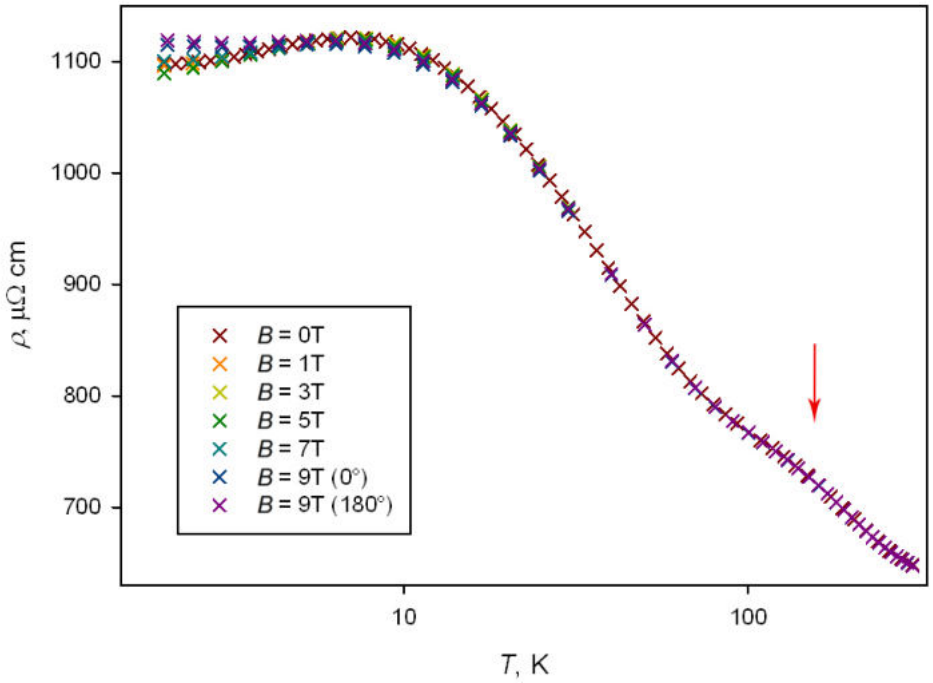

Figure 4.6: Measured resistivity of the annealed $CeRu_4Sn_6$ sample SJ02 in different magnetic fields. Again, the arrow indicates the position of the centre of the hump.

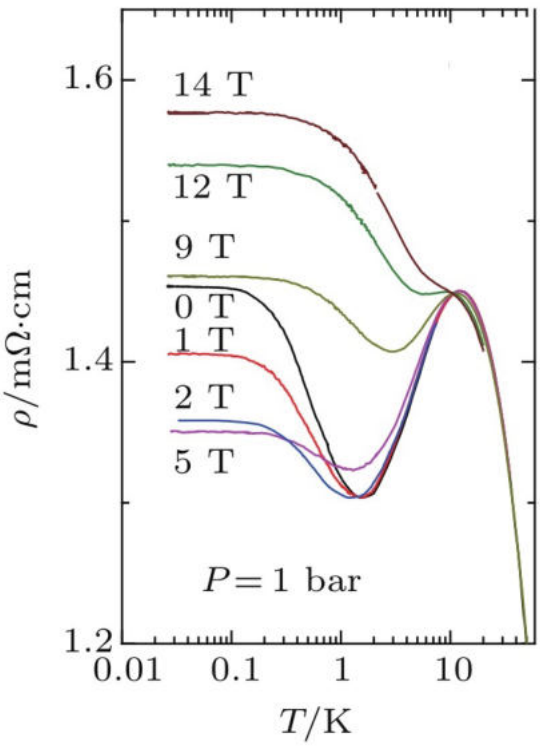

Figure 4.7: Temperature-dependent resistivity of $CeRu_4Sn_6$ at various magnetic fields taken from [23]

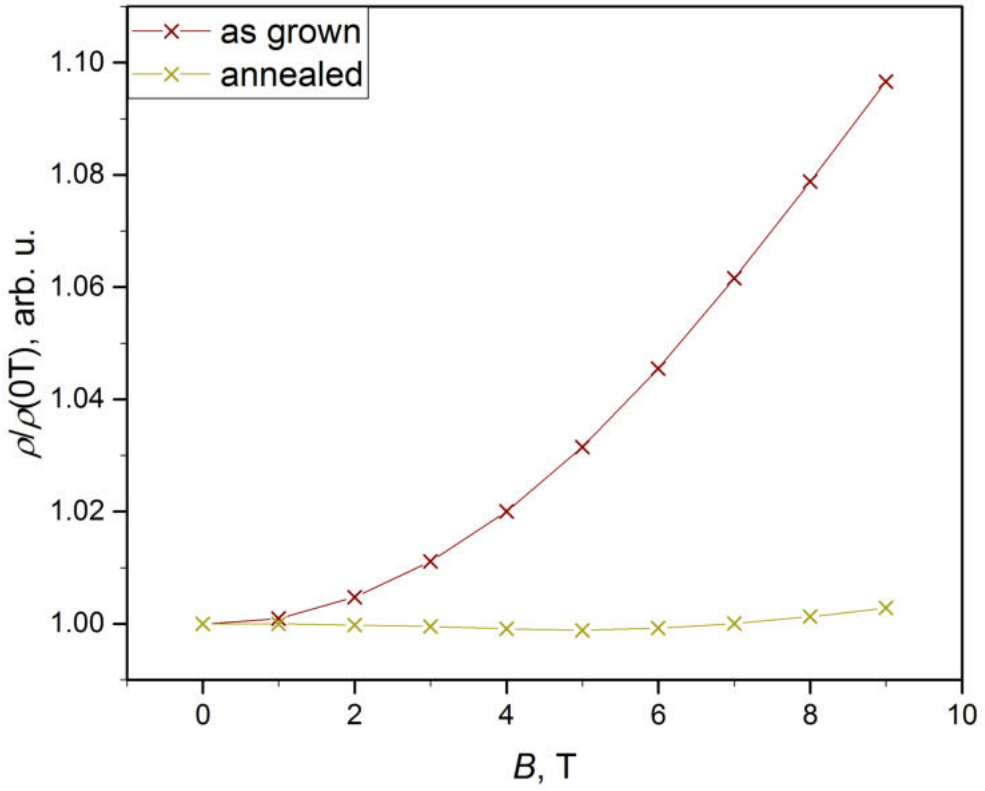

Figure 4.8: Magnetoresistance of the as-grown and annealed $CeRu_4Sn_6$ samples at $T = 4\,\mathrm{K}$

The relation between the resistivity ρ and the energy gap Δ of a semiconductor

$$\rho(T) = \rho_0\, e^{\frac{\Delta}{2k_B T}} \tag{4.1}$$

can be used to compute the magnitude of its energy gap. A fitting range of 170 K to 300 K was chosen.

For the as-grown sample the calculations resulted in a ρ_0 of 580(1) $\mu\Omega$cm and a $\frac{\Delta}{k_B}$ of 104(1) K. For the annealed sample the values $\rho_0 = 571(1)\,\mu\Omega$cm and $\frac{\Delta}{k_B} = 76(1)\,\mathrm{K}$ were calculated. It can be seen that annealing decreases the energy gap.

In previous studies comparable energy gap values are reported. In [23] a value of 130 K was calculated and in [27] a value of 85 K. In [28] a temperature-dependent gap was calculated for ranges of 20 K. In the range of 170 – 300 K these values vary between 61 and 91 K.

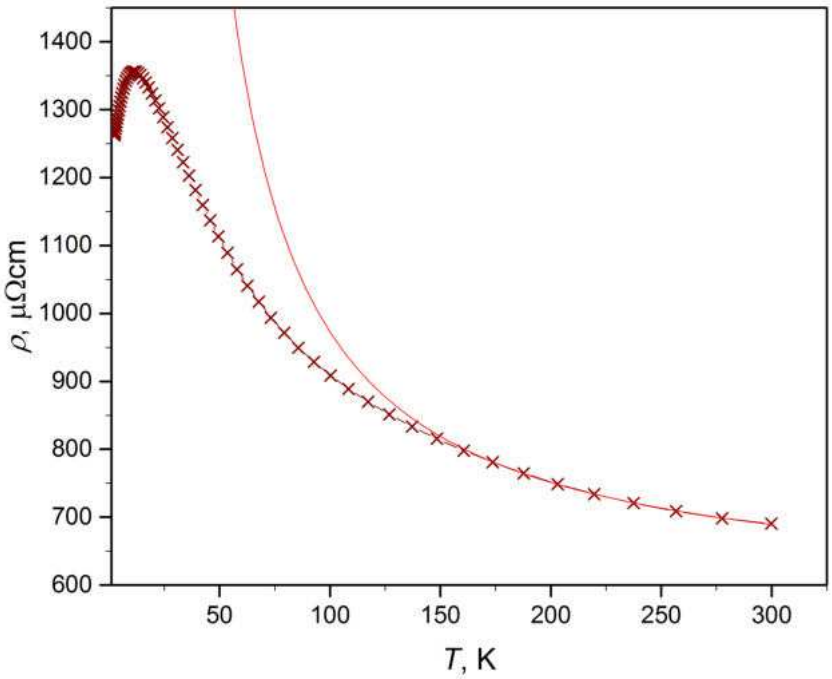

Figure 4.9: Measured resistivity of the as-grown $CeRu_4Sn_6$ sample with exponential fit for the gap calculation

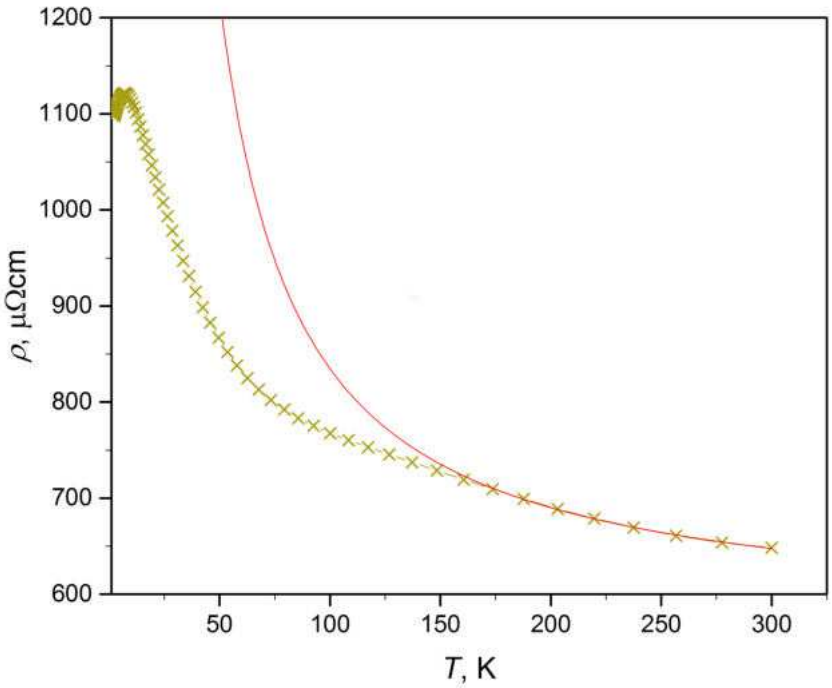

Figure 4.10: Measured resistivity of the annealed $CeRu_4Sn_6$ sample with exponential fit for the gap calculation

The resistivity curve in zero-field for SJ02 is in agreement with the resistivity of other samples of single- and polycrystalline $CeRu_4Sn_6$ measured previously (figure 4.11). The maximum at

about 12 K can be seen in all of the data sets, although at slightly different temperatures.

Since the crystal structure of $CeRu_4Sn_6$ is such that the c- and c'-directions in the crystal cannot be distinguished by Laue measurement only, the physical properties have to be used to determine the direction. By comparing with results of previous resistivity measurements on crystals with known orientations, the sample at hand can be determined to be oriented in c-direction, as shown in figure 4.11.

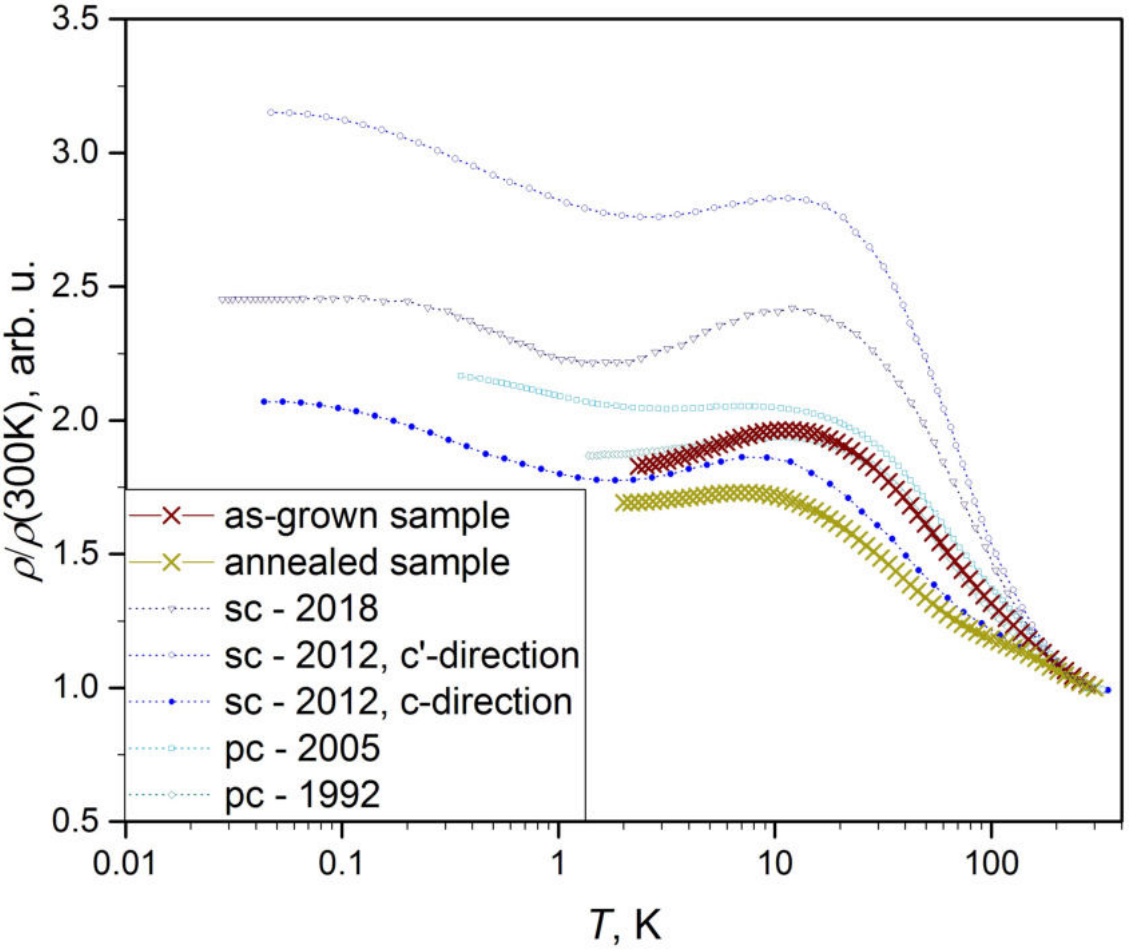

Figure 4.11: Zero-field resistivity measurements of $CeRu_4Sn_6$. Values are normalised to the respective value at 300 K. 2018 data are taken from [23], 2012 data from [27], 2005 data from [3], and 1992 data from [29]. Single-crystalline samples are indicated by "sc" and polycrystalline samples by "pc". The 2005 curve only shows the $4f$ contribution to the resistivity.

When using a simple single-band model, the charge carrier concentration and mobility can be determined. The resulting mobility curves of the as-grown and the annealed samples can be seen in figure 4.12 and the charge carrier concentration curves in figure 4.13. The mobility increases slightly with annealing which could be due to the release of residual thermal defects (stresses). However, the effect is rather small and thus we have to conclude that annealing does not improve the sample quality to a substantial extent.

The temperature-dependent Hall constant can be seen in figure 4.14. Below around 30 K the curve of the annealed sample increases less strongly than that of the as-grown sample. The reference curve for a polycrystalline sample from [3] increases even more strongly with decreasing temperature. Thus, it seems like a weaker increase is a sign of higher sample quality,

assuming that the polycrystal is of lowest quality.

The Hall resistivity dependent on the magnetic field in the sample after annealing (see figure 4.15b) shows slightly non-linear behaviour at low temperatures. This behaviour indicates that a single-band model does not fully describe the material.

Further investigation is needed to find a fitting model for the non-linear behaviour, and to find out why it arose after the sample was annealed.

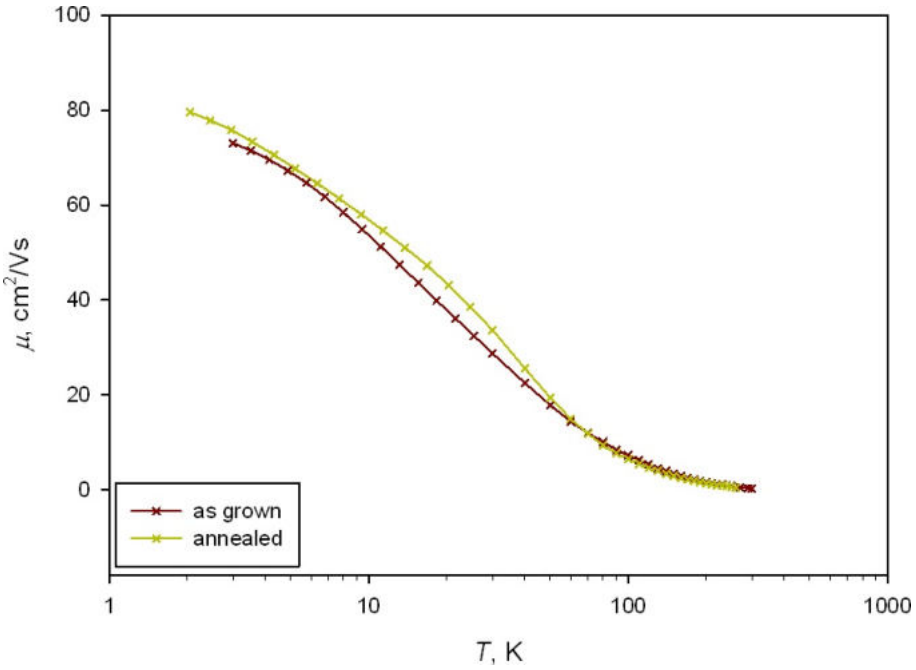

Figure 4.12: Charge carrier mobilities for $CeRu_4Sn_6$ sample SJ02

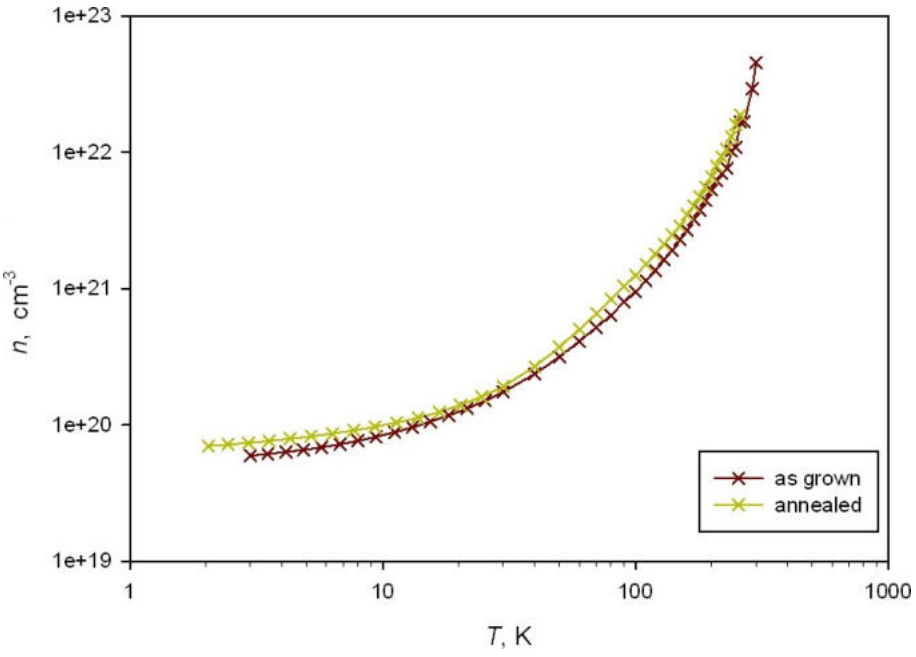

Figure 4.13: Charge carrier concentrations for $CeRu_4Sn_6$ sample SJ02

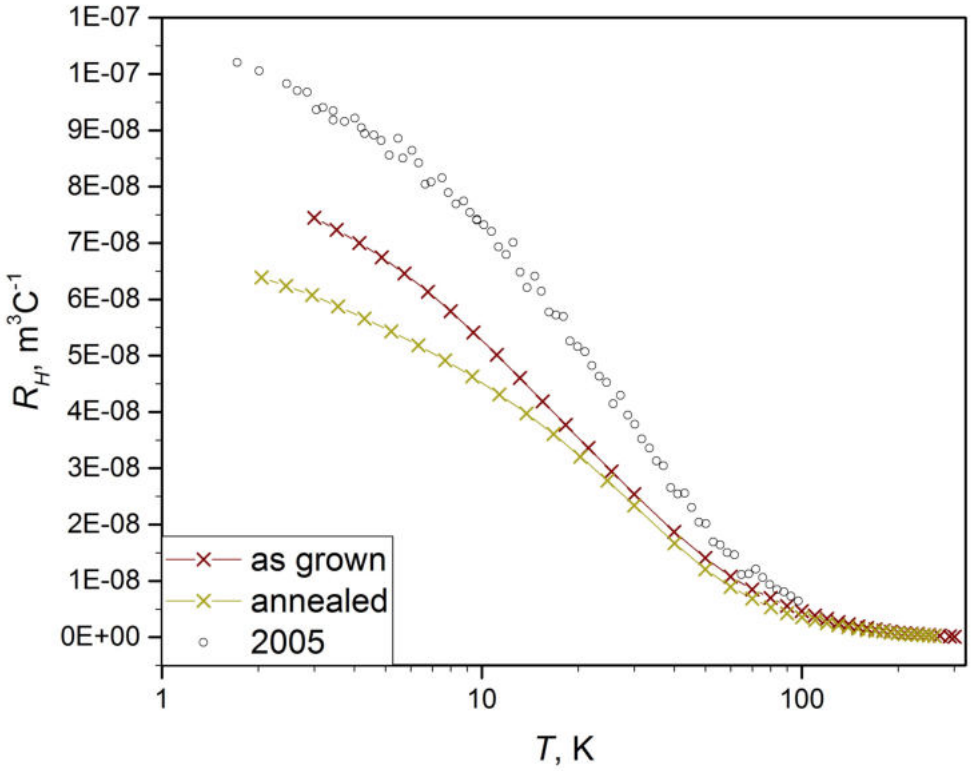

Figure 4.14: Hall constants for $CeRu_4Sn_6$ sample SJ02; 2005 data of polycrystalline $CeRu_4Sn_6$ were extracted from [3].

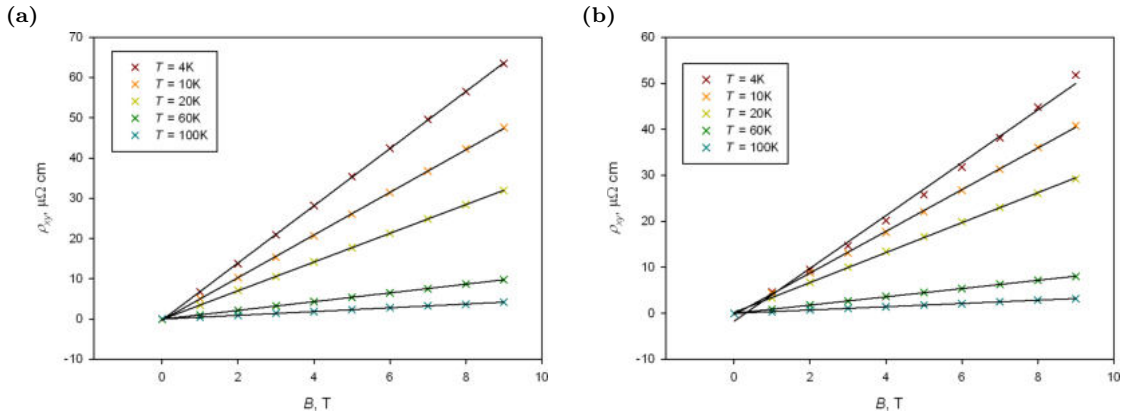

Figure 4.15: Field-dependent Hall resistivity at different temperatures for (a) as-grown and (b) annealed $CeRu_4Sn_6$ sample SJ02. The lines represent linear fits.

4.4 Flux growth of large single crystals

Several experiments were carried out before reaching the goal of growing 0.7 mm big single crystals. In the course of these experiments many parameters including flux to sample ratio, initial composition, and temperature profile were adjusted.

After each growth experiment the produced crystals were examined using a light microscope and subsequently powder XRD and/or EDX techniques. The results of these investigations

were used to determine the parameters for the next growth process.

4.4.1 Strategies

In order to achieve flux growth of large $CeRu_4Sn_6$ single crystals most experiments were aimed at determining a suitable starting composition as well as flux composition and flux to sample ratio. Then a method for increasing the size of the resulting crystals had to be investigated. Depending on the selected cooling rates (and also availability) either the box furnace or the vertical furnace were used, as indicated below.

The starting point for this series of experiments was the description of the method used in [23]. Based on this report the starting composition of the first experiment of this series was conducted using a molar ratio of Ce:Ru:Sn = 1:4:6 and 80 vol.% of pure Pb as a flux. The temperature profile in the furnace was as follows: heating up to 1150°C with a rate of 150°C/h, staying at that temperature for 24 h (holding time) and then cooling down to 600°C with a rate of 2°C/h. The resulting batch of crystals did contain $CeRu_4Sn_6$, but only small crystals with typical sizes around 0.3 mm. $Ce_3Ru_4Sn_{13}$ and $CePb_3$ were contained in large quantities.

Crystal growth in different fluxes

Apart from lead, Bi and In are two other commonly used metallic fluxes [30]. In order to test the viability of these two elements as fluxes for growing $CeRu_4Sn_6$ the following experiments were carried out.

SJ05 was synthesised using a piece of $CeRu_4Sn_6$ mixed with 80 vol.% Bi as the flux. Most of the grown crystals had a needle- or platelet-like shape. An examination by powder XRD shows Ru_2Sn_3 to be the main phase. Some smaller amounts of pure Bi and Ru are also contained. No $CeRu_4Sn_6$ was detected.

Additionally, growth from partial self-flux was tried. In SJ04 $CeRu_4Sn_6$ was mixed with 70 vol.% flux. The flux was composed of 10 vol.% Ce and 90 vol.% In. An examination by powder XRD showed a good match with In_3Ru, $Ce_3Ru_4Sn_{13}$ and In_3Ce compounds. In the EDX measurement the In in the In_3Ru and In_3Ce was found to be partly substituted by Sn to a varying degree. Again no $CeRu_4Sn_6$ was detected.

Several different mixtures between Pb and Sn with varying ratios were tested as flux materials. These Pb:Sn ratios were 76:4 (SJ15), 45:5 (SJ14), 35:15 (SJ13) and 10:50 (SJ12). Out of these, only SJ14 contained a substantial amount of $CeRu_4Sn_6$.

One experiment (SJ03) was conducted using pure self-flux of Sn and Ce. A piece of $CeRu_4Sn_6$ was mixed with 70 vol.% flux. The flux consisted of 10 vol.% Ce and 90 vol.% Sn. The resulting crystals did not contain $CeRu_4Sn_6$, but only Ru_3Sn_7 and $Ce_3Ru_4Sn_{13}$. The resistivities of two of these $Ce_3Ru_4Sn_{13}$ crystals were measured, see 4.4.2.

Growth from the melt was attempted in SJ06 in order to avoid the formation of impurity phases containing Pb. The overall Ce:Ru:Sn ratio of the mixture was 7:30:63 to avoid the pure Ru phase. The sample did not melt in the furnace.

SJ07 and 09 were produced using less Pb flux. The $CeRu_4Sn_6$:Pb molar ratios 1:80 and 1:50 respectively were tested. Both samples had $CeRu_4Sn_6$ as the main phase.

When SJ07 was centrifuged to remove the flux, all of the material accumulated in one piece with the flux. After heating to 800°C and centrifuging a second time some small crystals could be detected. An XRD measurement shows that the main phase of this sample is Ru. $CeRu_4Sn_6$ and Ce_3Pb are also contained.

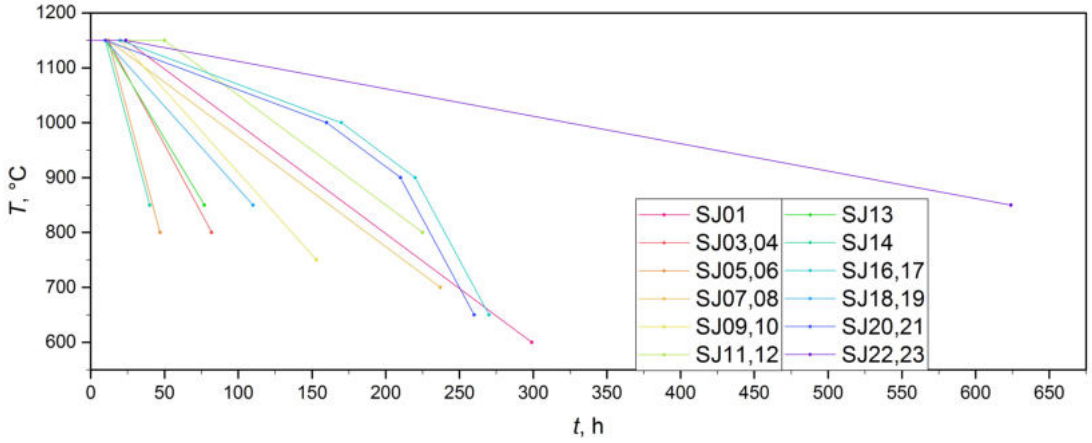

Figure 4.16: Temperature programmes of the $CeRu_4Sn_6$ SJ sample series

Table 4.1: Temperature programmes of most of the $CeRu_4Sn_6$ SJ samples. Rates r are given in °C/h, temperatures T in °C and holding times t in h.

Sample name(s)	Temperature programme				Furnace type
	r_{heat}	T_{hold} (t_{hold})	r_{cool}	T_{final}	
SJ01	150	1150 (24)	2	600	Box
SJ03, 04	150	1150 (12)	5	800	Box
SJ05, 06	150	1150 (12)	10	800	Box
SJ07, 08	150	1150 (12)	2	700	Box
SJ09, 10	150	1150 (20)	3	750	Box
SJ11, 12	150	1150 (50)	2	800	Box
SJ13	200	1150 (10)	4.5	850	Vertical
SJ14	200	1150 (10)	10	850	Vertical
SJ18, 19	200	1150 (10)	3	850	Box

Crystal growth with varying initial composition

Several experiments with initial compositions deviating from a Ce:Ru:Sn ratio of 1:4:6 were conducted. Previous research on the Ce-Ru-Sn system was taken into account for these experiments, see [25]. All relevant compositions and element ratios can be seen in figure 4.17.

As mentioned above, SJ06 was synthesised using a Ce:Ru:Sn ratio of 7:30:63. This composition was chosen in order to avoid the growth of Ru_2Sn_3. The sample did not melt in the furnace due to the small amount of Sn flux.

Samples SJ08 and 10 were produced using an initial ratio of 9:43:48. Again, the aim was to

avoid Ru_2Sn_3. SJ08 was made using polycrystalline $CeRu_4Sn_6$ mixed with additional Ce and Ru. The sample did not melt in the furnace. SJ10 was synthesised from the pure elements. The main phase of the resulting batch was $Ce_3Ru_4Sn_{13}$.

In order to avoid $Ce_3Ru_4Sn_{13}$, a ratio of 8.5:40:51.5 was used for SJ16 and 17. According to the phase diagram found in [25] (see also figure 4.17), this point is on a tie line between $CeRu_4Sn_6$ and Ru. $CeRu_4Sn_6$ was the main phase of this batch. Therefore this ratio was used in an experiment for increasing the size (SJ23, see below).

The temperature programmes of these samples are shown in table 4.1 and in figure 4.16.

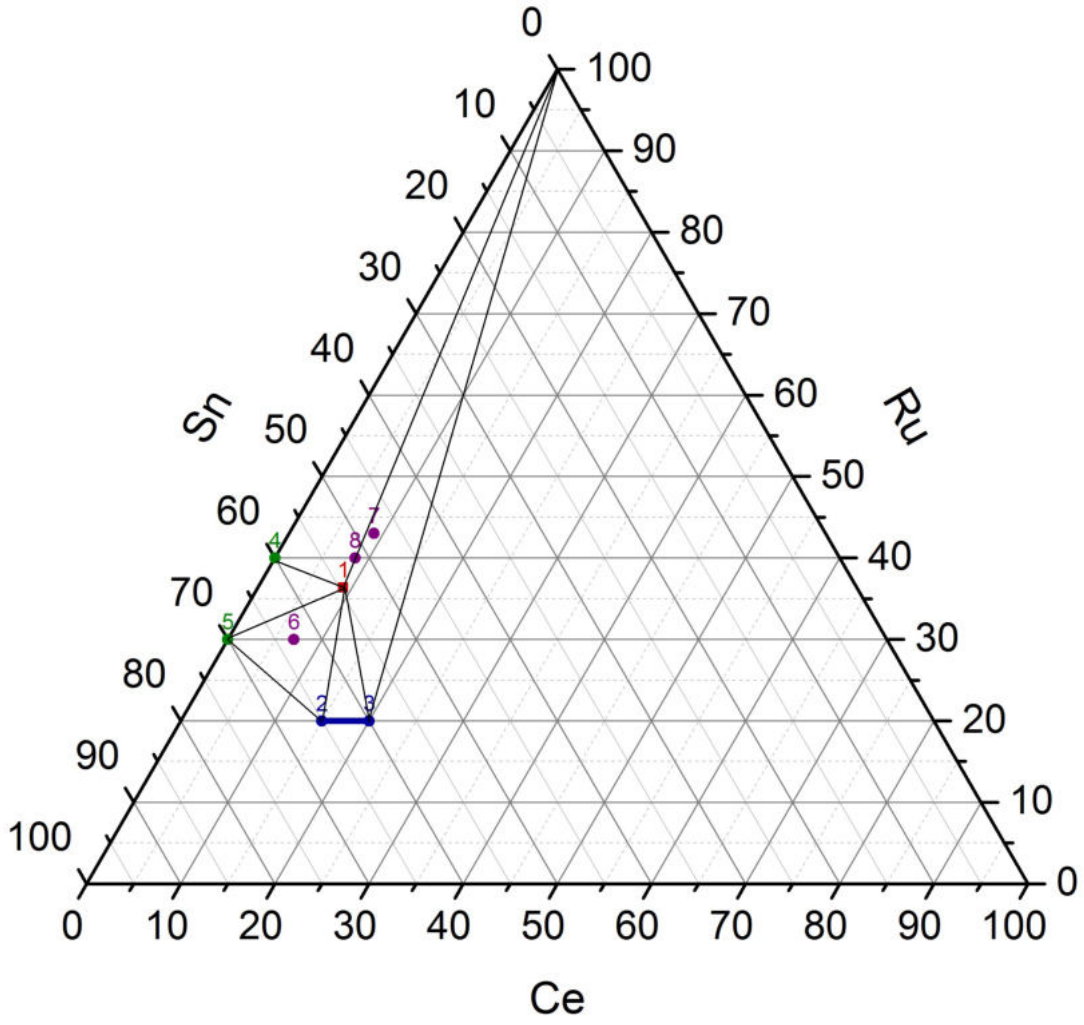

Figure 4.17: Sketch of a ternary diagram of the Ce-Ru-Sn compositions relevant to this work, arbitrary temperature. (1) $CeRu_4Sn_6$, (2) $Ce_3Ru_4Sn_{13}$, (3) $CeRuSn_3$, (4) Ru_2Sn_3, (5) Ru_3Sn_7; Ce:Ru:Sn atomic ratios: (6) 7:30:63, (7) 9:43:48, (8) 8.5:40:51.5.

Crystal growth with different temperature profiles

Several different cooling rates were used in the course of these experiments. For a quick analysis of the phase constitution of an initial composition a high cooling rate of 5 or 10°C/h was chosen. When also considering the size of the crystals rates between 0.5 and 3°C/h were chosen. Additionally to these considerations experiments with step-wise cooling were conducted.

The first such experiment (SJ15) consisted of several steps over a long period of time. After heating up to 1150°C the temperature was held for 50 hours. Then each of the cooling steps consisted of cooling down by 30°C with a rate of 2°C/h and then heating up by 10°C with a rate of 10°C/h. The last temperature that was reached by heating was 970°C and from there the sample was cooled to 750°C with 2°C/h. The process is depicted in figure 4.18. By oscillating the temperature in the cooling process, we expected smaller crystals to be melted but large ones to be retained. The resulting batch did not contain large crystals, maybe due to the wrong temperature range for oscillation. Furthermore, $CeRu_4Sn_6$ was not the main phase, as can be seen from figure 4.19.

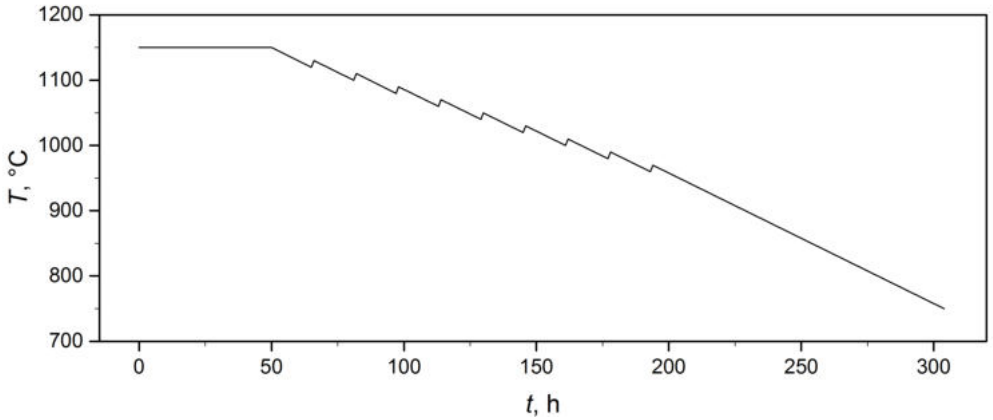

Figure 4.18: Temperature programme used for the $CeRu_4Sn_6$ sample SJ15

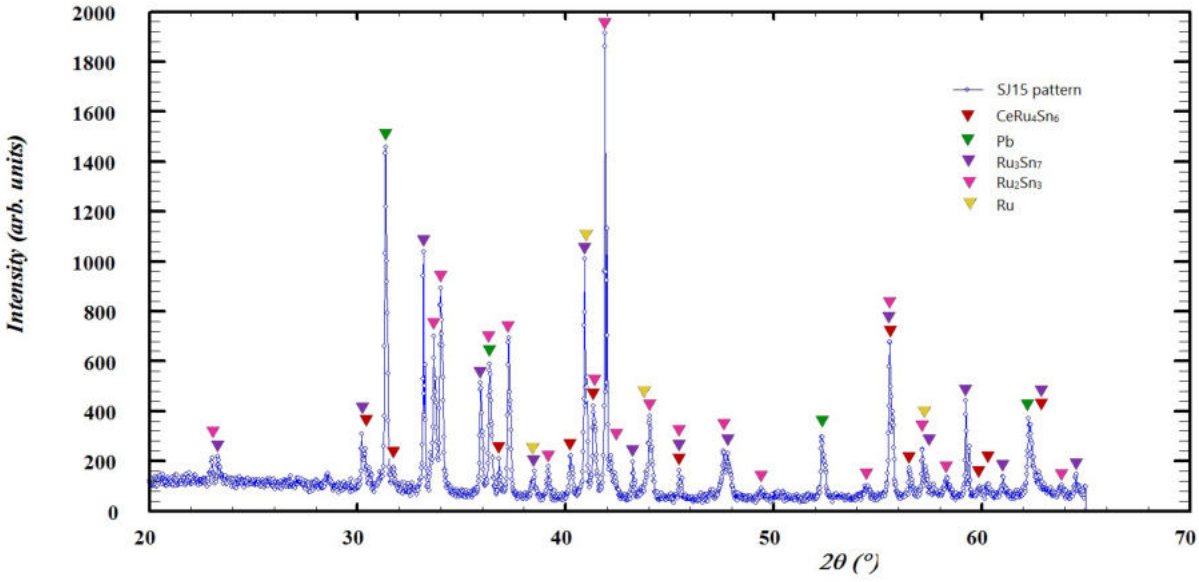

Figure 4.19: XRD pattern of the $CeRu_4Sn_6$ sample SJ15 with included phases marked

Another approach to phased cooling was used in the synthesis of samples SJ16, 17, 20 and 21. This was done in order to decrease the duration of the synthesis process. All of the samples were heated up to the highest temperature (1150°C) with a heating rate of 150°C/h. For SJ16

and 17, this temperature was held for 20 h. For SJ20 and 21 it was 10 h. The cooling steps were the same for all four samples. From the highest temperature a low cooling rate was used (1°C/h) until reaching 1000°C. The second step was cooling down to 900°C at a rate of 2°C/h. Finally with a high rate of 5°C/h the samples were cooled down to 650°C. The temperature programmes are plotted in figure 4.16. The experiments resulted in regularly-shaped $CeRu_4Sn_6$ crystals which nearly reached the required size (see figure 4.20).

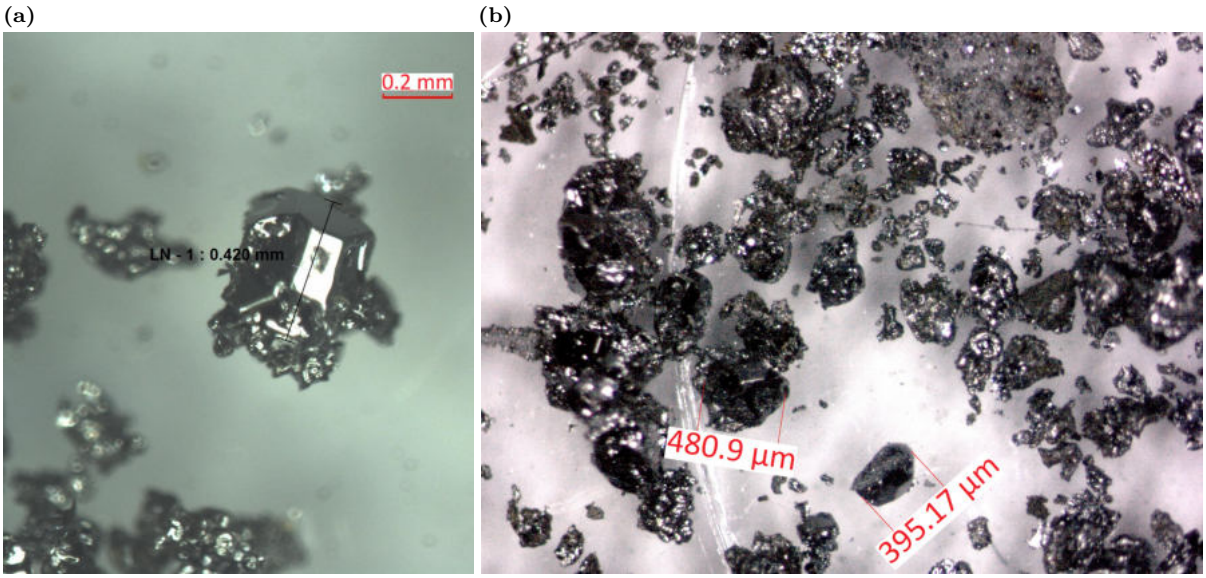

Figure 4.20: $CeRu_4Sn_6$ crystals produced with a step-wise cooling approach from (a) SJ17 and (b) SJ21.

Source materials

For SJ03, 04, 05, 06, 07 and 08 pieces of a $CeRu_4Sn_6$ polycrystalline sample were used. It had been synthesised at the IFP-TU Wien in the HF furnace in previous investigations. A piece with an appropriate size was cut off and mixed with the corresponding amount of flux.

The materials used to synthesise SJ08 did not melt in the furnace. With EDX measurements small crystals, some of them $CeRu_4Sn_6$, were found on the surface of the polycrystalline $CeRu_4Sn_6$ piece. In the synthesis of SJ07 similar difficulties were experienced.

In SJ09 and 10 the experiments SJ07 and 08, respectively, were repeated. This time pure elements were used and the holding time was increased from 12 to 20 h. With this approach the constituents melted as expected.

In SJ11 a similar experiment as with SJ07 and 08 was conducted, but the piece of $CeRu_4Sn_6$ was crushed into small pieces before mixing with the flux. Thus it could be possible that $CeRu_4Sn_6$ melts completely and mixes with the flux homogeneously. The holding time was also adjusted to 50 h.

The XRD patterns of SJ09 and SJ11 are shown in figure 4.21 and figure 4.22, respectively. The low intensity in the XRD patterns makes it difficult to perform quantitative Rietveld refinements, but it can be enough to identify the phase constituents in each sample. According to this the use of crushed pieces of $CeRu_4Sn_6$ as source material produces more $CeRu_4Sn_6$ crystals in the resulting batch than the use of pure elements.

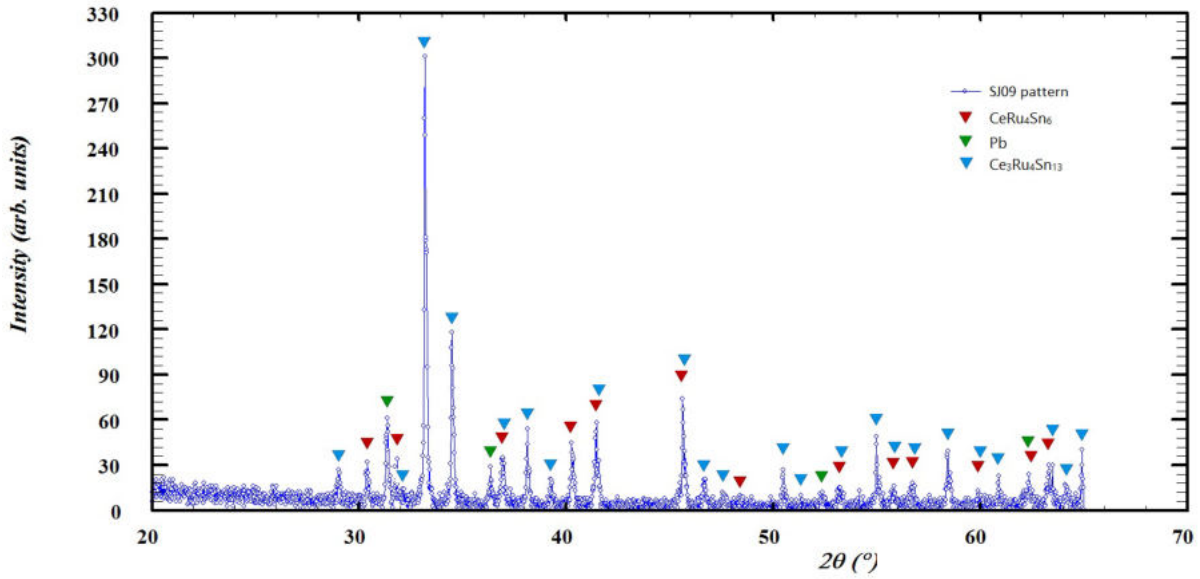

Figure 4.21: XRD pattern of the sample batch SJ09. Peaks from the phases $CeRu_4Sn_6$, Pb and $Ce_3Ru_4Sn_{13}$ are marked by the indicated colours. The crystals were grown from pure elements.

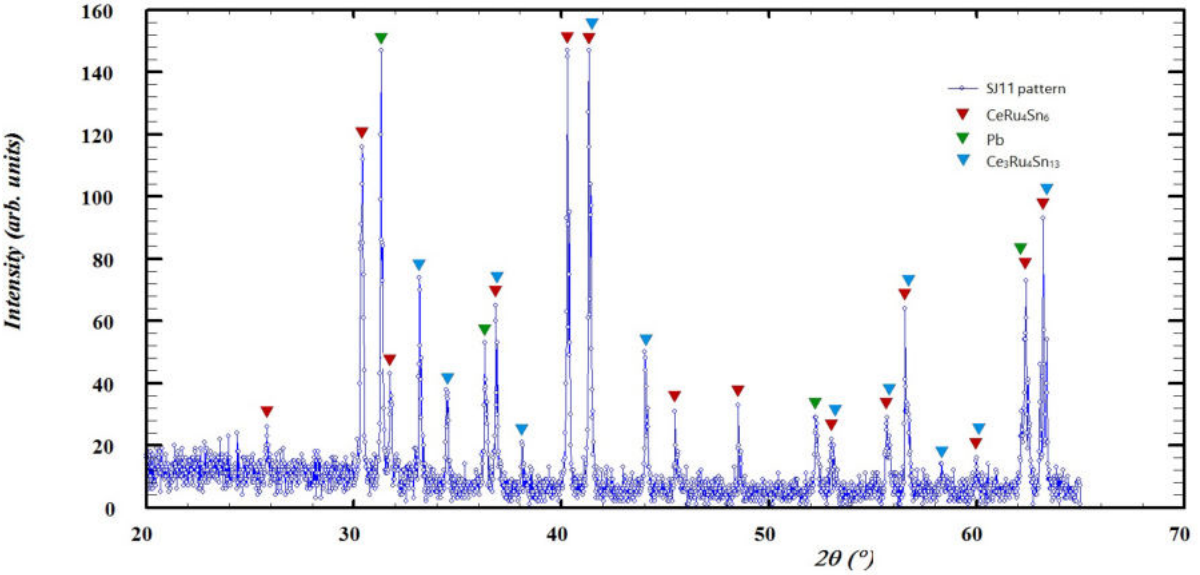

Figure 4.22: XRD pattern of the sample batch SJ11. Peaks from the phases $CeRu_4Sn_6$, Pb and $Ce_3Ru_4Sn_{13}$ are marked by the indicated colours. The crystals were grown from pre-alloyed $CeRu_4Sn_6$ polycrystalline samples.

SJ16 and 17 were produced to directly compare the results of using different source materials. The only difference in the procedures used was that for SJ16 pure elements were used, but for SJ17 a crushed pre-melted $CeRu_4Sn_6$ alloy was used. This rough comparison showed no significant differences in the two experiments' outcomes – neither in phases nor in shapes or sizes of the crystals.

4.4.2 Results

Growth of large $CeRu_4Sn_6$ single crystals

The following two initial compositions were selected, based on the previous experiments, to conduct an experiment with an especially low cooling rate. Firstly, a sample with a $CeRu_4Sn_6$:Pb molar ratio of 1:50 (SJ22) and secondly, a sample using a mixture of $CeRu_4Sn_6$ with added Ru powder and Sn so that Ce:Ru:Sn became 8.5:40:51.5; with a mixture:Pb molar ratio of 1:50 (SJ23) were prepared. The source materials for both samples were crushed pieces of $CeRu_4Sn_6$ alloy. These two samples were put in the vertical furnace with a temperature programme of staying at 1150°C for 24 h and then cooling down with 0.5°C/h to 850°C. Because the flux was not completely removed by centrifuging after the growth process (see 2.2.2), the resulting crystals were coated with a film of Pb. This was removed by chemical etching. Selected large crystals were kept in a mixture of nitric acid (65%) and water with a volume ratio of 1:3 for two days.

(a)

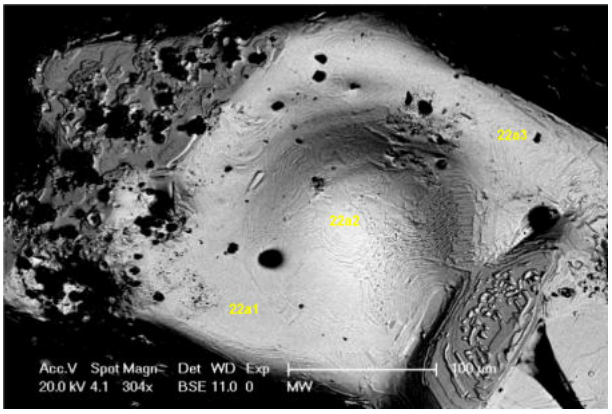

(b)

Measured point	Ce	Ru	Sn
a1	9.7	35.2	55.1
a2	10.0	34.8	55.2
a3	9.9	34.9	55.2

(c)

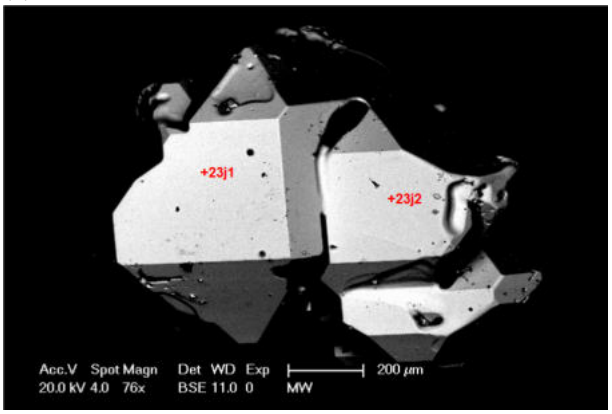

(d)

Measured point	Ce	Ru	Sn
j1	9.7	34.8	55.5
j2	9.4	35.2	55.4

Figure 4.23: (a) SEM image of a $CeRu_4Sn_6$ crystal from SJ22. (b) Compositions measured by EDX (at.%) from the marked points in (a). (c) SEM image of a $CeRu_4Sn_6$ crystal from SJ23. A photograph of the contacted sample is shown in figure 4.26c. (d) Measured compositions (at.%) at the marked points in (c).

The main phase as detected by XRD measurements is $CeRu_4Sn_6$ in both cases (see figure

4.24 and figure 4.25). The additional phases Ru_3Sn_7 and Ru_2Sn_3 are in accordance with the phase diagram (figure 4.17).

These two batches contain single-crystalline $CeRu_4Sn_6$ with larger crystal sizes than previously achieved (see figures 4.23 and 4.26). SJ22 yielded crystals with uneven surfaces (see figure 4.23a). In the following only crystals from SJ23 were used.

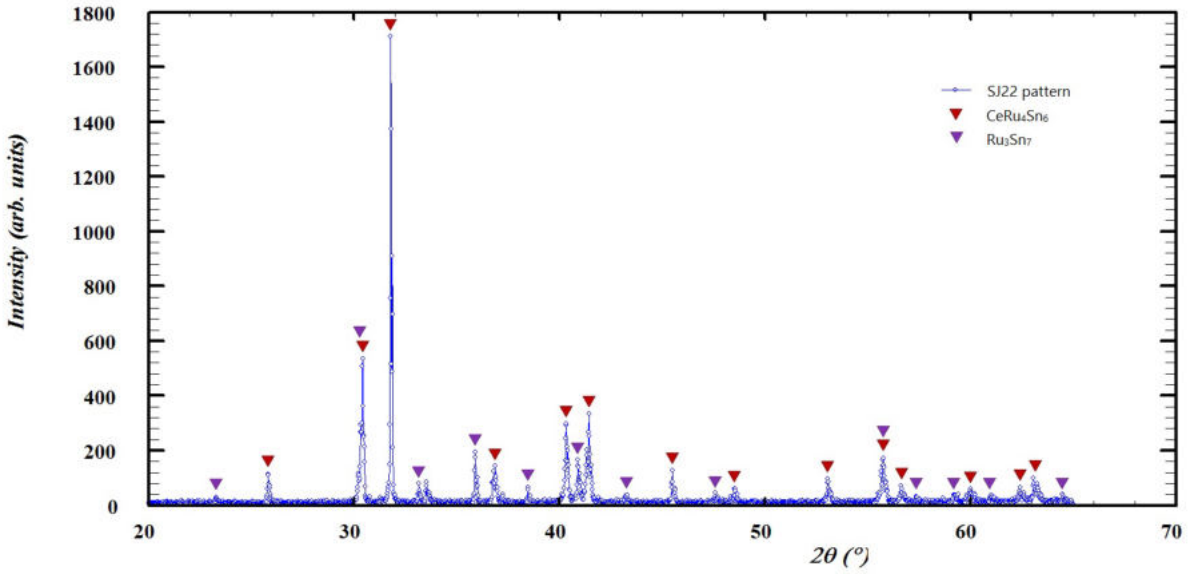

Figure 4.24: XRD pattern of the sample batch SJ22. Peaks from the phases $CeRu_4Sn_6$ and Ru_3Sn_7 are marked by the indicated colours.

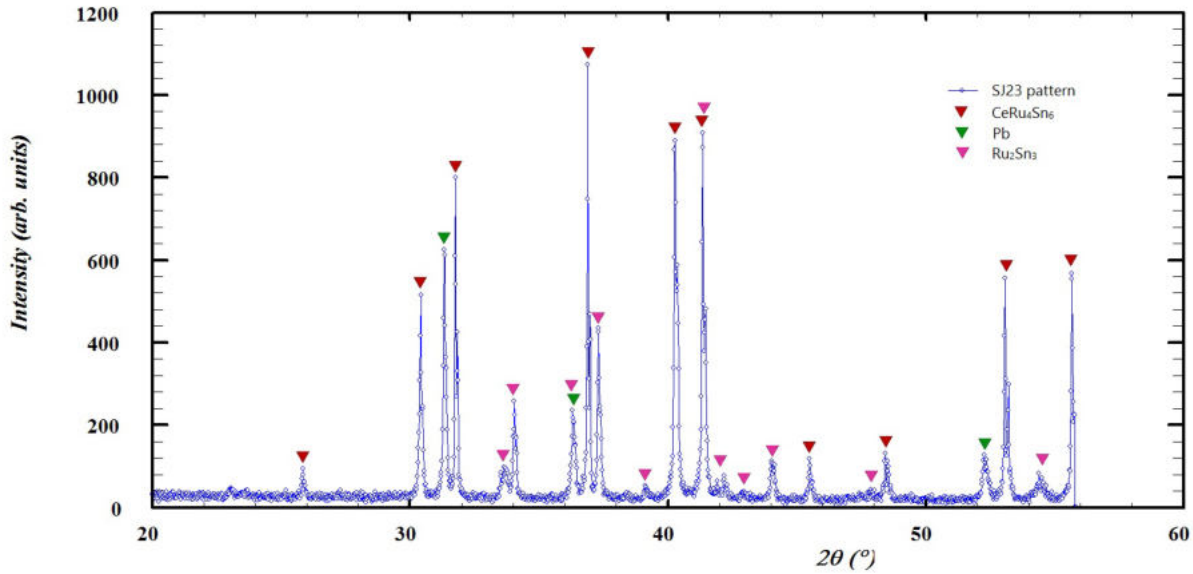

Figure 4.25: XRD pattern of the sample batch SJ23. Peaks from the phases $CeRu_4Sn_6$, Pb and Ru_2Sn_3 are marked by the indicated colours.

A non-stoichiometric initial composition was chosen for SJ23 to reach a stoichiometry of $CeRu_4Sn_6$. From the measured compositions of the crystals no significant influence of the

initial composition on the crystal composition was observable (see table 4.2).

In collaboration with Diego Zocco and Diana Kirschbaum from IFP-TU Wien, we characterised one of the SJ23 samples by means of electrical resistivity, magnetoresistance and Hall effect measurements down to 0.5 K. The sample shown in figure 4.26c (Laue image in figure 4.27) was contacted with 25 μm annealed gold wires using a spot-welding device. Initial results revealed that the mobility is similar or smaller to those obtained in previously grown single crystals ($\mu \approx 100\,\mathrm{cm}^2/\mathrm{Vs}$ at 0.5 K, [22]), although further measurements must be performed to confirm this result.

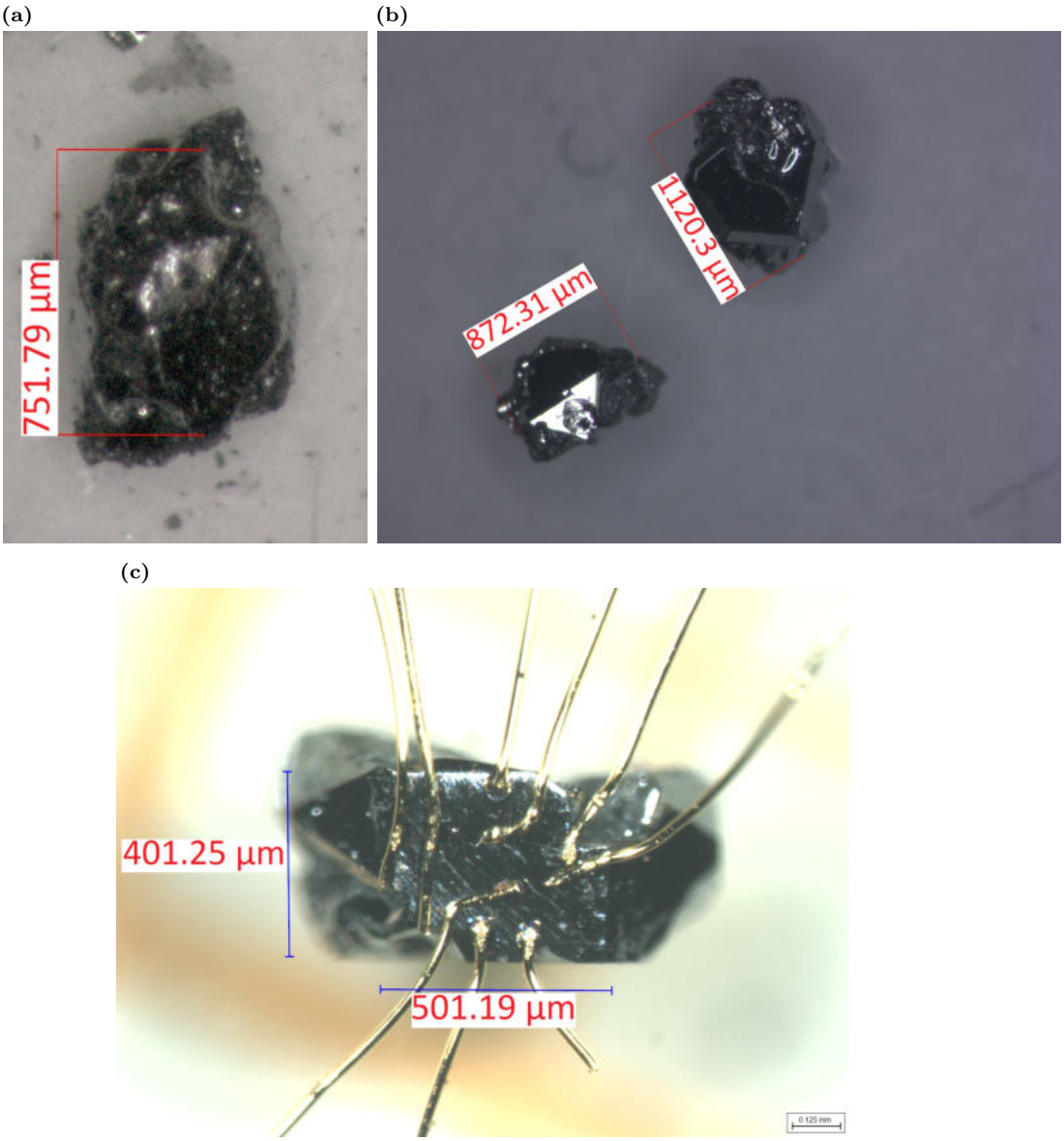

Figure 4.26: Large flux grown $CeRu_4Sn_6$ single crystals: (a) from SJ22, (b) from SJ23, and (c) a crystal from SJ23 with attached gold wires for resistivity, magnetoresistance and Hall effect measurements; photograph provided by D. Zocco (IFP-TU Wien).

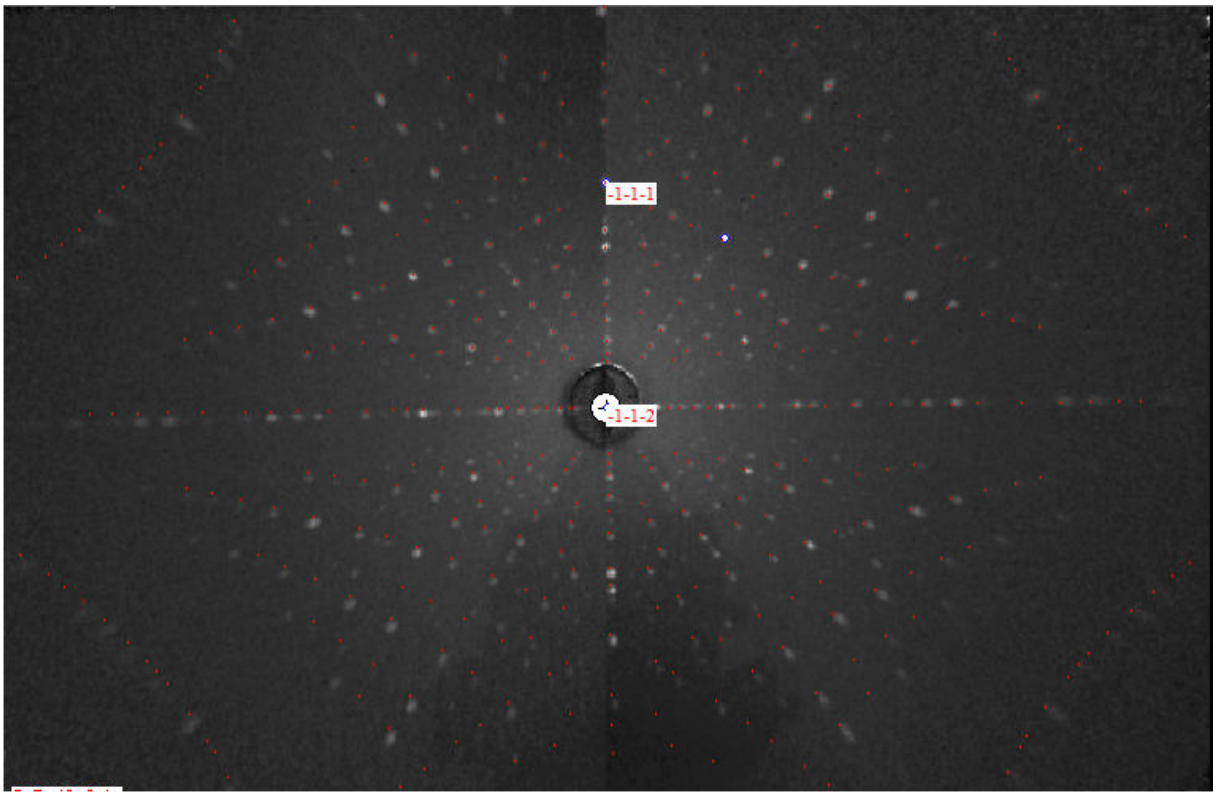

Figure 4.27: Laue image of the crystal shown in figure 4.26c; image provided by D. Kirschbaum and D. Zocco (IFP-TU Wien)

Table 4.2: Measured compositions (at.%) for $CeRu_4Sn_6$ crystals from SJ22 and SJ23. For comparison, the stoichiometric composition of $CeRu_4Sn_6$ is listed, showing that for crystals in both batches, the compositions deviate from the stoichiometry.

	Ce	Ru	Sn
stoichiometric composition	9.09	36.36	54.55
SJ22	9.6(3)	35.1(3)	55.3(4)
SJ23	9.6(2)	34.9(4)	55.5(3)

The optimal initial composition is Ce:Ru:Sn = 8.5:40:51.5 with pure Pb flux. The optimal temperature profile is holding 1150°C for 24 h and then cooling down to 850°C with a rate of 0.5°C/h. With this method a size of 0.7 mm could be reached. Fluxes from other elements that were tested here (Bi, In and Sn) did not give good results.

$Ce_3Ru_4Sn_{13}$ resistivity

In SJ03 several $Ce_3Ru_4Sn_{13}$ single crystals were found. This is noteworthy because in [31] it is stated that $Ce_3Ru_4Sn_{13}$ is the less stable compound as compared to the isostructural $CeRuSn_3$. Two of the synthesised crystals (SJ03-3 and SJ03-k, compositions see table 4.3) were used for resistivity measurements using a standard four-point technique.

Table 4.3: EDX-measured compositions (at.%) of $Ce_3Ru_4Sn_{13}$ samples SJ03-3 and SJ03-k

	Ce	Ru	Sn
SJ03-3	15.8	19.1	65.1
SJ03-k	15.8	18.7	65.5

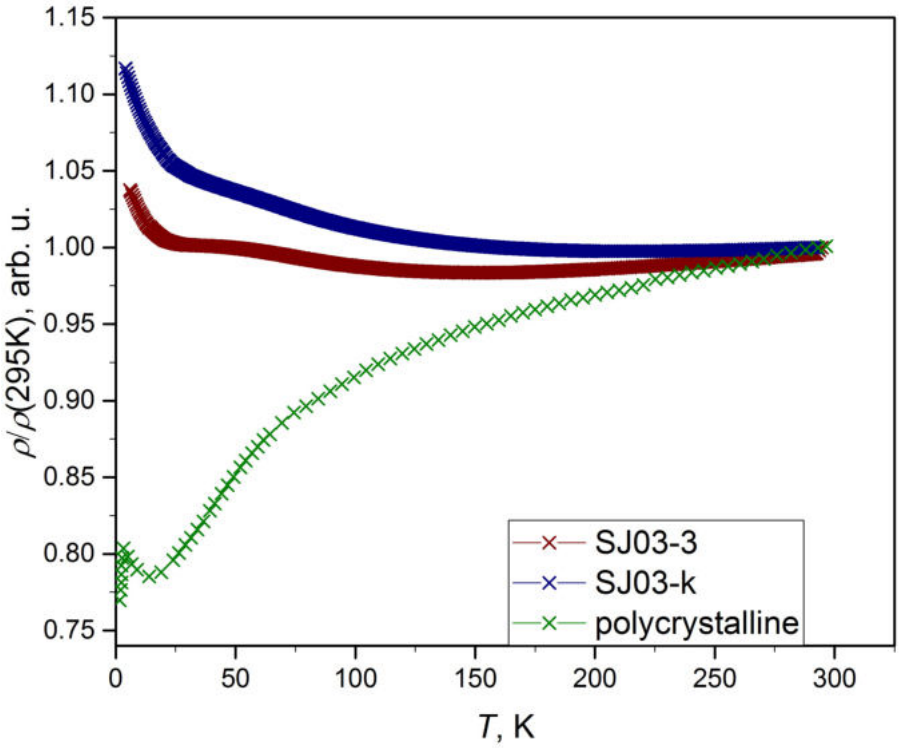

Figure 4.28: Resistivity curves of $Ce_3Ru_4Sn_{13}$. The data for the polycrystalline sample were extracted from [32]. The values are normalised to the values at 295 K. The original values are as follows: $\rho_{SJ03-3}(295\,K) = 311.13\,\mu\Omega cm$; $\rho_{SJ03-k}(295\,K) = 1267.54\,\mu\Omega cm$; $\rho_{polycrystalline}(295\,K) = 917.56\,\mu\Omega cm$.

In [32] a polycrystalline $Ce_3Ru_4Sn_{13}$ sample prepared by arc melting was investigated. Its resistivity curve has a significantly different shape than these two single-crystalline samples (see figure 4.28). Due to the non-regular shapes of the single-crystalline samples their measured absolute resistivity values cannot be deemed trustworthy. The higher resistivity of SJ03-k compared to SJ03-3 is probably correlated with a crack in the sample (see figure 4.29). All three samples show an upturn in the resistivity starting between 10 and 20 K. After the upturn there is a decreasing region in the polycrystalline sample. This temperature region is outside of the measurement range of the two single crystalline samples. The polycrystalline sample shows a metallic-like behaviour at higher temperatures while the two single-crystalline samples show a semiconductor- (or semimetal-)like behaviour. To interpret the difference between the polycrystalline sample and single crystals, more work should be done such as examining the stoichiometry, secondary phases and possible inclusions.

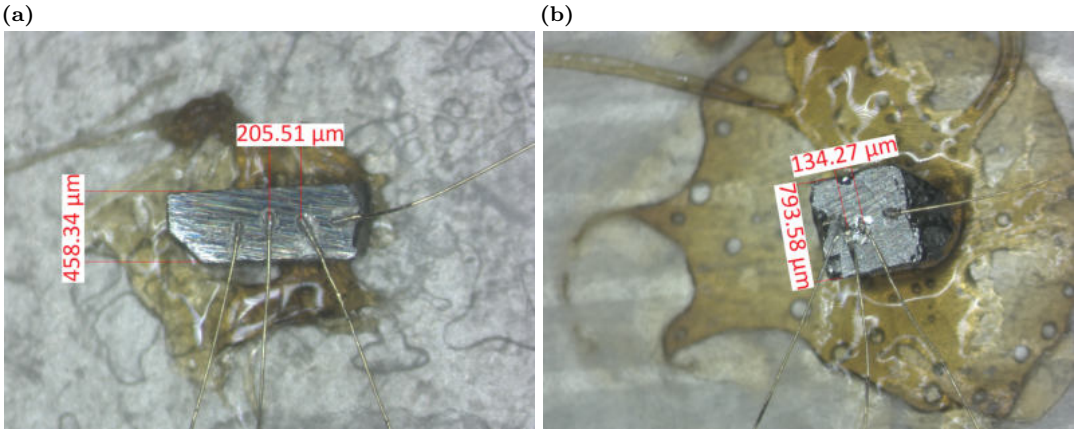

Figure 4.29: $Ce_3Ru_4Sn_{13}$ crystals with contacts for resistivity measurements: (a) SJ03-3 and (b) SJ03-k; a crack can be seen near the right upper corner.

4.5 Conclusion

In this chapter the growth and annealing of a $CeRu_4Sn_6$ single crystal, synthesised by the floating zone method, was described. The electrical transport properties were found to be only slightly influenced by annealing the sample. One of these effects was an expected increase of the mobility. This result shows that defects in the sample may not be the main cause for a low mobility in $CeRu_4Sn_6$ but instead the mobility could be intrinsically low. Additionally, the field-dependency of the resistivity was found to decrease, and also the magnitude of the energy gap differed before and after annealing. Further investigations on this sample are currently being made through ARPES measurements in order to obtain more clarity about the topological properties of this material (see figure 4.30). A question that remains to be answered is why the Hall resistivity changes its behaviour from linear to slightly non-linear through annealing, which might indicate a change in the band structure.

Additionally, the flux growth method was used to synthesise $CeRu_4Sn_6$ single crystals. After several experiments the following set of conditions could be found to produce high-quality single crystals of a size that makes Hall effect measurements possible. Crushed pieces of $CeRu_4Sn_6$ were mixed with additional Ru and Sn so that the molar ratio between Ce, Ru and Sn became 8.5:40:51.5. Pb flux was added in a molar ratio of 1:50. A low cooling rate of 0.5°C/h was chosen to enable growth of large-sized crystals of 0.6-0.8 mm. These crystals are currently being utilised for extensive physical property measurements. This series of experiments has shown that among the investigated flux compositions Pb was the most successful element for growing $CeRu_4Sn_6$ crystals.

The $Ce_3Ru_4Sn_{13}$ single crystals that were found in the course of the above-mentioned flux-growth experiments showed a substantially different resistivity behaviour than a previously measured polycrystalline sample. Based on the sparse knowledge about this compound an understanding of this behaviour could not yet be reached.

The Ce-Ru-Sn system shows significant potential for further investigations, in the above-mentioned compounds as well as others. Being a system built on a rare earth element it can be expected to possess many more attention-worthy features.

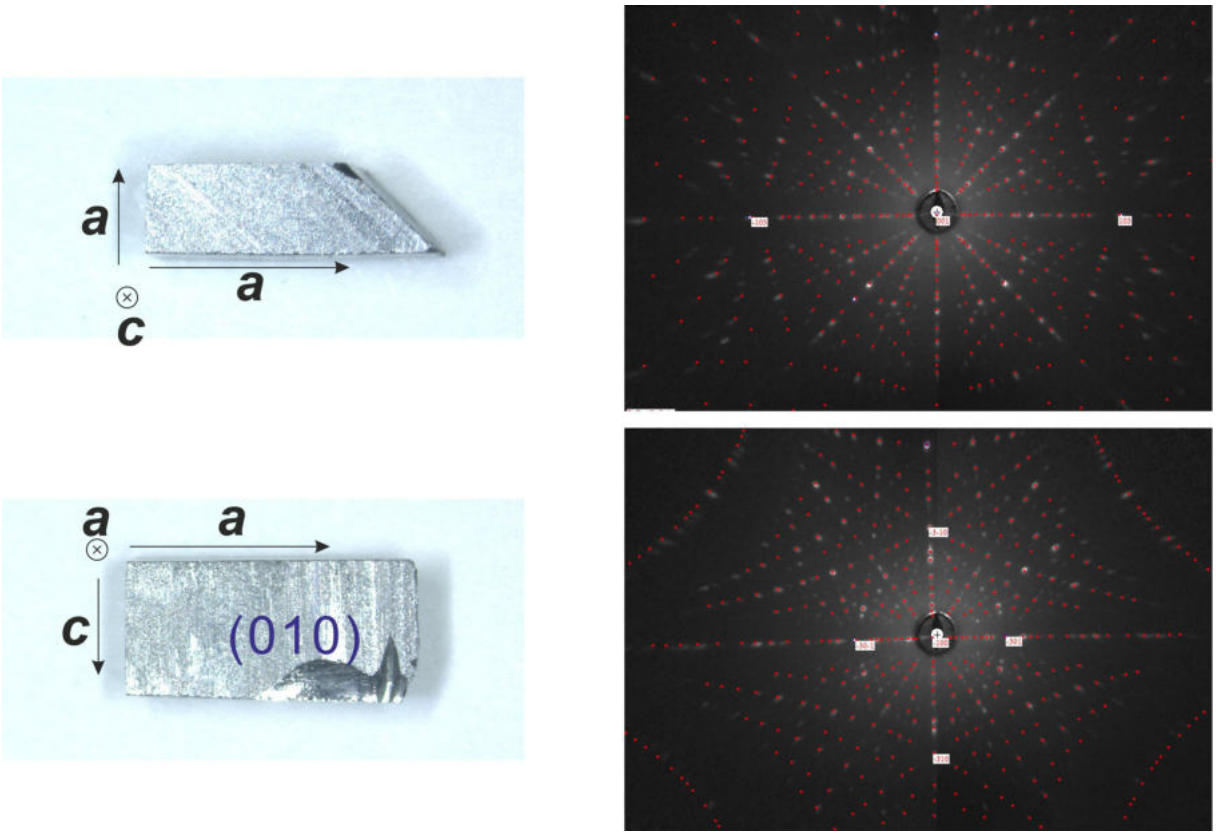

Figure 4.30: Photographs and Laue images of the $CeRu_4Sn_6$ sample that is being investigated by ARPES measurements

5 Half-Heusler compound CeBiPd

5.1 Introduction

The half-Heusler compound CeBiPd has not been investigated very deeply in the past. However, put into the context of heavily researched material classes like heavy fermion and topological insulator materials, it is a promising field to explore. Some preliminary analyses on the physical properties have been done, and basic crystallographic data have been collected [11]. However, from a materials scientific point of view many questions about crystal synthesis and properties remain unanswered. Widening the view to non-stoichiometric compounds, much remains to be discovered.

In [12] four sample batches were produced to grow CeBiPd single crystals by flux growth. The resistivity curves of the resulting crystals showed substantial differences between the batches. A more thorough investigation will here be conducted to improve the understanding of the relation between the synthesis process, crystal chemistry and physical properties.

The first question that will hence be addressed is whether the observed physical properties are intrinsic. Another question concerns the impact of the composition on the physical properties. Therefore in this section the sensitivity of the material's resistivity to variations in the composition will be examined. Additionally, insights into other properties of this not-so-well-known material gained in the course of these studies will be presented.

The strategies used in this section were developed considering the small amount of knowledge in existence about the ternary system Ce-Bi-Pd. Some of the minor problems met during this research concerned the material properties – for example, several samples broke during preparation due to material brittleness. Another example is that the crystals are sensitive to air and moisture which thus requires specific methods in handling.

The following sections will cover the two different synthesis methods used, the physical property measurements of the resulting samples and additional findings.

5.2 Polycrystalline CeBiPd samples

The aim of producing polycrystalline samples was to investigate the phase constitution in alloys of different initial compositions, which is crucial to guide the single crystal growth, since no information on the phase diagram of the Ce-Bi-Pd system is available in the literature.

High-purity elements Ce, Bi and Pd were mixed in three different ratios for syntheses in the HF furnace (see table 5.1). An amount of Bi evaporates each time during heating to high temperatures. Therefore the elements were repeatedly melted together, measuring the weight loss and adding an adequate amount of Bi for the loss. After the final melting the deviation from the target weight of each sample was smaller than 0.6 wt.%. The sample name CPB2 will be used in the following for this series of samples.

Each of the resulting samples was split into two parts. One part was annealed at $T_{ann} = 800^{\circ}\mathrm{C}$ and the other part at 900°C for eight days. After annealing XRD and EDX measurements were performed for all six pieces.

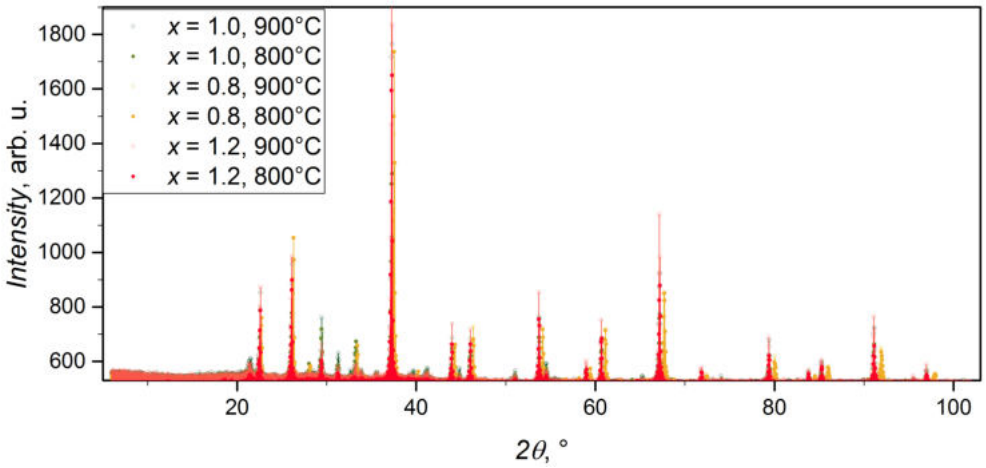

Figure 5.1: A comparison of the XRD patterns of each of the CPB2 samples ($CeBiPd_x$). It can be seen that all patterns contain the same main peaks but at slightly different angles, indicating different lattice parameters.

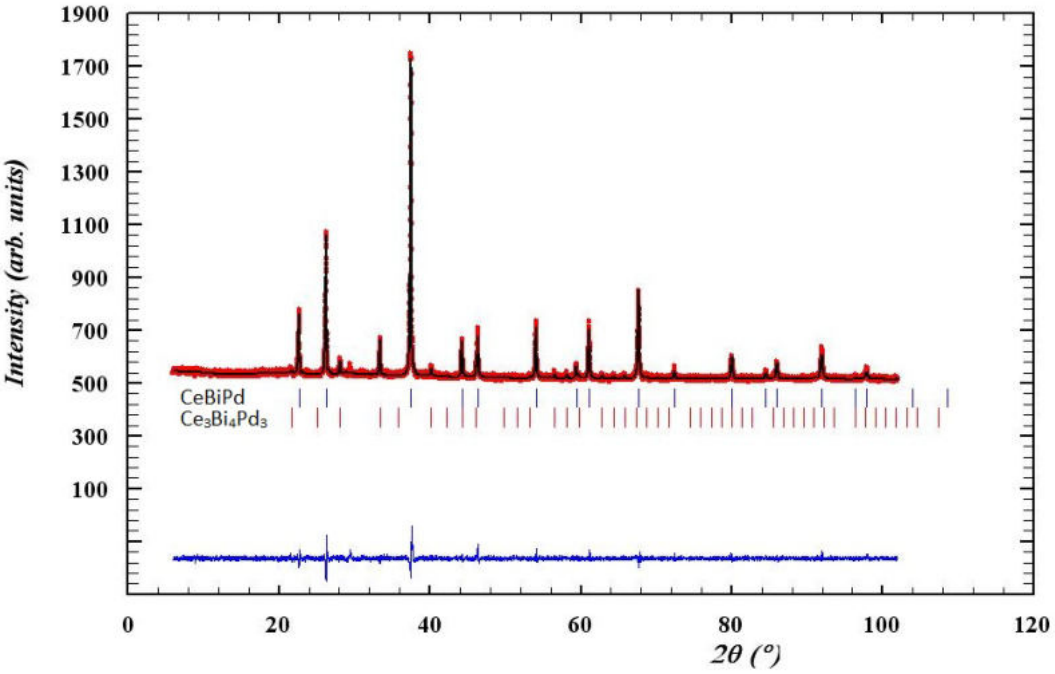

Figure 5.2: Pattern fit by Rietveld refinement for the annealed (800 °C) sample $CeBiPd_{0.8}$. Two types of phases were indexed and an unknown phase can be seen.

Phase identifications by SEM imaging of all six samples are presented in the following. Unless otherwise indicated, the backscatter electron images are shown. The element atomic percentage in each phase from the EDX measurements of the indicated points are shown.

(a)

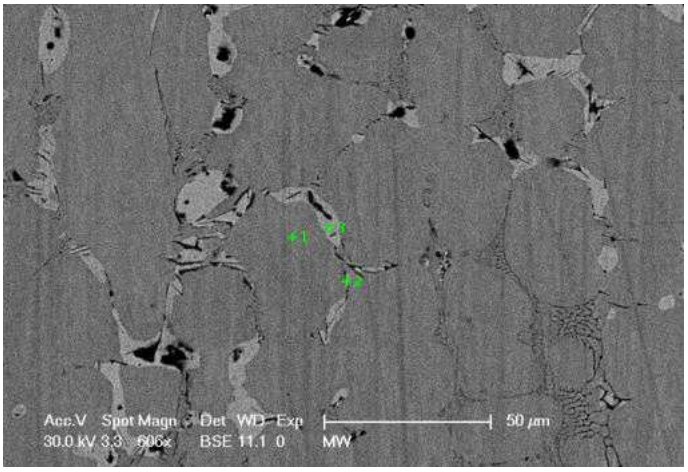

(b)

	Phase	Ce	Bi	Pd
1	CeBiPd	35.6	36.7	27.7
2	CeBi	52.6	37.4	10.0
3	$Ce_3Bi_4Pd_3$	31.5	41.1	27.4

(c)

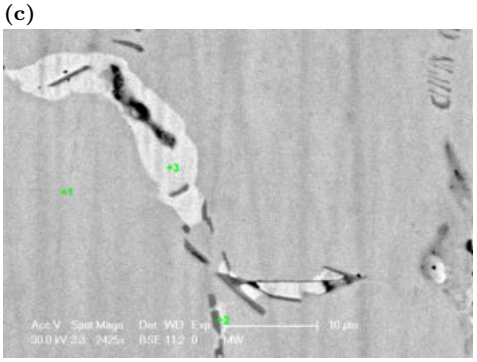

Figure 5.3: $CeBiPd_x$ with $x = 0.8$, $T_{ann} = 800°C$. (c) is an enlarged detail of (a)

(a)

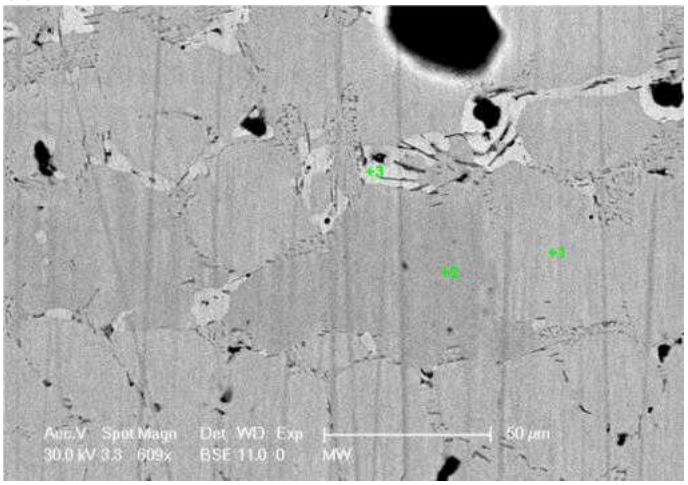

(b)

	Phase	Ce	Bi	Pd
1	CeBiPd	34.2	35.6	30.3
2	CeBiPd	34.9	34.8	30.3
3	$Ce_3Bi_4Pd_3$	30.7	41.2	28.2

Figure 5.4: $CeBiPd_x$ with $x = 0.8$, $T_{ann} = 900°C$

(a)

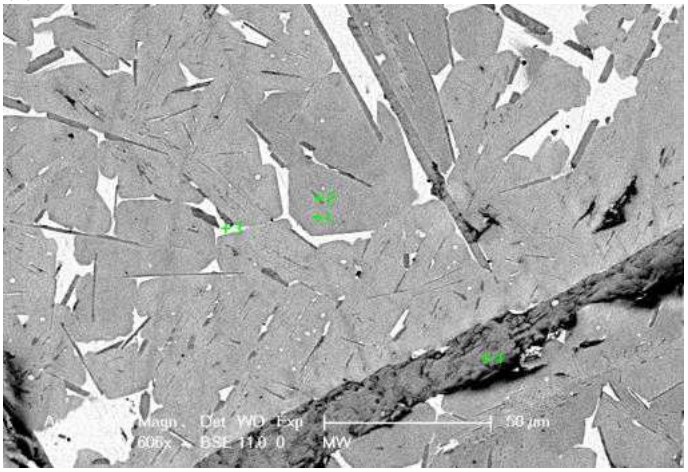

(b)

	Phase	Ce	Bi	Pd
1	CeBiPd	32.8	32.8	34.4
2	Ce_2Bi	53.6	34.7	11.7
3	BiPd	5.8	46.5	47.7
4	Ce_2Bi	66.8	33.2	0

(c)

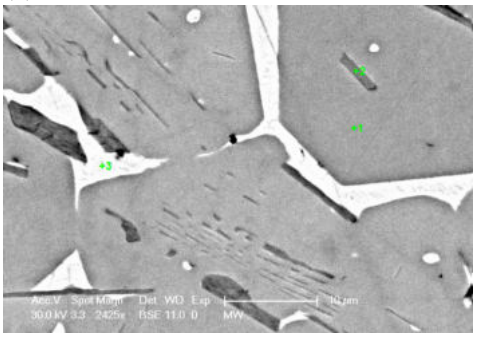

Figure 5.5: $CeBiPd_x$ with $x = 1.0$, $T_{ann} = 800°C$. (c) is an enlarged detail of (a)

(a)

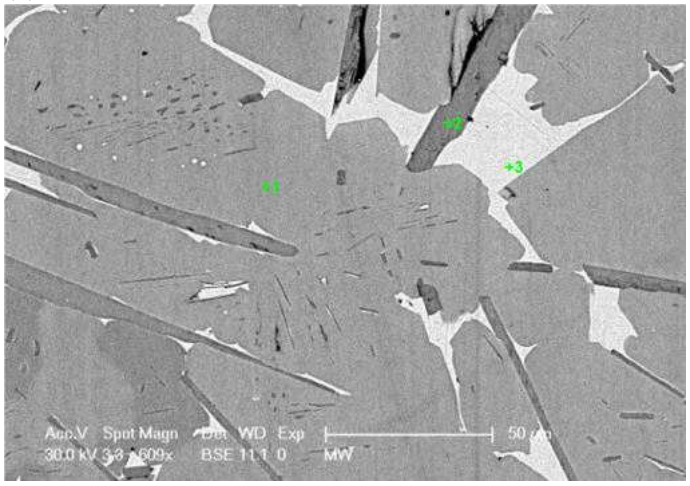

(b)

	Phase	Ce	Bi	Pd	O
1	CeBiPd	32.9	32.7	34.4	
2	Ce_2BiO_4	28.2	14.9	0.2	56.7
3	BiPd	3.6	47.3	49.2	

Figure 5.6: $CeBiPd_x$ with $x = 1.0$, $T_{ann} = 900°C$. The O content in the measurement of point number 2 is an estimation.

(a)

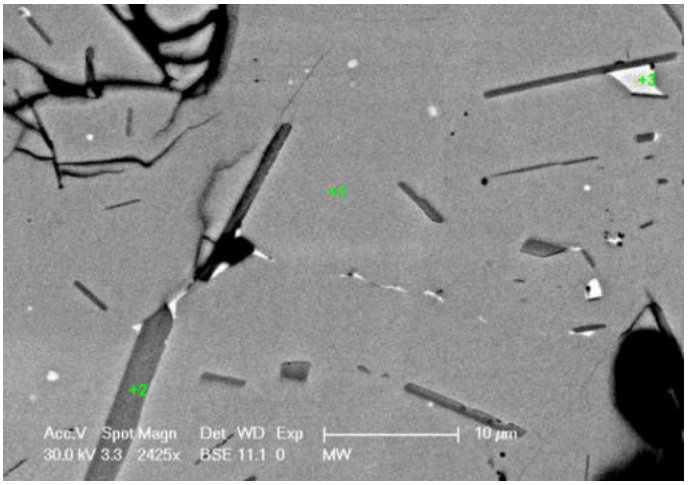

(b)

	Phase	Ce	Bi	Pd
1	CeBiPd	32.2	33.1	34.7
2	Ce_2Bi	61.7	34.4	3.9
3	BiPd	6.1	43.5	50.4

(c)

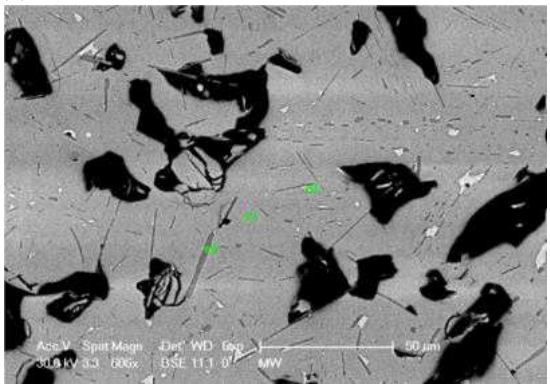

(d)

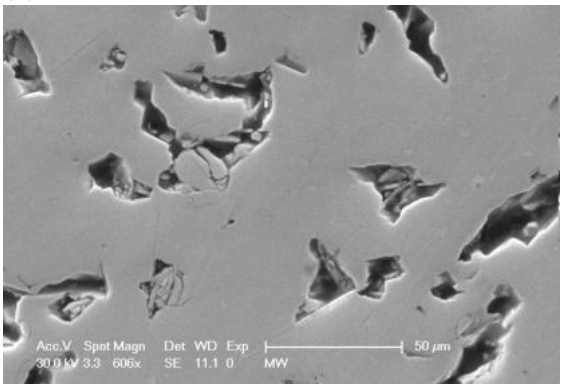

Figure 5.7: $CeBiPd_x$ with $x = 1.2$, $T_{ann} = 800°C$. The black regions in (c) are holes in the sample (see secondary electron image in (d)). (a) is an enlarged detail of (c)

(a)

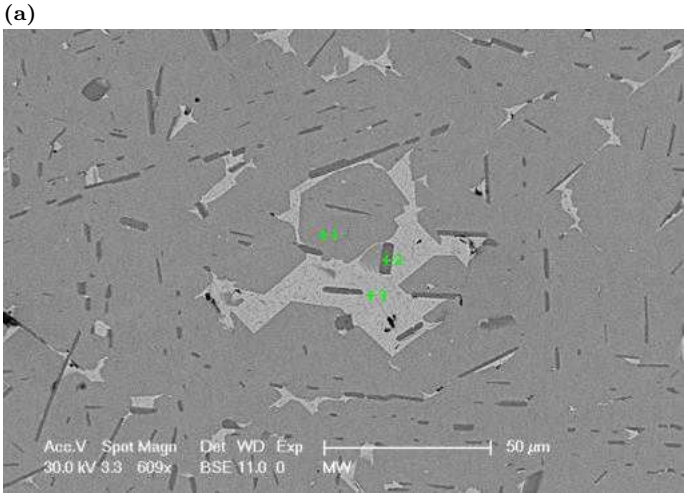

(b)

	Phase	Ce	Bi	Pd
1	CeBiPd	31.9	33.6	34.5
2	Ce_2Bi	61.4	37.3	1.3
3	BiPd	4.3	45.7	50.0

Figure 5.8: $CeBiPd_x$ with $x = 1.2$, $T_{ann} = 900°C$

Table 5.1: Sample compositions (in at.%) for the CeBiPd-type phase from EDX measurements. Lattice parameters (in Å) were calculated from the XRD data using Rietveld refinement.

Sample – $CeBiPd_x$		Ce	Bi	Pd	computed lattice parameter
$x = 0.8$	starting composition	35.71	35.71	28.57	
	$T_{ann} = 800°C$	35.6	36.7	27.7	6.77538(25)
	$T_{ann} = 900°C$	34.5	35.2	30.3	6.77975(29)
$x = 1.0$	starting composition	33.33	33.33	33.33	
	$T_{ann} = 800°C$	32.8	32.8	34.4	6.82292(38)
	$T_{ann} = 900°C$	32.9	32.7	34.4	6.82409(26)
$x = 1.2$	starting composition	31.25	31.25	37.5	
	$T_{ann} = 800°C$	32.2	33.1	34.7	6.82257(26)
	$T_{ann} = 900°C$	31.9	33.6	34.5	6.82601(21)

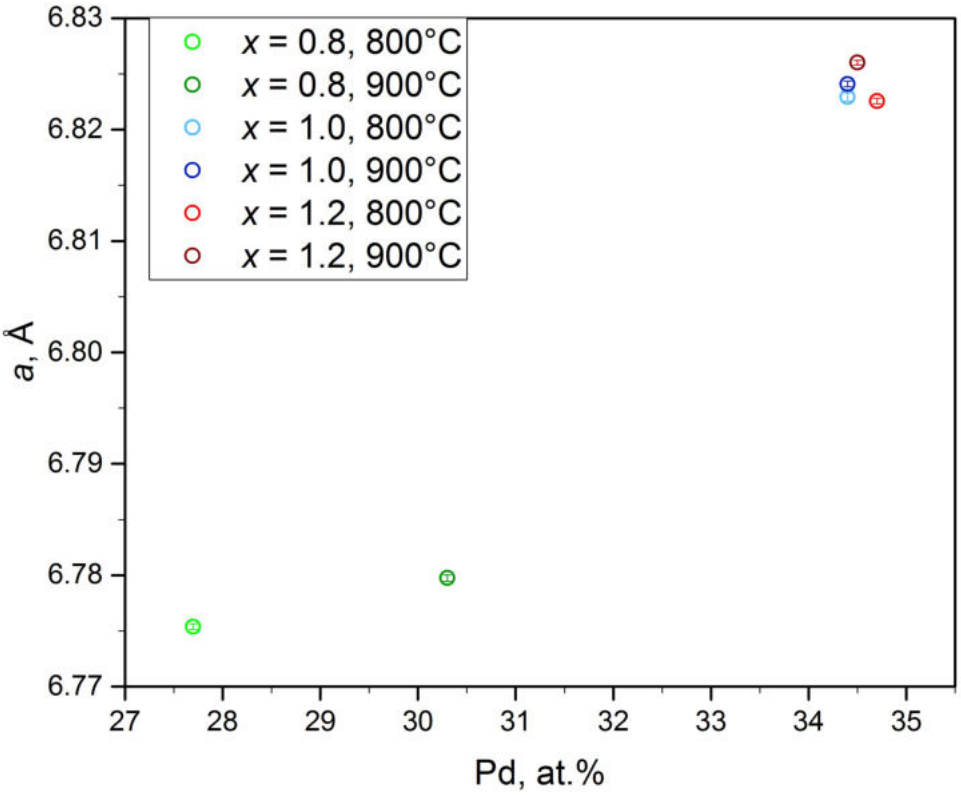

Figure 5.9: The relation between measured Pd content (from EDX) and lattice parameter (from XRD) of the CeBiPd-type phases in the CPB2 samples ($CeBiPd_x$).

The first conclusion to draw from the XRD as well as EDX measurement results is that all of these samples contain more than one phase. As we can see from SEM images in figures 5.3 to 5.8, and an example of the refined XRD pattern of the $x = 0.8$, $T_{ann} = 800°C$ sample shown in figure 5.2, several phases are present in addition to CeBiPd. Therefore these samples are unsuitable for investigating physical properties.

The comparison of the XRD patterns of the samples $CeBiPd_x$, $x = 0.8, 1, 1.2$ (see figure

5.1) leads to another conclusion. The samples with $x = 1$ and 1.2 exhibit peaks in their XRD patterns in very similar positions. The peaks of the sample with $x = 0.8$ are located at higher angles. This means that the CeBiPd phase in $x = 0.8$ has a smaller lattice parameter than those in $x = 1$ and $x = 1.2$ (see table 5.1). These results indicate that the Pd content in the CeBiPd phase can be less than 35 at.% but more than 27.5 at.%. Depending on the annealing temperature, the phase region can change from 27.5 at.% to 34.7 at.% Pd for $T_{ann} = 800°C$, and from 30.0 at.% to 34.4 at.% Pd for $T_{ann} = 900°C$.

Further, we note that the lattice parameters of the CeBiPd in the samples with a lower Pd content are smaller than those of the stoichiometric samples. Together with the fact that the atomic radius of Pd is the smallest out of the three involved elements, it becomes clear that missing Pd atoms appear as vacancies in the crystal structure rather than being substituted by any of the other two elements.

5.3 Flux growth of CeBiPd single crystals

Single-crystalline samples that are necessary for certain physical property measurements were produced in Pb flux. In previous investigations an atomic ratio of Ce:Bi:Pd = 3:3:5 was used as the initial composition. The ratio of the sample volume to the Pb flux was 45:55. The temperature programme consisted of heating to 1100°C, staying at that temperature for 12 hours, cooling down to 1050°C with a rate of 5°C/h and finally cooling down to 900°C with a rate of 1°C/h. In this work the above process was replicated, as well as conducting experiments using different starting compositions. The aim of this strategy was to obtain samples with different Pd contents.

The preparation of the samples was conducted as follows: First an appropriate amount of Ce and Pd were weighed and melted together in the HF furnace. Subsequently this mixture, together with the calculated amounts of Bi and Pb were filled into an alumina crucible. The procedure continued as described in 2.2.2.

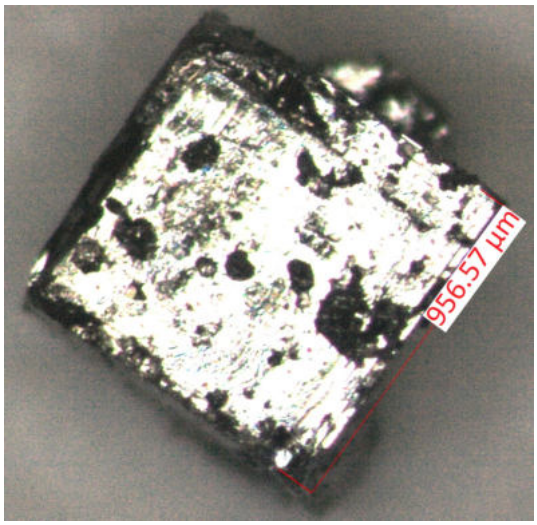

Figure 5.10: As-grown CeBiPd crystal CPB4d

The resulting sample qualities vary in several respects. Some of the produced crystals have sizes of a few millimetres, which is very favourable for conducting physical property measurements. However, they often contain impurities, for example Pb inclusions or inclusions of Pb

alloys. These are often undetectable until revealed by metallography or EDX measurements, or by physical property measurements.

There are many factors in the crystal growth influencing the quality of the resulting crystals. Unfortunately, a control of the outcomes of the experiments could not be achieved with the techniques available. The crystal size and shape are two examples showing only a weak dependence on the starting composition. Nevertheless, some advances towards the answering of the initial questions could be made, which will be presented in the following section.

The experiments in this series and their results are listed in table 5.2. The lattice parameter of the half-Heusler phase in some batches changes from crystal to crystal (e.g., in the batch CBP4 we see two types of lattice parameters; as in the other batches with an initial Pd content below 33.3 at.%). The cause for this is that crystals grown at high temperatures have different compositions than at low temperatures, as indicated in the annealed samples presented in the previous section. Compositional inhomogeneity can also be seen in the same crystal, since it has grown from high to low temperatures (see figure 5.11).

(a)

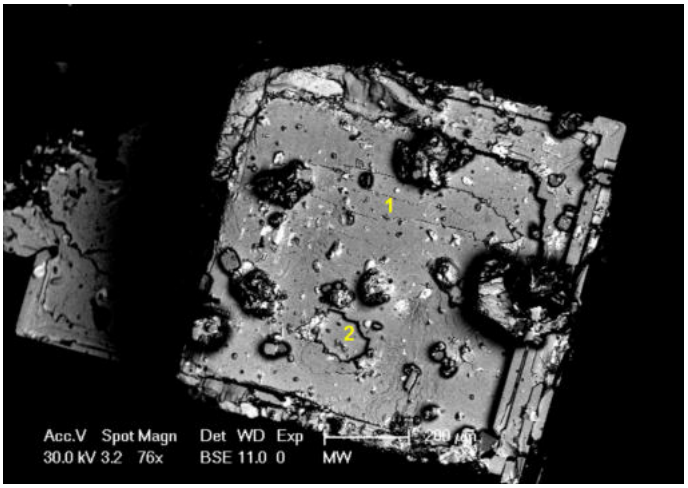

(b)

Measured point	Ce	Bi	Pd
1	32.9	36.9	30.2
2	33.0	36.7	30.3
Mean value	**32.9(0)**	**36.8(1)**	**30.3(1)**

(c)

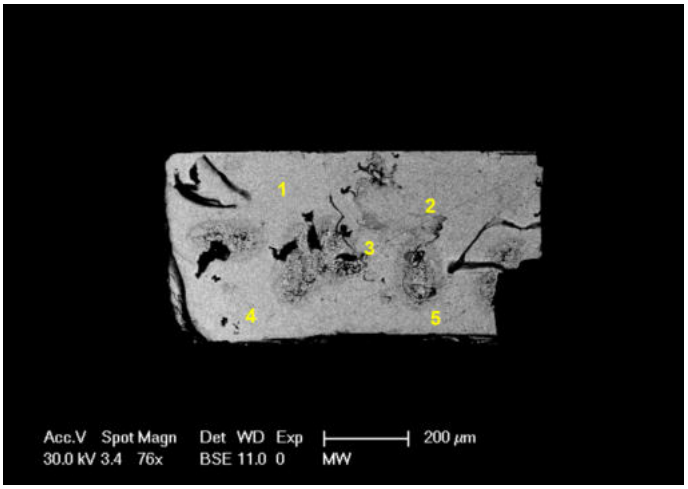

(d)

Measured point	Ce	Bi	Pd
1	36.2	35.4	28.4
2	35.9	35.2	28.9
3	36.1	35.4	28.5
4	36.0	36.3	27.7
5	35.6	35.7	28.7
Mean value	**36.0(2)**	**35.6(4)**	**28.4(4)**

Figure 5.11: SEM images of the CeBiPd crystal CPB4d, (a) as-grown surface with compositions in (b), (c) after grinding and resistivity measurement, compositions in (d). The composition is different between the outermost layer of the crystal and inside.

Table 5.2: An overview of all flux grown CeBiPd samples. The starting composition varies with the Bi content and/or Pd content. The measured compositions (in at.%) are calculated from averaging different points of each sample from EDX measurements. The lattice parameters (in Å) are computed from the XRD refinements. In CPB8 only the surface consists of single-phase CeBiPd, therefore no data can be given for a bulk composition. Samples CPB9 and 10 consist of single- and double-phase regions (see 5.5). Here only the CeBiPd single phase was considered in the EDX measurement results.

Sample name	Starting composition, molar			Starting composition, at.%			Measured composition, at.%			Lattice parameter(s), Å
	Ce	Bi	Pd	Ce	Bi	Pd	Ce	Bi	Pd	
CPB1	3	3	5	27.3	27.3	45.5	34.0	33.3	32.6	6.80088(57)
CPB3	3	3	3	33.3	33.3	33.3	30.4	44.3	25.3	6.79780(81)
CPB4	3	3	2.8	34.1	34.1	31.8	33.6	35.4	31.0	6.7957(12) 6.76709(28)
CPB5	3	3	6	25	25	50	34.4	33.4	32.2	6.80137(23)
CPB6	3	3	2.5	35.3	35.3	29.4	35.1	33.6	31.3	6.74301(29) 6.78301(30)
CPB7	3	4	6	23.1	30.8	46.2	33.4	28.6	38.0	6.80221(19)
CPB8	3	4	2.5	31.6	42.1	26.3	–	–	–	6.75167(58) 6.79687(59)
CPB9	3	4	3	30	40	30	36.6	36.4	27.1	6.75604(89)
CPB10	3	4	3.5	28.6	38.1	33.3	36.5	36.0	27.5	6.76733(22)
CPB11	3	4	5	25	33.3	41.7	34.7	33.8	31.5	6.79339(38)

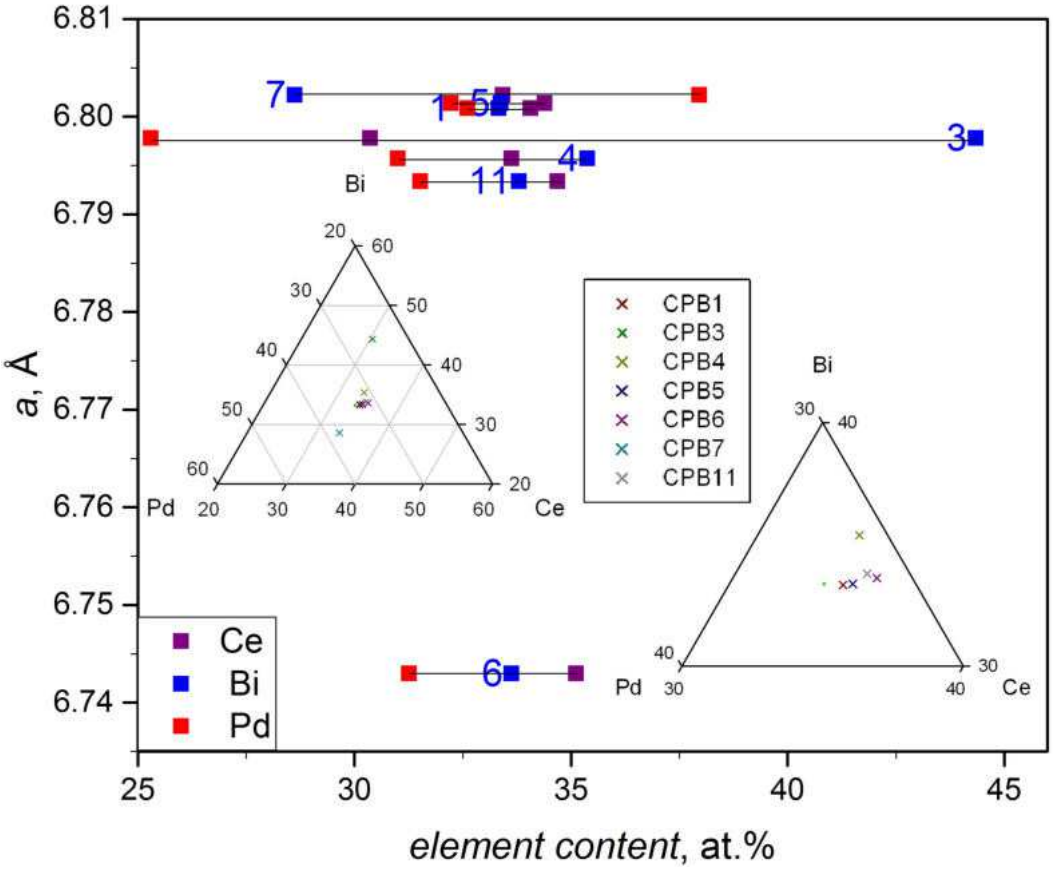

Figure 5.12: The relation between lattice parameters a and compositions of the CeBiPd samples (CPB). Each line represents the sample indicated by the number. For batches that contain crystals with different lattice parameters the value corresponding to the highest volume fraction was chosen. The squares connected by the line signify the atomic percentage of the respective element in the crystal. The green dots in the ternary diagrams indicate the composition of stoichiometric CeBiPd.

It can be seen that crystals with a near-stoichiometric composition of CeBiPd can be obtained by using the starting composition of CPB1. In the subsequent experiments the growth of crystals with varying Pd content was attempted. However, the following two samples (numbers 3 and 4) show resulting compositions deviating from outcomes anticipated from the initial compositions. Not only the Pd content varies in these samples, but also the Bi content, which was expected to stay in a fixed relation to the Ce content. A lattice parameter as high as in the HF furnace produced samples (see figure 5.9) could not be reached.

Since batches 5 and 6 resulted in crystals with a lower Bi than Ce content the following batches (7 and 8) were produced using a higher Bi concentration in the initial composition. As can be seen in the EDX results this effect was not achieved between sample 5 (initial composition 3-3-6) and 7 (in. comp. 3-4-6). The change from a composition of 3-3-2.5 (sample 6) to 3-4-2.5 (sample 8) resulted in the growth of an unexpected two-phase crystal (see section 5.5).

CPB7 is the only sample with a higher Pd content than both of the other elements. This could be caused by Pd substituting the other elements at their respective sites. The higher amount of Bi in the initial composition could have made favourable circumstances for the formation of CeBi which could have caused an excess of Pd in the remainder of the volume. It is remarkable that this sample is the only one in the series at hand to exhibit this effect.

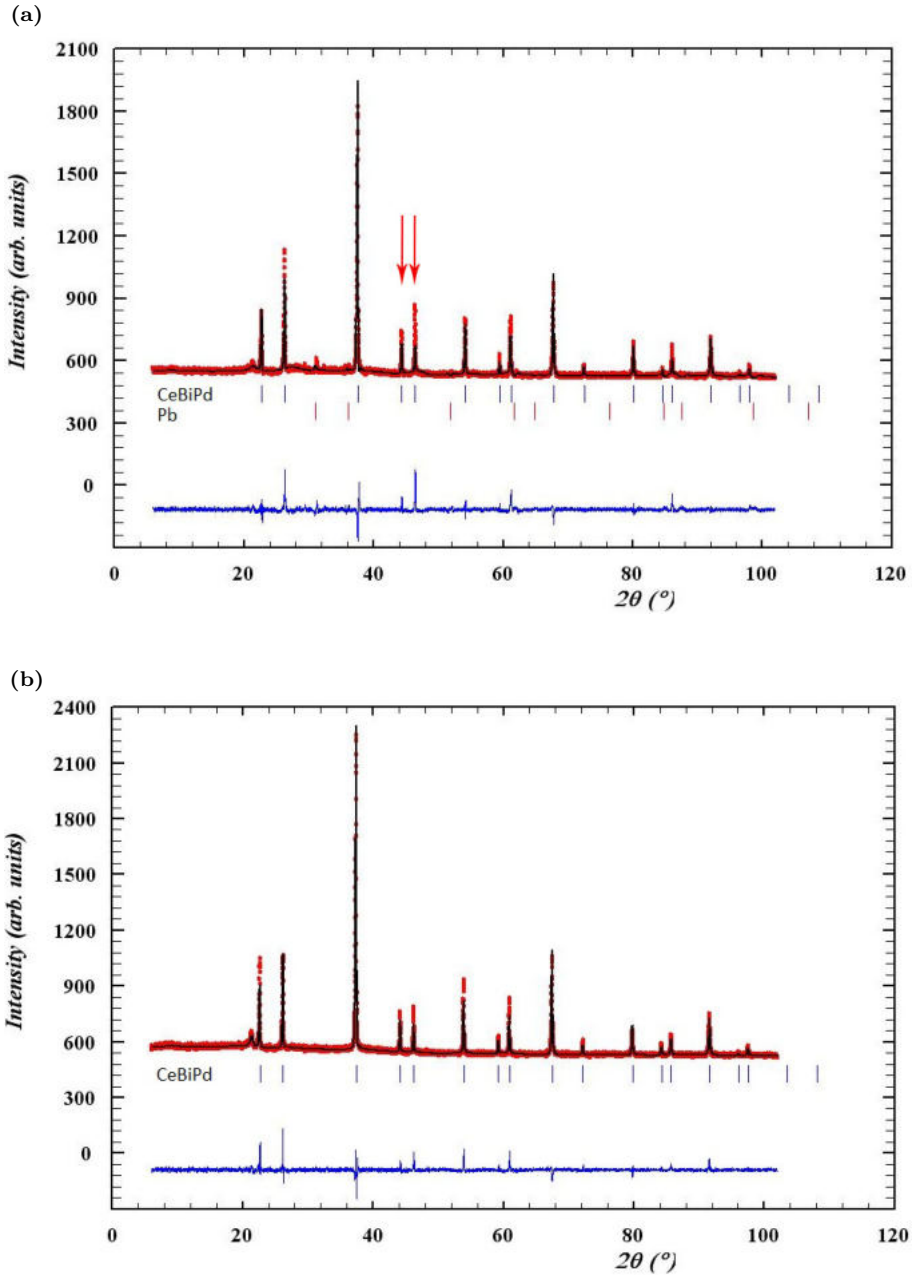

Figure 5.13: XRD patterns of the sample batches (a) CPB10 and (b) CPB11. The arrows indicate peaks that show different height/intensity differences in different samples.

Two peaks are marked in the XRD patterns presented in figure 5.13. Their height difference deviates from the height difference of the same peaks calculated by Rietveld refinement of the XRD pattern (black lines in the figures). This may be due to unequal occupation of the Pd and Bi sites in the real crystal.

An investigation by single crystal x-ray diffraction could reveal more extensive knowledge about the crystal structure, including occupancies and temperature factors of this compound.

As CeBiPd is sensitive to air, measures against oxidation had to be implemented when han-

dling the samples. Exposure to air as well as water or heat should be avoided as much as possible. Some modifications of the sample preparation procedures were made.

When attaching the sample to a holder for grinding, superglue was used instead of resin that has to be heated for use.

Usually water cooling is used in the grinding process. To avoid contact with water this was not done here. Instead the grinding was executed in shorter intervals to avoid overheating.

Some heating of the sample could, however, not be avoided when attaching gold wires for measurements. Most samples were contacted using spot welding, and some using a two-component glue which requires heating. An alternative without heating, a one-component glue, was tested but unsuccessful.

5.4 Physical property measurements

5.4.1 Resistivity measurements

The resistivity of several large crystals from the flux grown sample series was measured. These crystals were selected in consideration of showing phase purity in the EDX measurements and therefore on the surface.

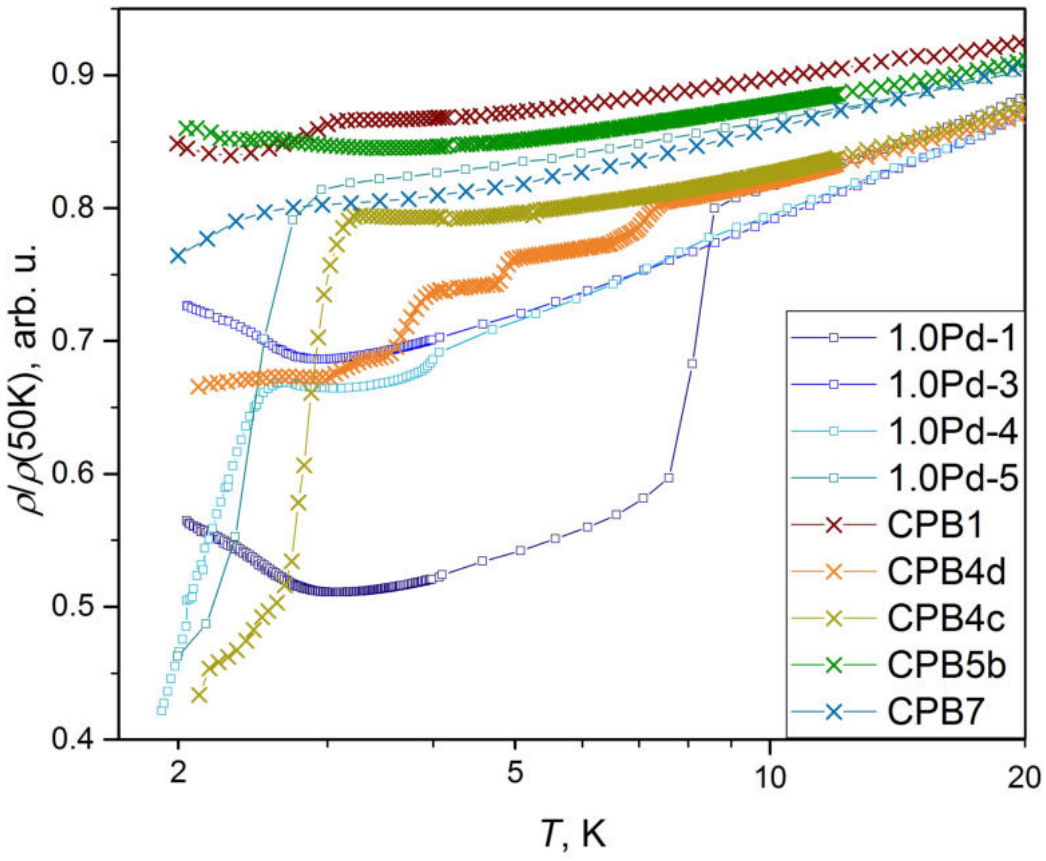

Figure 5.14: Low-temperature resistivity of CeBiPd samples (crosses) and resistivity data of CeBiPd samples from [12] (squares). Values were normalised to the value at 50 K.

The results can be seen in figure 5.14 for low temperatures and in figure 5.15 for the whole temperature range. All of the curves except for CPB7 were taken with a standard four-point

technique. The curve for CPB7 was taken from the Hall-effect measurements carried out on the Quantum Design PPMS (see section 5.4.2).

All samples show a slightly decreasing resistivity with decreasing temperature and a change in the slope at around 3 K. This change is a kink for CPB1, 4c and 4d, a minimum for CPB5b and in the curve of CPB7 there is an inflection point at this temperature. The most pronounced effect can be seen in CPB4c, which shows an abrupt fall in the resistivity. In the curve of CPB4d several kinks can be seen. Some of the samples show slight upturns at the lowest temperatures.

Table 5.3: Compositions of the CeBiPd samples in figure 5.14 measured by EDX (at.%) and atomic ratios

Sample	Ce	Bi	Pd	Ce:Bi:Pd
CPB1	34.1	33.3	32.6	1:0.98:0.96
CPB4d	36.0	35.6	28.4	1:0.99:0.79
CPB4c	33.2	35.0	31.8	1:1.05:0.96
CPB5b	34.2	33.3	32.5	1:0.97:0.95
CPB7	33.4	28.6	38.0	1:0.86:1.14

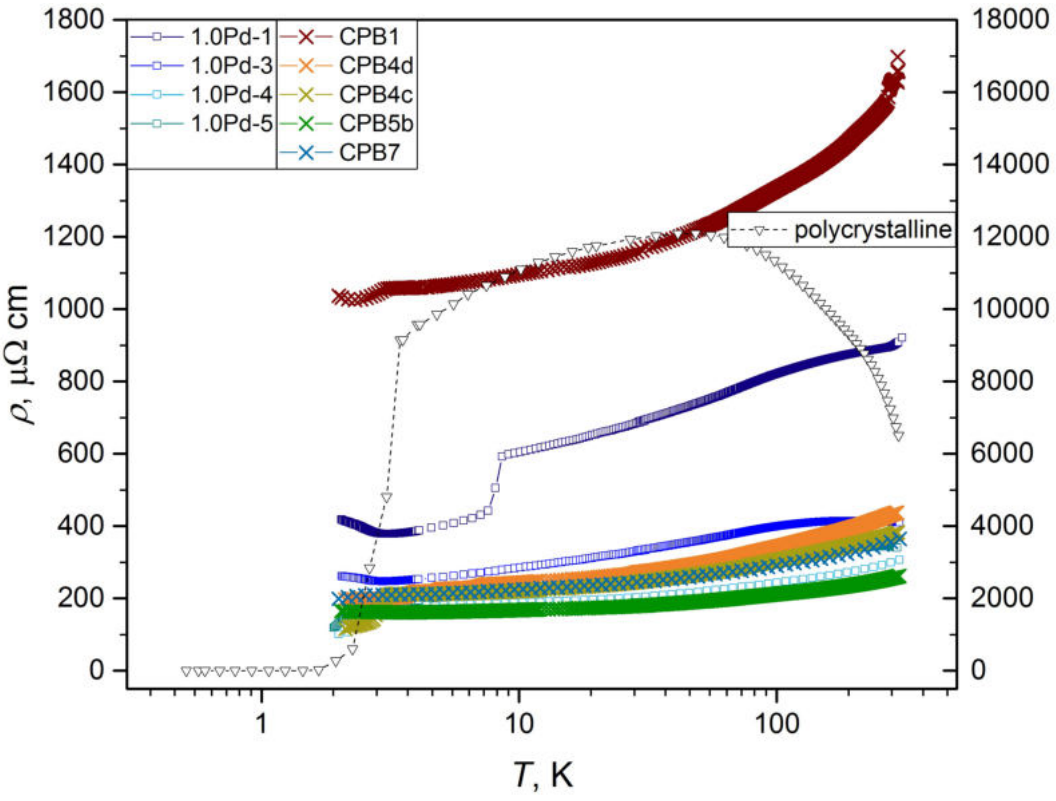

Figure 5.15: Resistivity of CeBiPd samples (crosses) with samples from [12] (squares) and a polycrystalline sample (data extracted from [9]. The right-side axis pertains to the polycrystalline sample. The CPB1 curve shows considerably higher values than the other CPB samples. Possible reasons are micro-cracks or inclusions in the crystal.

Comparing with [12], the slopes at higher temperatures are very similar in all samples. Like the CPB samples, all of the 1.0Pd-x samples have a kink or minimum at around 3 K. 1.0Pd-4 and -5 decrease steeply after a kink, like CPB4c. 1.0Pd-1 and -3 show similar upturns to CPB1 and 5b.

The resistivity of the polycrystalline sample studied in [9] steeply increases at first with decreasing temperature, contrary to the other samples in figure 5.15. At 3.5 K there is a kink and below 1.5 K the sample becomes superconducting.

The compositions of the CPB samples of this measurement series are shown in table 5.3. CPB1 and 5b, which have very similar compositions, both show upturns in the resistivity at low temperatures. However, clear conclusions cannot be drawn on the correlation between composition and resistivity.

Possible extrinsic influences on the resistivity curves

Since the samples were only measured by EDX prior to the resistivity measurements there could easily be inclusions in the bulk of the crystals. Often the first measured resistivity curve of a sample shows a kink at approximately 7 K. This suggests that some Pb from the flux is in the sample and influences the resistivity behaviour of the sample.

Oxidation can be another cause for extrinsic influences. Measures were taken to avoid possible oxidation as much as possible but it cannot be ruled out completely.

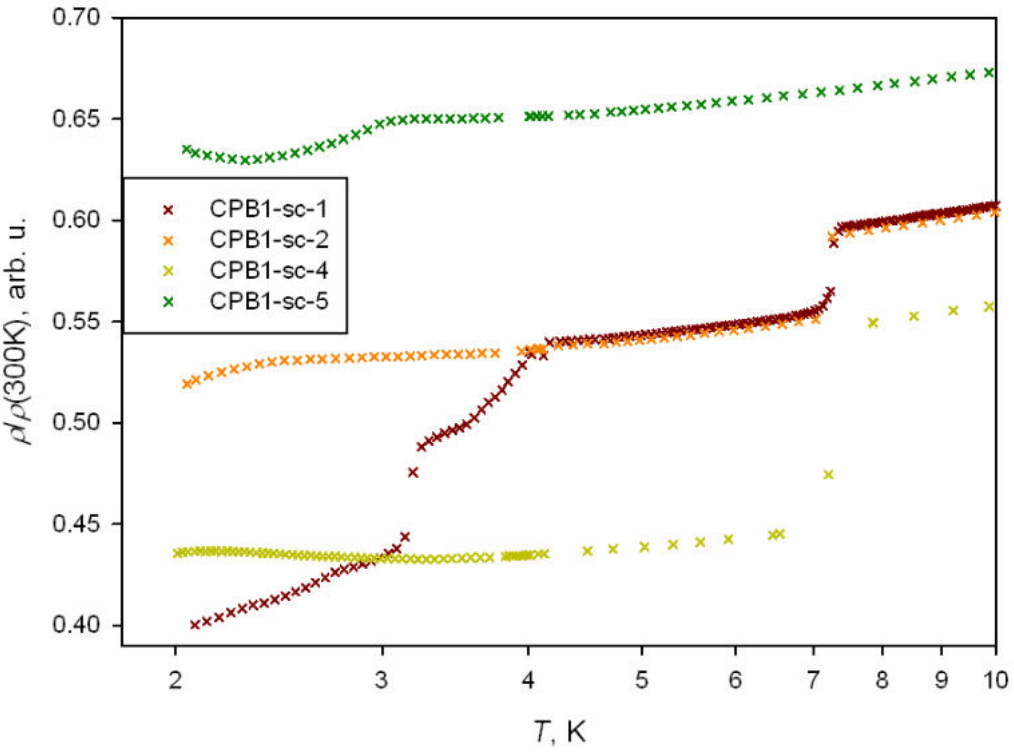

Figure 5.16: Resistivity data of the CeBiPd sample CPB1 taken at different stages of phase purity. Values normalised to the value at 300 K.

In the process of obtaining the resistivity curves several samples were measured more than once. When discovering hints of extrinsic influences a grinding process was repeated on the sample surface and then the resistivity was measured again. Figure 5.16 shows a sequence of resistivity measurements on CPB1. The first measured curve shows several steps. The contacts

were attached to the corresponding sample by a two-component silver paste which requires heating (150°C for 20 min) to achieve solidification. The exposure of the sample to this heat is a possible cause for the steps in the resistivity. All steps except for the one at 7 K disappear in the next measurement. In CPB1-sc-4 the overall resistivity value is lower due to a higher concentration of Pb inclusions, as also seen in the larger jump at 7 K. The last measured curve only shows a kink at around 3 K and is thus considered to be free of Pb inclusions.

5.4.2 Hall-effect measurements

Based on sample quality according to the above resistivity measurements and visual assessment, CPB5b and CPB7 were chosen to be used for Hall-effect measurements. The results of these measurements are shown in figure 5.17 and figure 5.19.

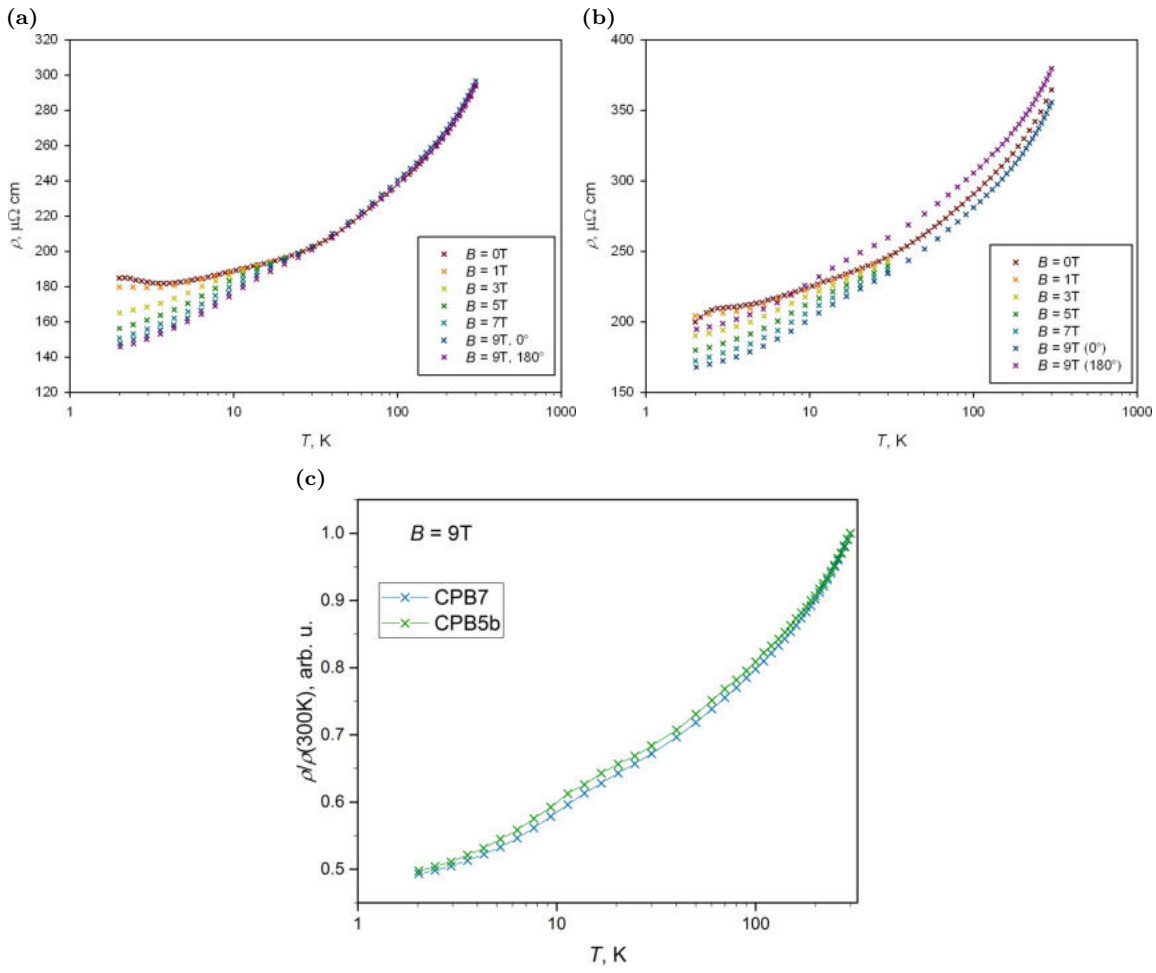

Figure 5.17: Resistivity of the CeBiPd samples (a) CPB5b and (b) CPB7; (c) resistivity curves of CPB5b and CPB7 at $B = 9\,\mathrm{T}$. Each of the curves in (c) is the average of the curves taken at 0° and 180° positions.

Both samples show a decreasing resistivity with decreasing temperature. This decrease is continuously slowing down with no applied magnetic field. Around 3 K both samples have a nearly-flat region. Below 3 K CPB5b shows an upturn and CPB7 another decrease. However,

this difference vanishes with an applied magnetic field, as shown in figure 5.17c. The resistivity curves become remarkably similar despite the difference in the compositions of the samples.

An applied magnetic field causes the resistivity curves of both samples to have a steeper slope at low temperatures. In increasing fields the slope shows less variation. At the highest field (figure 5.17c) the change of the slope is very subtle. A hump can be seen in the region of 20 K.

The mismatch of the two curves taken at 9 T in the CPB7 graph is caused by the misalignment of the electrical contacts of the sample. This also has an effect on the curves taken at different magnetic fields. However, the shapes of these curves show that the decrease of the resistivity with a magnetic field is also present in this sample.

In figure 5.18 a comparison of the resistivity measurements on CPB5b in the home-made device GUNDI and in the PPMS can be seen. In figure 5.18a the two curves are shown normalised with regard to the respective value at 300 K. These curves overlap very well. The inset shows the absolute values. Their difference in the position of about 20 $\mu\Omega$cm could be caused by a mismeasurement of the sample dimensions. Figure 5.18b shows a slight deviation between the curves at low temperatures. This can be caused by instrumental errors in the cooling or heating process. The minimum at around 3.5 K can be seen in both curves.

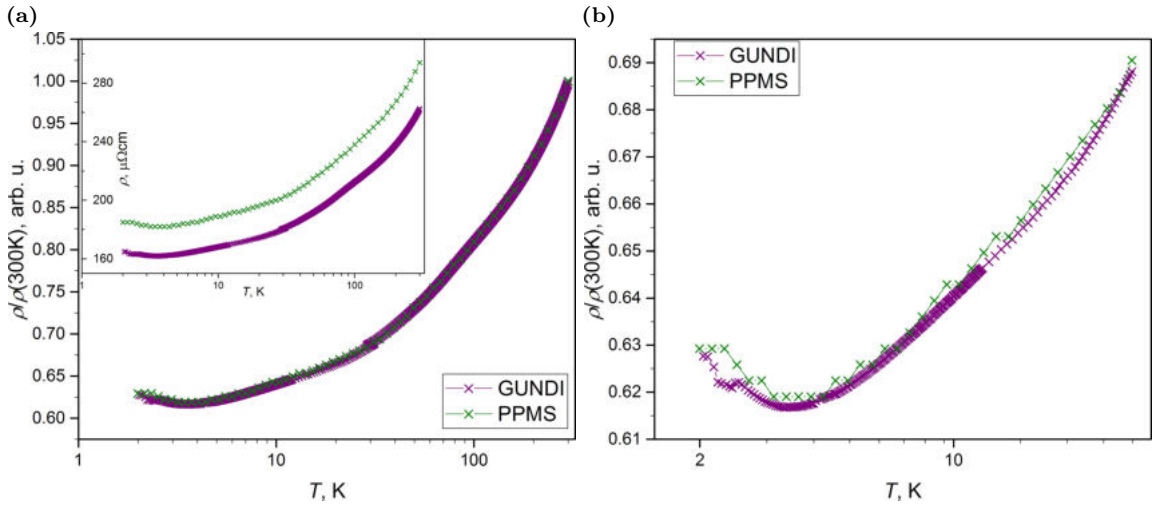

Figure 5.18: Resistivity curves of the CeBiPd sample CPB5b measured with two different techniques. (a) Temperature range $2 \leqslant T \leqslant 300$ with values normalised to values at 300 K; the inset shows the measured values. (b) A small deviation can be seen at the lowest temperatures.

In figure 5.19 the Hall resistivities are shown as a function of the magnetic field. For CPB5b it is slightly non-linear from 10 K downwards. For CPB7 the Hall resistivity is linear at nearly all temperatures. Thus the mobility can be estimated using a single-band model for both of the investigated samples.

The mobilities of the two samples are very similar. The charge carrier concentrations at low temperatures show a substantial difference which causes the discrepancy in the resistivity curves.

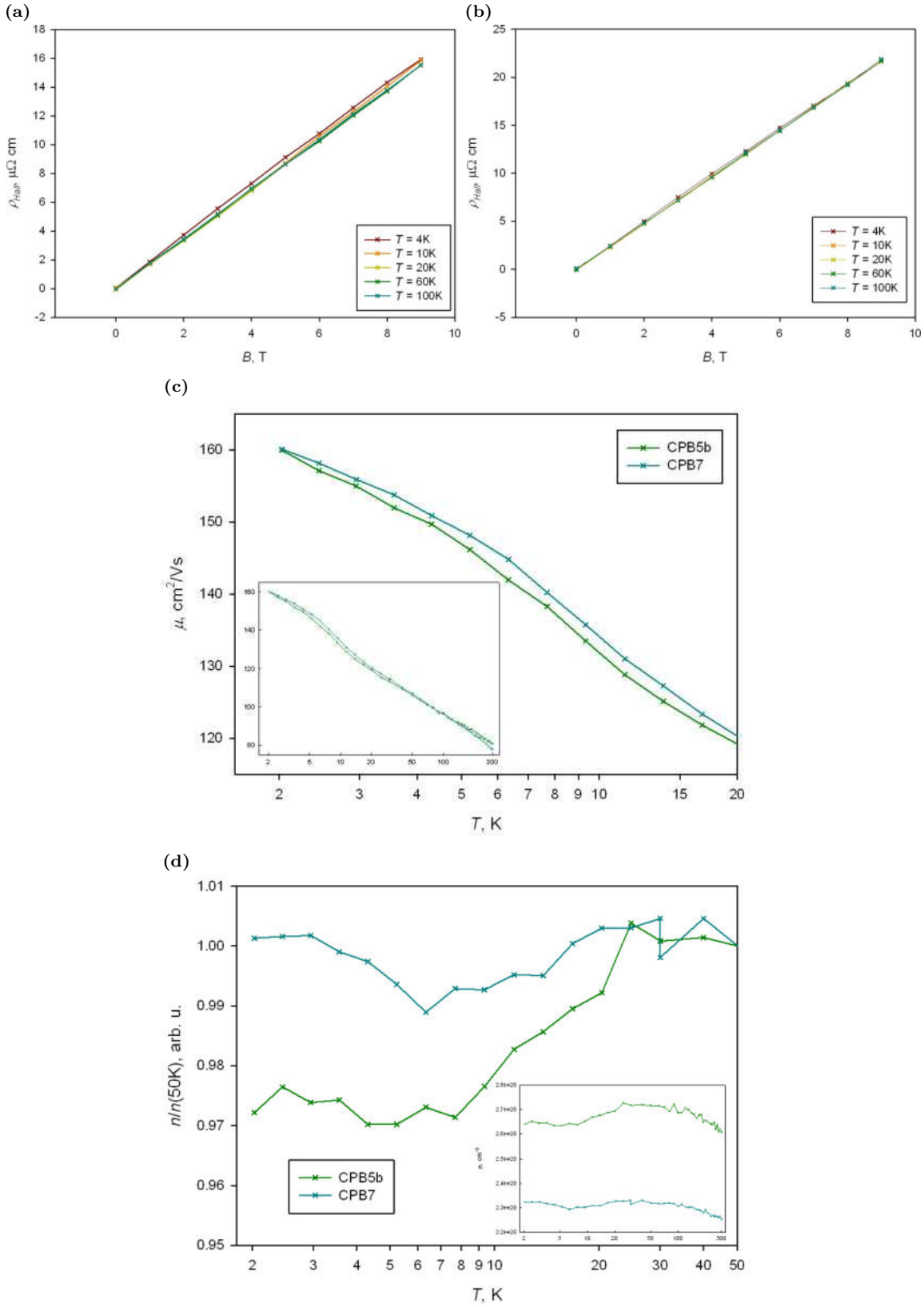

Figure 5.19: Magnetic-field-dependent Hall resistivity for the CeBiPd samples (a) CPB5b and (b) CPB7; (c) mobility of CPB5b and CPB7; (d) charge carrier concentrations of CPB5b and CPB7: The curves are normalised to the respective value at 50 K. The inset shows the curves with original values. The difference in the position of the curves is assumed to be caused by an imprecise geometric factor.

The two samples investigated here show different zero-field resistivities (figure 5.17) and charge carrier concentrations (figure 5.19d) at low temperatures. In table 5.3 their measured compositions can be seen. CPB7 has a much higher Pd:Bi ratio than CPB5b. However, the collection of more data is necessary for concise conclusions.

5.4.3 Magnetisation measurements

Two samples were used for magnetisation measurements in the Quantum Design PPMS: CPB5b, which shows a very smooth resistivity curve and CPB4c, which shows a significant kink in the resistivity.

When measuring the properties of CPB4c the sample was installed in such a way that the magnetic field was parallel to the [2 -1 0] direction in the crystal. It was oriented using Laue measurements (see figure 5.20).

The field-dependent magnetisation is linear above about 20 K (see figure 5.21a). Below that temperature the susceptibility becomes field-dependent. A saturation of the magnetisation could not be observed in the measurement range.

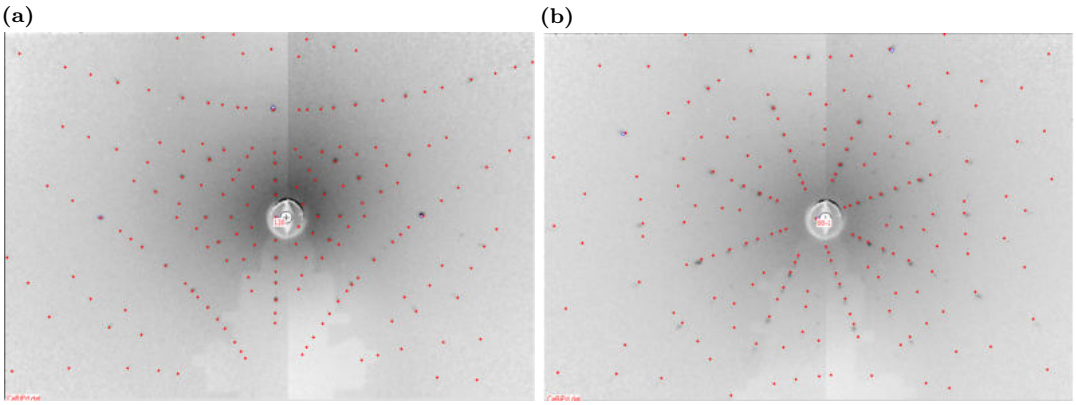

Figure 5.20: Laue pictures of the CeBiPd sample CPB4c in (a) [1 2 0] and (b) [0 0 -1] directions.

Susceptibility measurements with a variety of magnetic field strengths were performed on CPB4c. A summary of the susceptibility for magnetic fields between 1 and 9 T can be seen in figure 5.21d. The data for low fields ($\leqslant 3$ T) and low temperatures ($\leqslant 10$ K) can be found in figure 5.21c.

Above 4 K the susceptibility decreases steadily with increasing temperature. At the lowest field in figure 5.21c ($B = 0.05$ T) a peak is visible at about 3.4 K, which is approximately the same temperature at which the resistivity curve (figure 5.14) has a kink. This peak becomes flatter and moves to lower temperatures with increasing field. The slope of the curve between 3.4 and 10 K also becomes flatter with increasing field. The peak is gradually suppressed by the magnetic field. This behaviour suggests an antiferromagnetic transition.

Superconductivity can be investigated by applying a very low field to the sample. In figure 5.21b the susceptibility at $B = 100$ Oe is shown. A strong magnetic shielding effect due to the Meissner effect was not observed in the entire temperature range. Thus, the observed strong resistivity drop is unlikely to be related to bulk superconductivity.

The curve taken at 7 T in figure 5.21d shows a peak at around 60 K. This is most likely caused

by an amount of remaining oxygen in the measuring chamber.

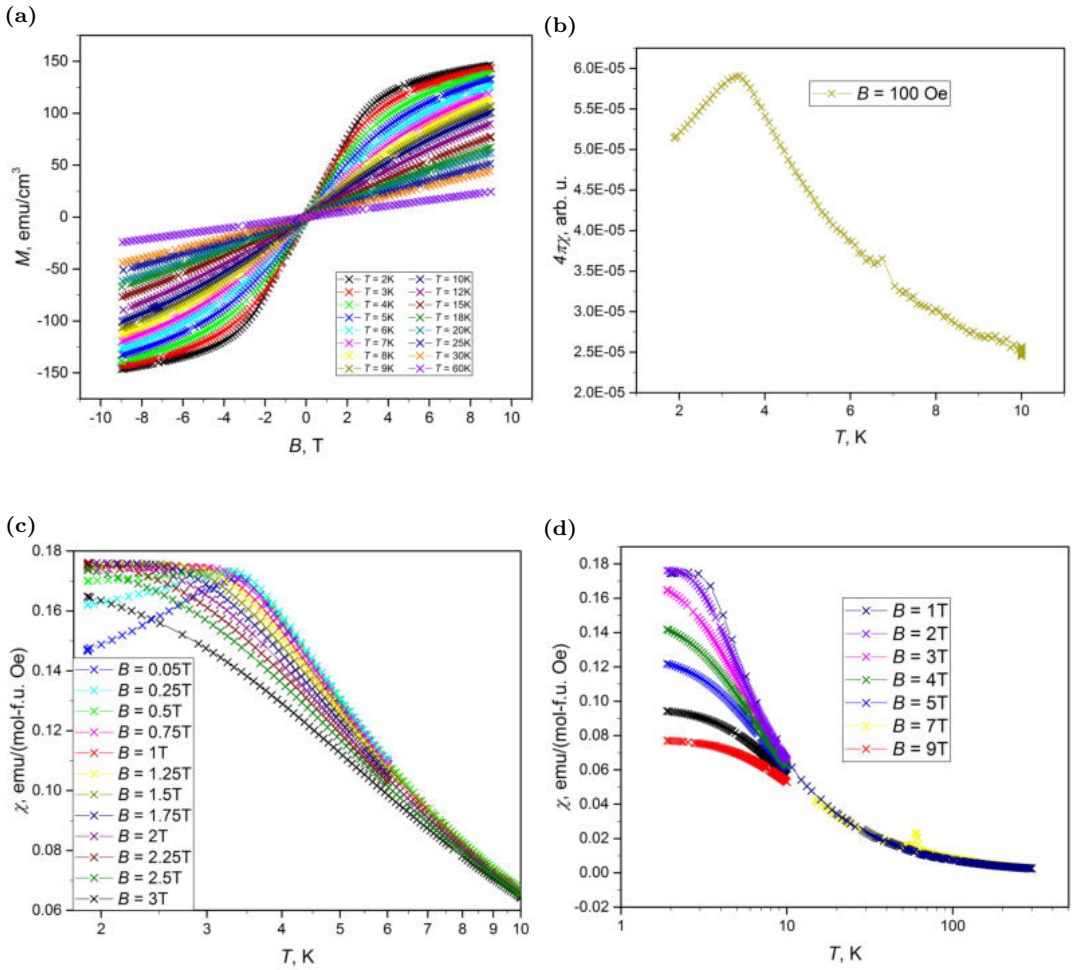

Figure 5.21: Magnetisation measurements of the CeBiPd sample CPB4c. (a) Magnetic field dependent magnetisation at different temperatures; susceptibility (b) at a very low magnetic field, (c) at fields $\leqslant 3\,\mathrm{T}$ and temperatures $\leqslant 10\,\mathrm{K}$, and (d) at fields $1\,\mathrm{T} \leqslant B \leqslant 9\,\mathrm{T}$

For CPB5b the magnetisation was analysed in the temperature range of 4 to 300 K (see figure 5.22b). The susceptibility shows a steady decrease with increasing temperature. The slope of the curve is also decreasing. At the lowest temperatures the susceptibility measured with an applied magnetic field of 2 T is lower than in the curves measured at lower fields. This behaviour matches the one observed in CPB4c. However, the presence of a peak at 3.4 K could not be verified due to the measuring range. The field-dependent magnetisation curve for $T = 10\,\mathrm{K}$ is shown in figure 5.22a.

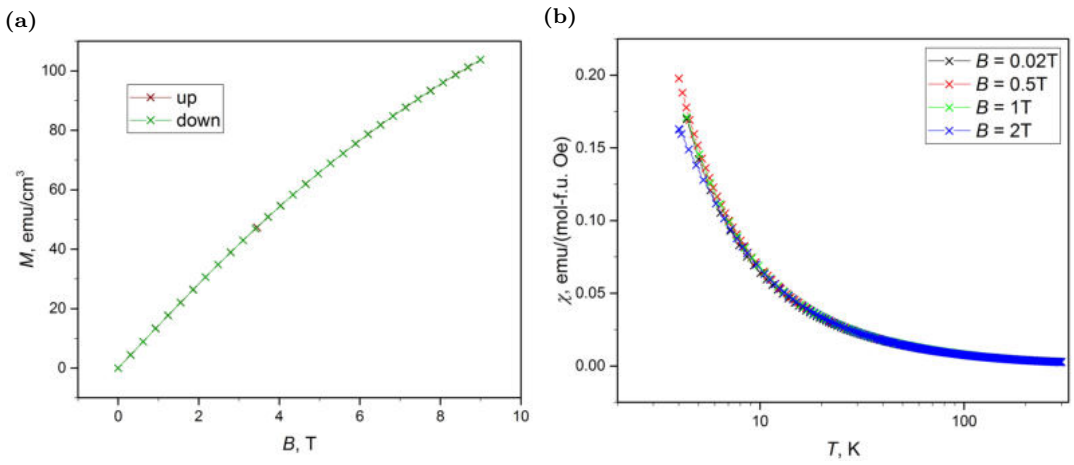

Figure 5.22: Magnetisation data of the CeBiPd sample CPB5b. (a) $M(B)$ at $T = 10\,\mathrm{K}$; the "down" curve was taken while decreasing the field and the "up" curve while increasing; (b) susceptibility in different magnetic fields.

The Curie-Weiss law

$$\chi(T) = \frac{C}{T-\theta} \quad \text{with} \quad C = \frac{N_A\,\mu_{eff}^2}{3\,k_B} \tag{5.1}$$

was fitted to the inverse susceptibility curve of CPB4c taken at a field of 1 T (see figure 5.23a). Since

$$\frac{1}{\chi} = \frac{T-\theta}{C} = \frac{1}{C}T - \frac{\theta}{C}, \tag{5.2}$$

a linear fitting function can be used to determine the Curie constant C (and thus the effective magnetic moment μ_{eff}) and the paramagnetic Néel temperature θ. However, C and θ are very sensitive to the range used for fitting. In a range of 100 to 175 K the parameters are computed to $C = 0.791\,\mathrm{K}\frac{\mathrm{emu}}{\mathrm{mol-f.u.\,Oe}}$, $\mu_{eff} = 2.52\,\mu_\mathrm{B}$ and $\theta = -5.412\,\mathrm{K}$. The negative θ suggests antiferromagnetic correlations in the sample. The value is similar to previously reported ones: $\theta = -5.1\,\mathrm{K}$ in [12] and $\theta = -5.8\,\mathrm{K}$ in [11].

For CPB5b the Curie-Weiss law was also fitted to the inverse susceptibility curve (see figure 5.23b) in a range of 100 to 175 K. The parameters are computed to $C = 0.794\,\mathrm{K}\frac{\mathrm{emu}}{\mathrm{mol-f.u.\,Oe}}$, $\mu_{eff} = 2.52\,\mu_\mathrm{B}$ and $\theta = -1.405\,\mathrm{K}$. While the C and μ_{eff} values agree well with the values of CPB4c, θ has a different value from the values presented above.

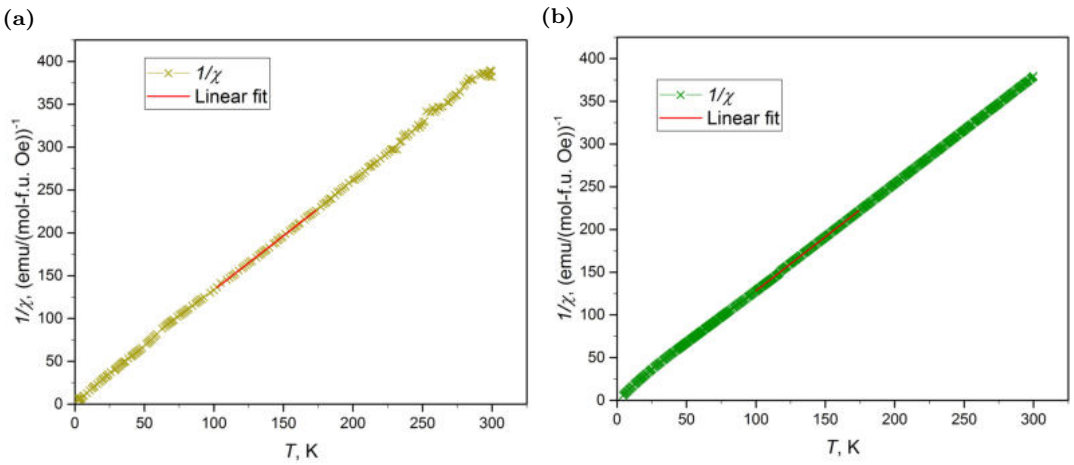

Figure 5.23: Curie-Weiss fits at $B = 1\,\mathrm{T}$ for the CeBiPd samples (a) CPB4c and (b) CPB5b

5.4.4 Heat capacity measurements

Two samples were selected, based on their resistivity curves, for heat capacity measurements – CPB1 and CPB4c. The measurements were conducted in a temperature range of approximately 0.4 K to 20 K. Both samples show a kink in the resistivity between 2 and 3 K. The heat capacity is a bulk sensitive property. Thus the behaviours seen here are most likely intrinsic properties of the material.

In figure 5.24 the heat capacity curve of CPB1 (sample weight 1.1 mg) is presented. It shows a strong peak around 2.2 K. Below the peak temperature the heat capacity rapidly falls down until the end of the measurement range. When turning on a magnetic field the peak flattens and moves to higher temperatures.

A peak in the heat capacity can be caused by a second order phase transition. Superconductivity leads to a different peak shape and is therefore ruled out, despite the sharp fall in the resistivity of CPB4c (see figure 5.25). It is more likely that this behaviour is caused by an antiferromagnetic transition.

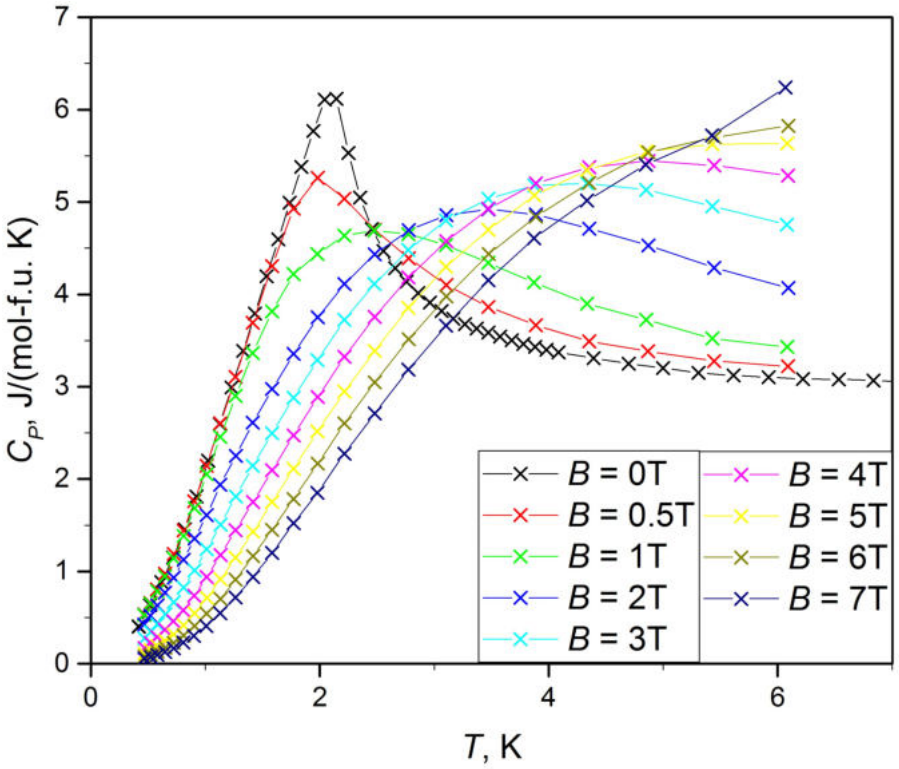

Figure 5.24: Heat capacity data for the CeBiPd sample CPB1

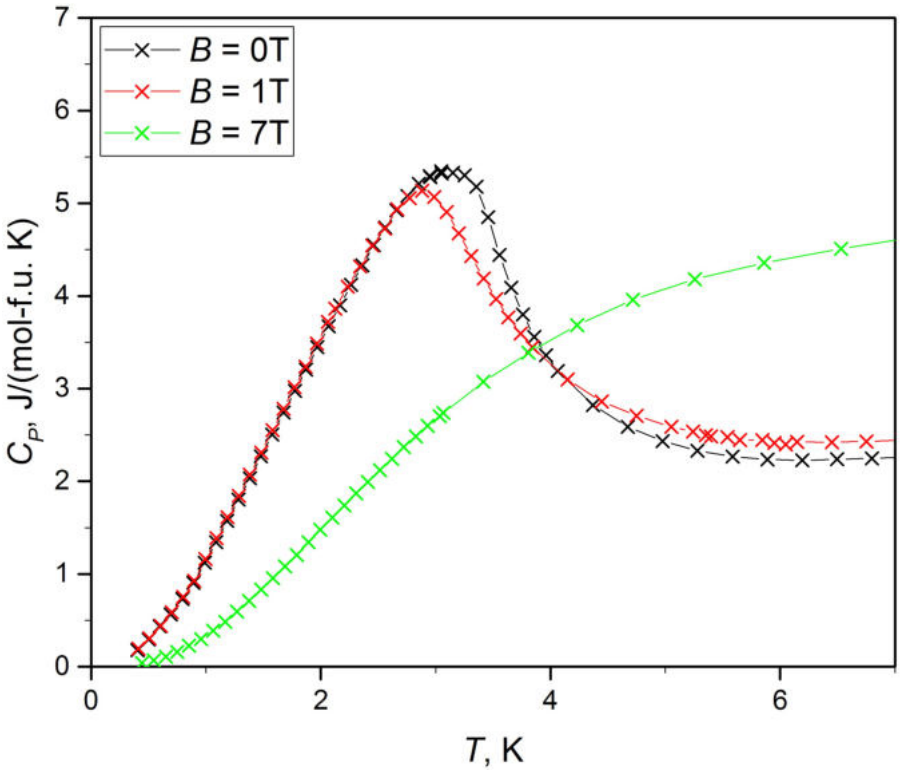

Figure 5.25: Heat capacity data for the CeBiPd sample CPB4c

In the CPB4c (sample weight 1.25 mg) curve a peak can be seen at approximately 3 K (see figure 5.25). Similarly to the CPB1 curves a high applied field flattens and moves it to a higher temperature.

The difference in the position of the peaks of the two samples suggests a high sensitivity of the transition temperature to small variations in the composition. In table 5.3 it can be seen that the relative Bi content differs in the two samples.

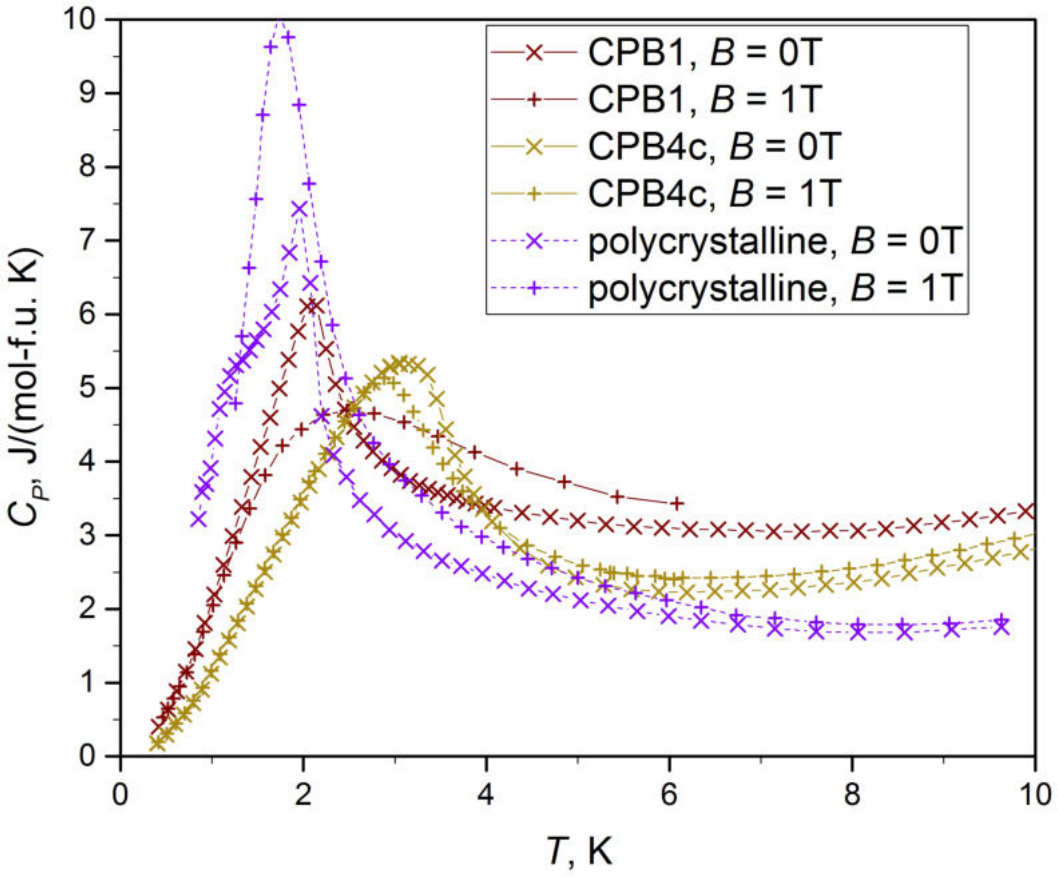

Figure 5.26: Comparison of measured heat capacity data with data of polycrystalline CeBiPd extracted from [9]

A polycrystalline sample of CeBiPd prepared by arc melting was investigated in [9]. The overall shape of the curve is comparable with the single crystal data. However, the peak of the curve taken at a magnetic field of 1 T reaches higher values of C_P than the one at 0 T, opposite to the behaviour observed in CPB1. A substantial difference is that in [9] a superconducting transition was discovered at 1.4 K which cannot be found in the data at hand.

5.4.5 Discussion

A kink or extremum was found in the resistivity of all CeBiPd samples at low temperatures. The origin of this phenomenon was studied with further measurements.

Superconductivity, which was reported in [9] for a polycrystalline sample, could not be confirmed here. Neither the susceptibility nor the heat capacity curves show a superconducting transition. Instead, evidence for an antiferromagnetic transition was found in both measurements. The phase transition temperatures differ between the samples as well as the measured property (resistivity, susceptibility or heat capacity). They thus appear to depend sensitively

on the composition. The differences in the resistivity at low temperatures can be seen to vanish with an applied high magnetic field for CPB5b and CPB7 (see figure 5.17c).

In table 5.4 the phase transition temperatures for the CeBiPd samples and their compositions are provided. No obvious correlation between the compositions of the samples and the characteristic points in the physical properties can be seen.

Table 5.4: Overview of the kinks and extrema as well as compositions of CeBiPd samples in the different physical properties at low temperatures (where available). For the resistivity either the GUNDI or the PPMS were used. The compositions were measured by EDX and are given in atomic ratios.

Sample	$\rho(T)$	$\chi(T)$	$C_P(T)$	Ce:Bi:Pd
CPB1	kink, 3 K (GUNDI) min, 2.7 K (GUNDI)		max, 2 K	1:0.98:0.96
CPB4c	kink, 3 K (GUNDI)	max, 3.5 K	max, 3 K	1:1.05:0.96
CPB5b	min, 3–4 K (GUNDI) min, 3–4 K (PPMS)			1:0.97:0.95
CPB7	kink, 2.7 K (PPMS)			1:0.86:1.14

5.5 A new microstructure in the Ce-Bi-Pd system

The sample batch CPB8 with an initial composition of Ce:Bi:Pd = 3:4:2.5 yielded a large crystal (CPB81) which at first glance looked like a single-phase crystal. The EDX results for the as-grown surface are shown in figure 5.27. In figure 5.27c the smooth as-grown surface of the crystal is shown. However, after polishing the crystal in preparation for physical property measurements the metallographic image showed two phases on one face of the piece. Laue pictures of the sample (see figure 5.27d) confirm that the sample is not single-crystalline.

The crystal was polished so that only one of the observed phases remained. Then resistivity and magnetisation measurements were performed.

The resistivity curve of CPB81 (figure 5.28) shows two kinks: one at about 21 K and one at about 3 K. Unlike in the other CPB samples the resistivity disappears completely below 3 K. In [9] a superconducting transition was reported for polycrystalline CeBiPd, however at a lower temperature than found here. At 5 T an upturn can be seen below 3 K. Curiously, this effect cannot be seen for any of the other field strengths. The Hall resistivity shows considerable nonlinearity at 20 K and below.

In the susceptibility (figure 5.29) an antiferromagnetic transition at approximately 25 K can be seen. At about 3 K another peak can be seen that shows a similar behaviour when exposed to a magnetic field as the corresponding peak in other CPB samples (see figures 5.21 and 5.22). The magnetisation data also show similarities with CPB4 and 5.

(a)

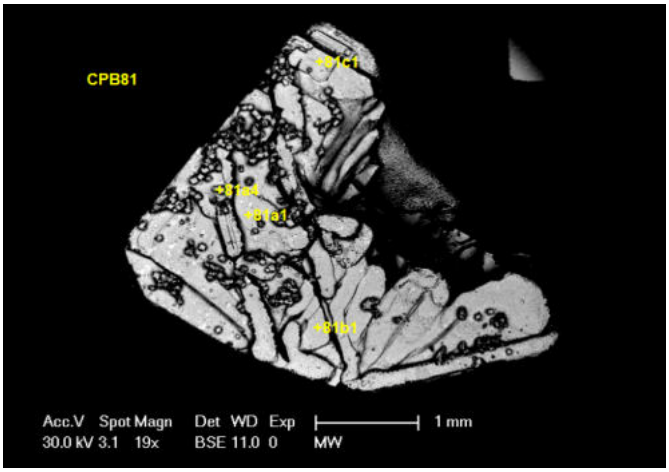

(b)

Measured point	Ce	Bi	Pd
a1	34.8	33.3	31.9
a4	34.1	36.8	29.1
b1	35.4	34.4	30.2
c1	34.8	32.9	32.3

(c)

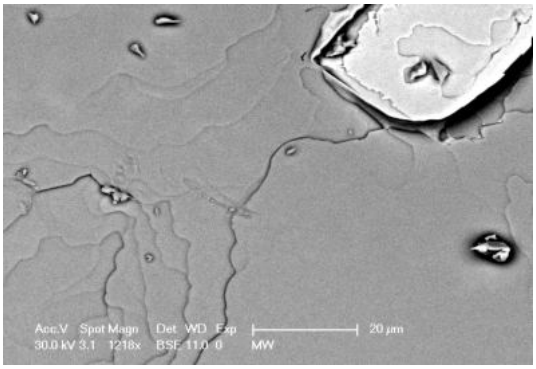

(d)

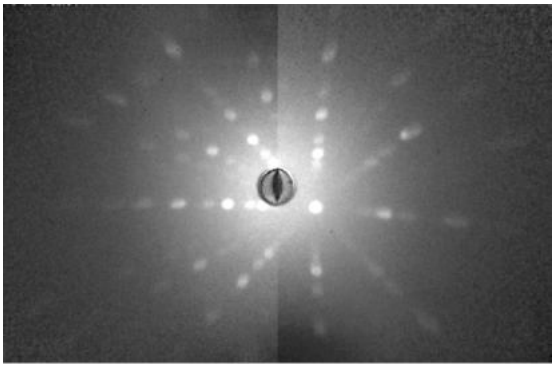

Figure 5.27: EDX and Laue investigations of the surface of the CPB81 crystal. (a) SEM image of the surface of CPB81, measured points are marked; (b) EDX measured compositions in atomic percent on the surface of CPB81 (the positions of the points are marked in (a)); (c) close-up SEM image of CPB81; (d) Laue picture of CPB81: The dots show the crystallinity of the sample and the light patch in the centre indicates that it is not single-crystalline.

(a)

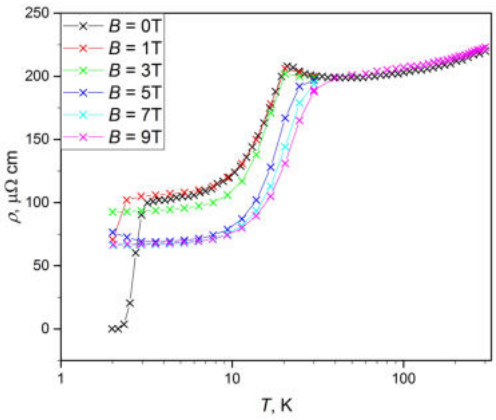

(b)

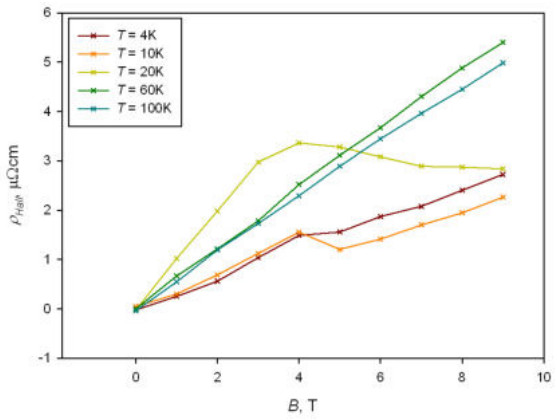

Figure 5.28: (a) Resistivity and (b) Hall resistivity of the CPB81 crystal

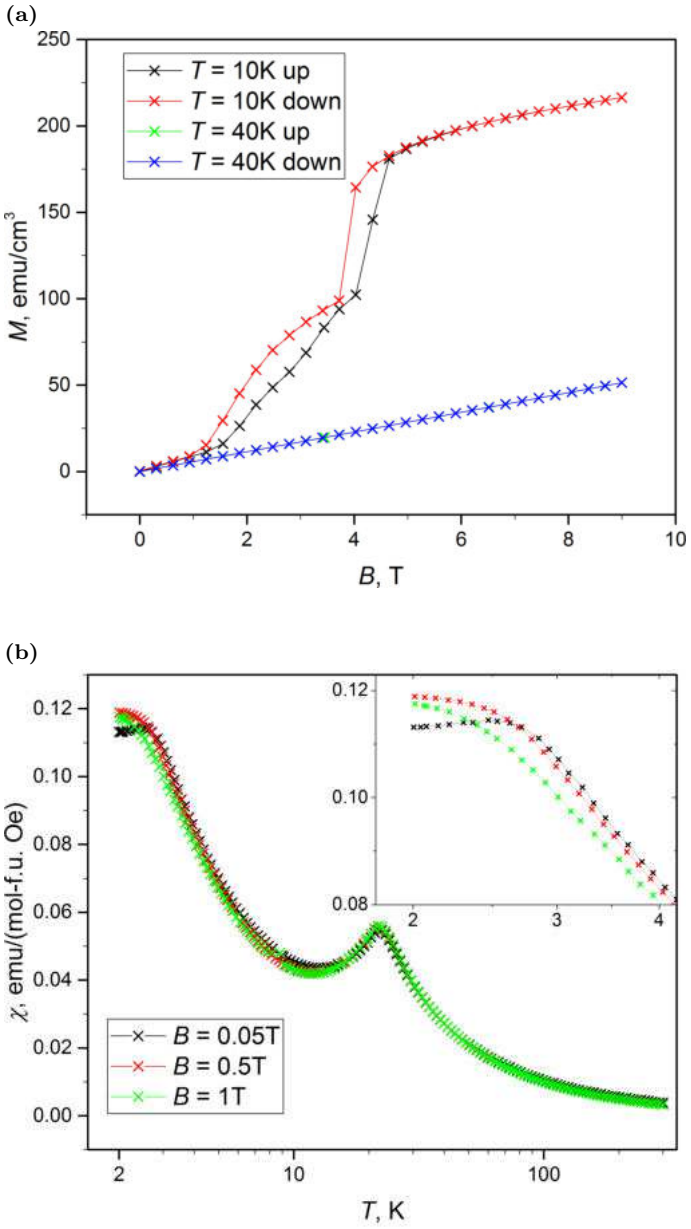

Figure 5.29: (a) Magnetisation of the CPB81 crystal; the "down" curves were taken while decreasing the field and the "up" curves while increasing. (b) Susceptibility of CPB81; the inset shows a magnification at the lowest temperatures.

Because of its unusual behaviour the sample was investigated with EDX (see figure 5.30a) once again. EDX measurements of the two phases in the two-phase region are presented in figure 5.30c. Due to the small phase areas and the relatively low resolution of the measurement method only an estimation of the phase compositions in the light (a2 and a4) and dark (a1 and a3) areas can be obtained. The measurements suggest that the light phase could be CeBi and the dark phase could be CeBiPd. The Pd observed in the light areas (a2 and a4) could be caused by the large measuring point (the minimum area is around 5 μm) which covers the light and the dark areas.

An EDX measurement was performed on a freshly split piece. The two opposite surfaces of

the split piece clearly show the same pattern of the structure. Thus, a contact with air could be ruled out as being the cause for the forming of two phases. In addition figure 5.30b shows that the microstructure is three-dimensional.

(a)

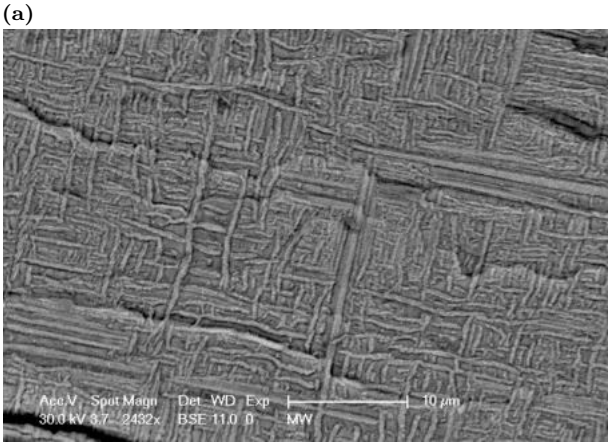

(b)

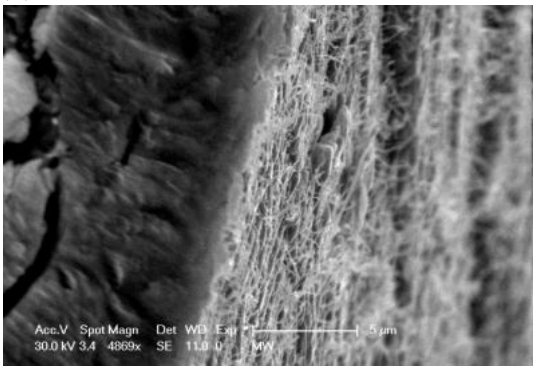

(c)

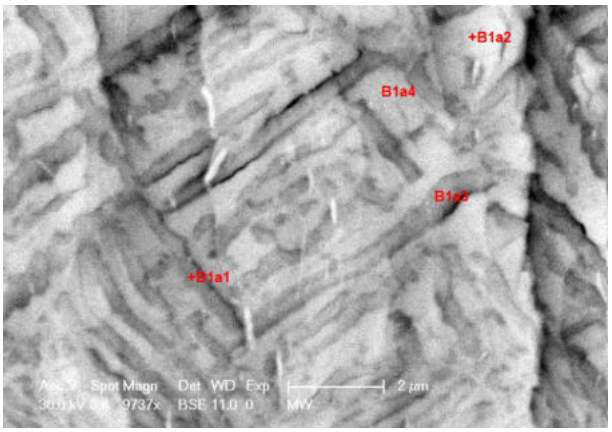

(d)

Measured point	Ce	Bi	Pd
a1	40.9	41.9	17.2
a2	44.9	45.2	9.9
a3	40.3	42.5	17.2
a4	45.2	46.5	8.3

Figure 5.30: EDX results for the CPB81 crystal. (a) SEM image of the microstructure of CPB81. (b) The right-hand part of the figure shows a surface with the visible microstructure from the side. The three-dimensionality of the structure can be seen. (c) Enlarged picture of the microstructure. The points indicated were measured with the aim to find the composition of each phase. (d) Measured compositions (in atomic percent) of the points shown in figure 5.30c. Percentages are only shown in relation to Ce, Bi & Pd. C and O were also measured on the points.

Following the results of the EDX measurement the physical properties were compared with those of the two phases CeBi and CeBiPd.

The kink in the resistivity at 25 K resembles a kink in the resistivity of CeBi, as shown in figure 5.31. Its behaviour in a magnetic field is also comparable. The kink at 3 K (see figure 5.28a) is at a similar temperature as kinks found in other CPB samples (see figure 5.14).

A comparison of the magnetisation of CPB81, CeBi and CPB4c is shown in figure 5.32. The shape of the CPB81 curve and magnitude of its values show characteristics of both underlying phases. The susceptibility of CPB81 shows an antiferromagnetic transition at a similar temperature as CeBi (25 K). Simultaneously, the continuous increase with decreasing temperature and the kink at 3 K in the susceptibility curve of CPB4c can also be found in CPB81. This is

shown in figure 5.33.

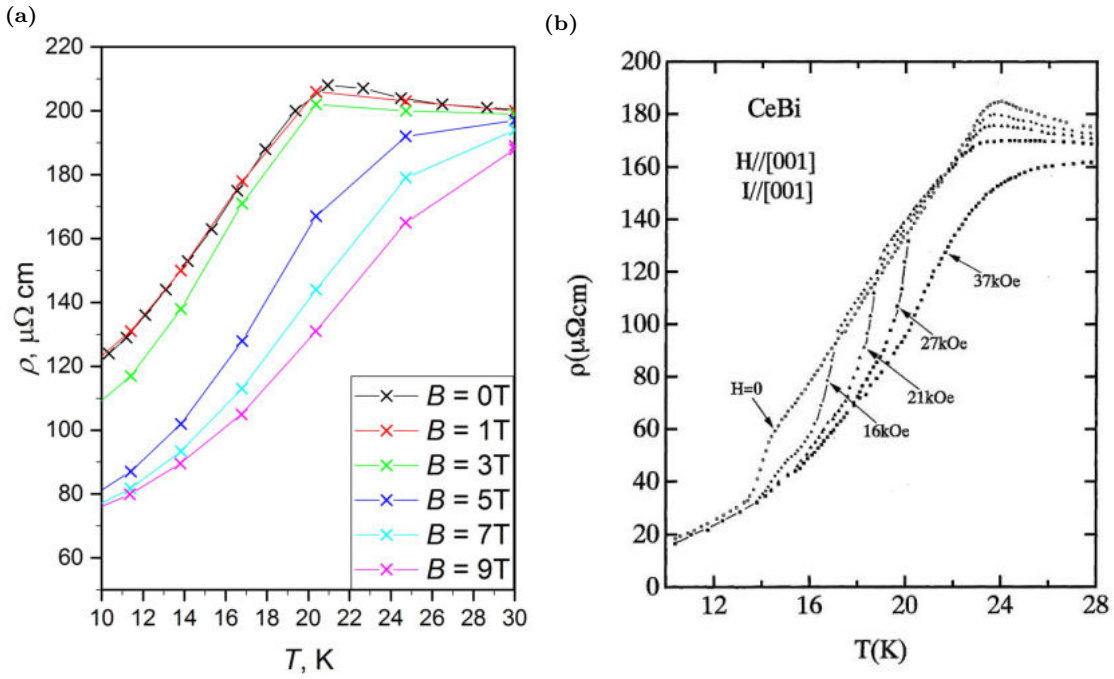

Figure 5.31: Resistivity of (a) the CPB81 crystal and (b) CeBi (figure taken from [33])

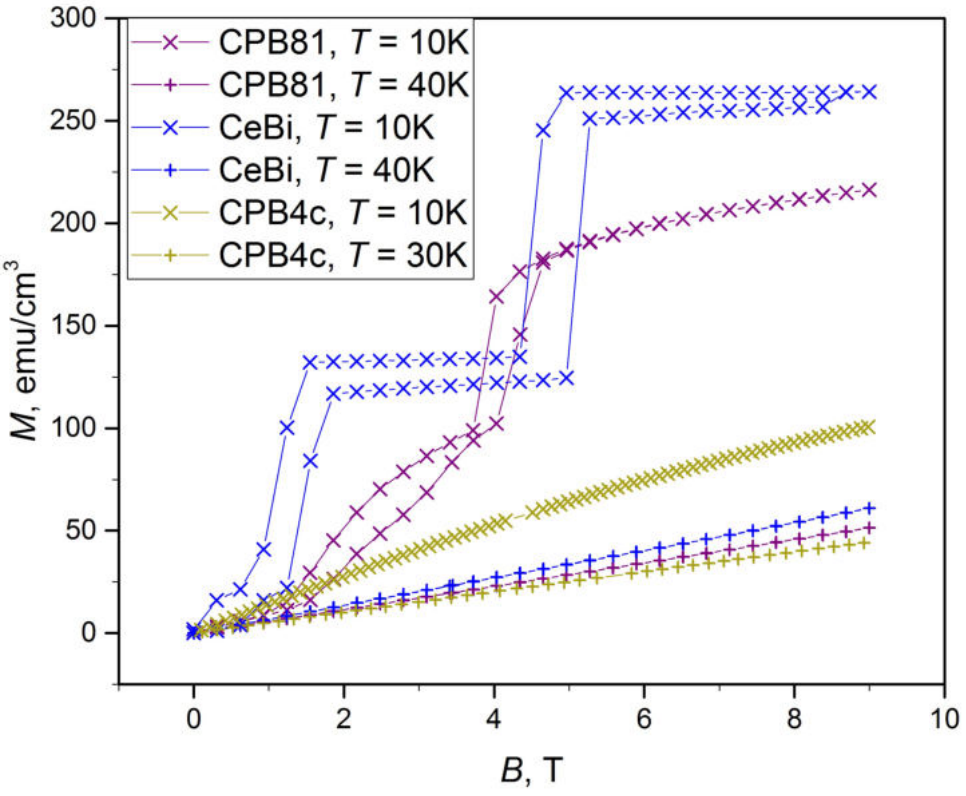

Figure 5.32: Magnetisation of the CPB81 crystal, CeBi and CPB4c at 10 and 40 K (30 K)

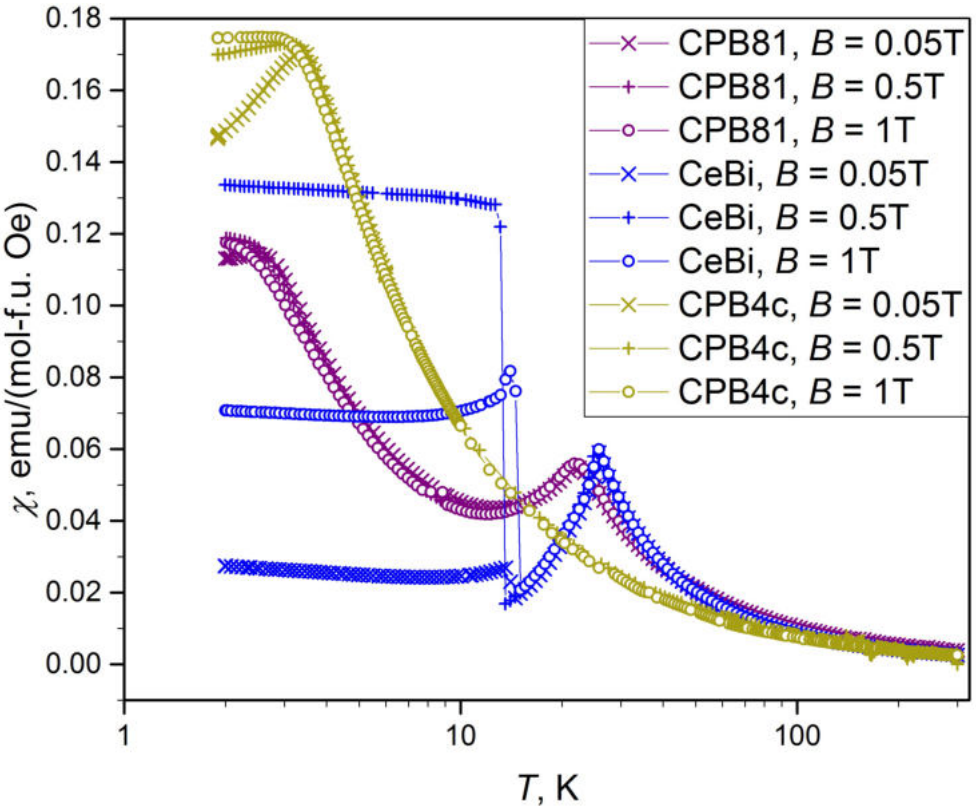

Figure 5.33: Susceptibility of the CPB81 crystal, CeBi and the CeBiPd crystal CPB4c with $B = 0.05$, 0.5 and 1 T

The XRD pattern (figure 5.34) confirms the presence of the two phases CeBi and CeBiPd. Rietveld refinement of the XRD pattern yields two different lattice parameters for the CeBiPd phase: $a_1 = 6.7969(6)$ Å and $a_2 = 6.7517(6)$ Å.

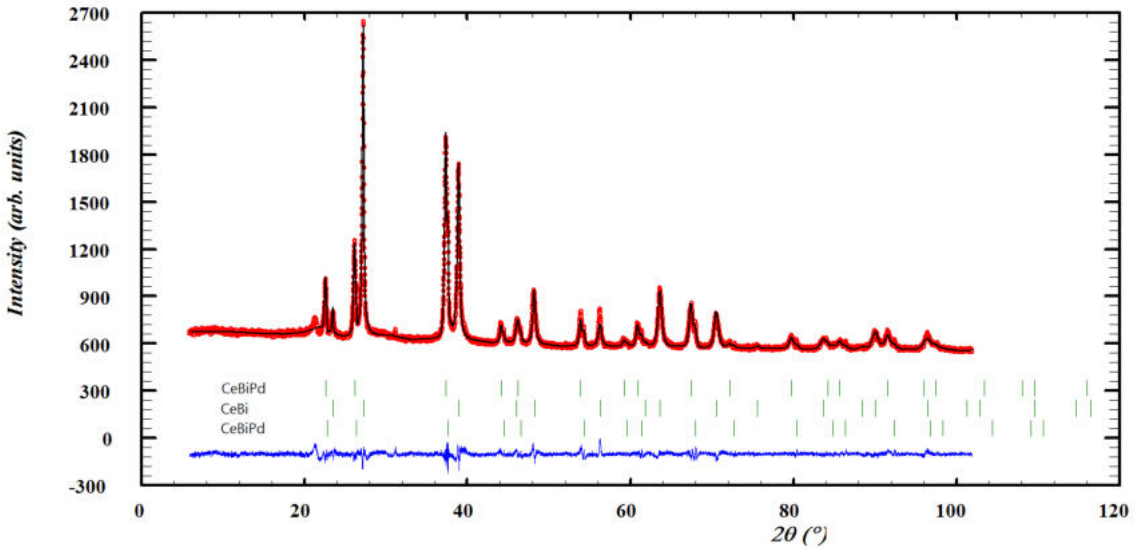

Figure 5.34: Refined XRD pattern of the CPB81 crystal

Another interesting feature of this material is that with time more and more so-called whiskers can be observed on the surface (see SEM image in figure 5.35a). Whiskers are protrusions with thicknesses typically in the micrometre range and lengths up to millimetres. They grow out of pure metal or alloy surfaces due to compressive stresses in the material [34]. Among the elements reported to show this behaviour are Bi [35] and Pb [36]. To find out which of these is the more likely element in these whiskers, EDX measurements were conducted (see figure 5.35b). Because the whiskers do not fulfil the SEM's requirements for size and other geometric traits several elements – also from the surroundings – were detected, but Pb was not among them. Out of the detected elements only Bi has been reported to spontaneously form whiskers. Therefore Bi is the most likely substance of the whiskers.

(a)

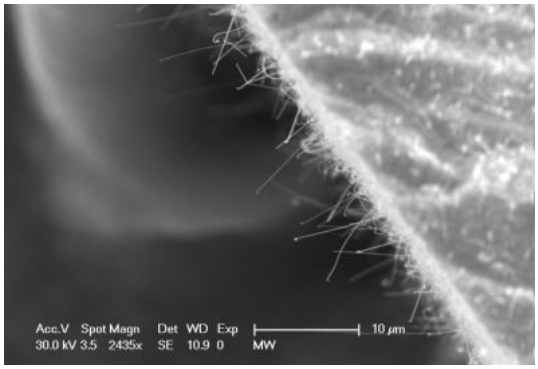

(b)

Measured point	Ce	**Bi**	Pd	C	O
wh1	0.35	**0.69**	0.12	83.75	15.09
wh2	0.16	**0.73**	0.03	83.11	15.97
wh3	0.16	**0.66**	0.03	87.24	11.91

Figure 5.35: (a) Whiskers grown on the surface of the CPB81 crystal after one week in a sealed and evacuated chamber. (b) Measured compositions (in atomic percent) of three individual whiskers. The measurement accuracy is very limited because of the very small size of the whiskers and the large size of the measuring point. This is also the reason for detecting C and O from the surroundings.

In order to investigate the growth of this new two-phase phenomenon three more samples were prepared with slightly different starting compositions (see CPB9, 10 and 11 in table 5.2). The resulting crystals were cut in half. EDX measurements of these surfaces show a varying ratio between areas of single- and of double-phase. CPB11 shows no double-phase region. The thickness of the CeBiPd coating is clearly dependent on the starting composition.

Two of the three previously measured CPB6 crystals also show two-phase areas in EDX measurements of the as-grown surfaces. As in all other samples that contain the two-phase compound the Bi content in the initial composition was set higher than the Pd content.

(a)

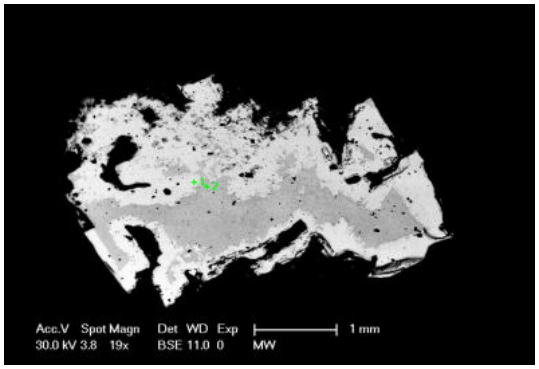

(b)

Measured point	Ce	Bi	Pd
1	36.6	36.3	27.1
2	42.9	41.8	15.3

(c)

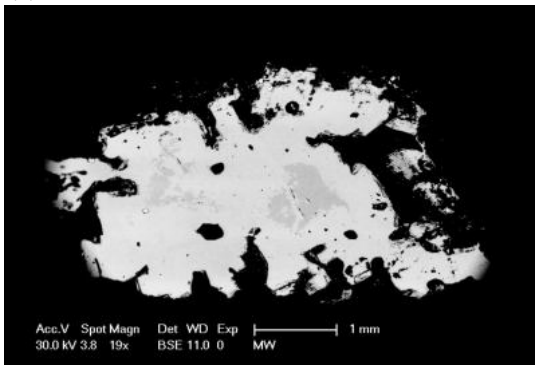

(d)

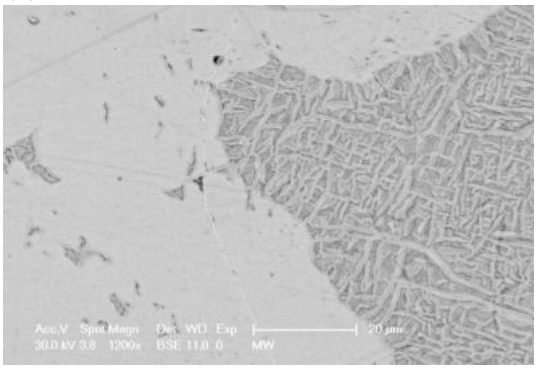

Figure 5.36: SEM images of (a) the CPB9 crystal with the measured compositions in (b), and (c) the CPB10 crystal (with detail in (d)) showing single- and two-phase regions

A sample (S4) with a similar Ce:Bi:Pd ratio as CPB9 was synthesised in the HF furnace. S4 had a Ce:Bi:Pd ratio of 3:4.2:3 and CPB9 of 3:4:3. Due to the different synthesis process of S4 no flux was required. Therefore the phase constitutions can be compared with respect to the influence by Pb.

In the XRD pattern of CPB9 (see figure 5.37) the two phases CeBiPd and Pb as well as a foreign phase are found. EDX measurements show the CeBiPd one-phase region and the two-phase region with CeBi and CeBiPd. Evidently the piece used for the XRD measurement did not contain the two-phase region. The XRD pattern of S4 shows the phases $Ce_3Bi_4Pd_3$, $CeBi_2Pd$ and CeBiPd. With EDX measurements $CeBi_2Pd$ and CeBiPd are found, among others (figure 5.38). CeBi is not detected in this sample.

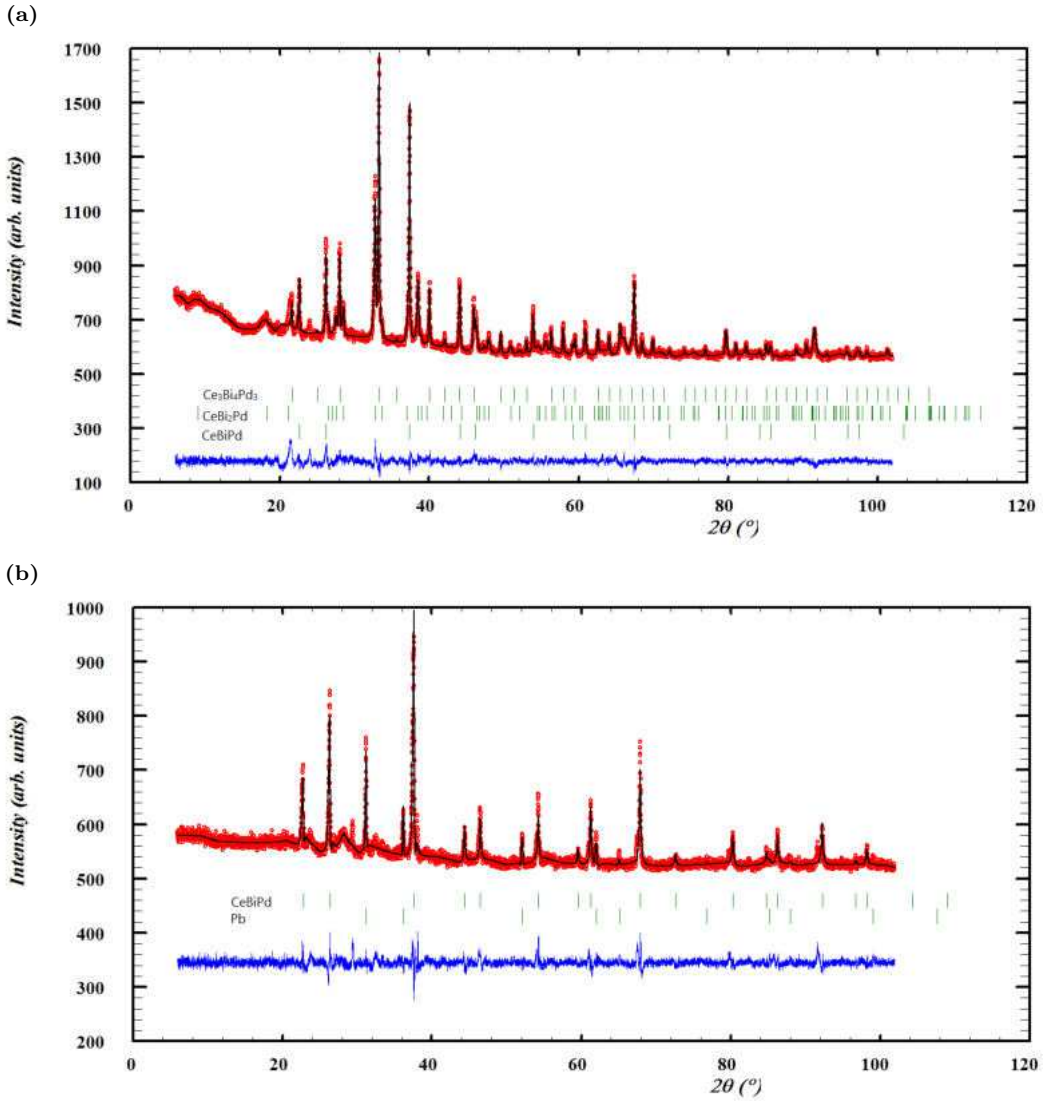

Figure 5.37: Rietveld refined XRD patterns of the samples (a) S4 and (b) CPB9

(a)

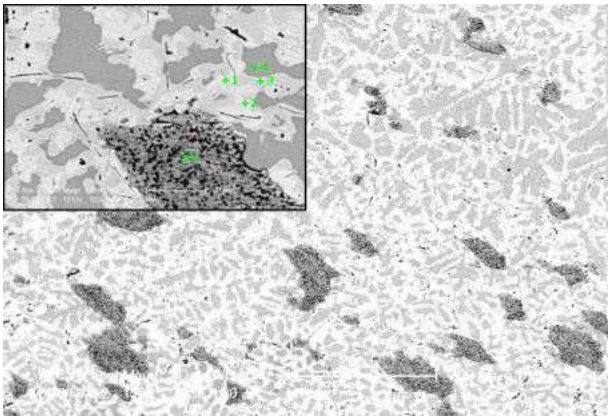

(b)

Measured point	Ce	Bi	Pd
1	15.8	48.1	36.1
2	24.2	49.2	26.6
3	30.4	39.5	30.1
4	34.3	35.2	30.5
5	11.7	34.7	53.6

Figure 5.38: EDX measurements of the sample S4. Point number 2 can be identified as $CeBi_2Pd$, number 3 as $Ce_3Bi_4Pd_3$ and number 4 as $CeBiPd_{1-x}$. (a) SEM image; (b) Phase compositions in atomic percent. The point numbers correspond to the points indicated in (a).

The sample synthesised without Pb flux does not include either the two-phase region or CeBi. Instead a large part of its volume is made up of $Ce_3Bi_4Pd_3$, which is close to the nominal composition, and $CeBi_2Pd$, besides CeBiPd. Therefore the formation of the newly found two-phase compound is possibly correlated with the presence of Pb during the growth process.

Another difference in the synthesis process between these two samples is the cooling rate. CPB9 was cooled slowly in order to facilitate equilibrium growth down to a temperature of 900°C. S4 was cooled rapidly and hence the phase composition is in non-equilibrium.

Concerning the question how this kind of crystal is stabilised we can only speculate. One possible growth mechanism could be the existence of a stable CeBiPd phase with Pd deficiency at a higher temperature which, when cooled, ceases to be stable. As a result CeBi grows along the planes of the existing crystal, leaving the latter with a high enough Pd concentration.

Another possibility is that CeBi starts crystallisation first at several sites. Then, at a lower temperature, CeBiPd is formed from the liquid which contains a high amount of Pd. Because there is liquid between the CeBi crystals an intergrown microstructure forms. At a sufficiently low temperature CeBiPd can form in a single phase from the remaining melt. This process could explain the outer layer of CeBiPd that is observed on samples with a low content of Pd in the initial composition.

Both of these scenarios imply that the composition of the CeBiPd phase changes with the temperature.

These scenarios are very rough sketches of two of many possible explanations for a complex process that has barely been investigated. Deeper studies of the growth mechanisms of single crystals can be made using for example differential scanning calorimetry.

5.6 Conclusion

In this part of this thesis several crystals of CeBiPd were synthesised using melt synthesis and flux growth. The melt synthesis was not successful in producing single phase alloys, but revealed the following valuable information. The EDX and XRD results suggest that there is no stable $CeBiPd_x$ compound with $x = 1.2$. A phase with $x < 1$ could be synthesised which suggests vacancies to be the major cause for variations in the Pd content. Furthermore, with varying Pd

content the phase region of CeBiPd was found to be narrower at temperatures around 900°C than at around 800°C.

The flux grown samples were investigated for various physical properties. A controlled tuning of the crystal compositions could not be reached, since there is insufficient knowledge about the ternary system of Ce, Bi and Pd and also about the crystal growth mechanisms. However, previous research about the material behaviour was expanded in the following ways.

A more precise study of the resistivity in consideration of the sample compositions showed a sensitive dependence of the physical properties on the ratio of the elements in the respective crystal, especially at low temperatures. Hall effect measurements suggest that this is caused by a change in the charge carrier concentration. When comparing the different samples it seems that an anomaly in the resistivity at about 3 K is an intrinsic property. Generally, the measured curves are similar to the results in the previous study [12]. Heat capacity and magnetic measurements suggest this behaviour of the resistivity to be caused by an antiferromagnetic transition. As opposed to studies of polycrystalline samples (see [9]) no indication of superconductivity was found.

A novel microstructure in this material system was discovered by using a high amount of Bi in relation to the amount of Pd in the flux growth. This structure is a combination of CeBiPd and CeBi.

A more detailed study of CeBiPd and its non-stoichiometric relatives could shed more light on the influence of the ratio between the elements on the physical properties, and thus also on the properties of the stoichiometric material. The complex behaviours expressed here in terms of incompletely understood measurement results are caused by several factors. They influence the crystal growth process as well as the response to outer conditions and still remain to be unravelled in future efforts.

6 Summary and outlook

In this thesis the synthesis and physical properties of the two intermetallic compounds $CeRu_4Sn_6$ and CeBiPd were studied. A brief summary of the most important findings will be presented here.

For $CeRu_4Sn_6$ single crystals of high quality were produced. One single crystal was grown by the floating zone method and subsequently annealed. The charge carrier mobility measured in this crystal was not substantially higher than in the measurement prior to the annealing.

A series of experiments was conducted to synthesise a single crystal by flux growth that had a size of at least 0.7 mm. This size was achieved by using a non-stoichiometric initial element ratio of Ce:Ru:Sn = 8.5:40:51.5 with a lead flux and a low cooling rate of 0.5°C/h. Preliminary measurements of the mobility, however, again do not reveal an increase compared to previous measurements. This suggests that the mobility might not be limited by defects. Further investigations are needed to confirm this conjecture.

In the course of the experiments with flux growth several flux materials were tested. Bi, In as well as mixed Sn and Pb flux did not produce crystals of the desired quality. In an attempt to increase the crystal sizes a step-wise cooling procedure of the liquid was tested but did not yield a high content of $CeRu_4Sn_6$.

Polycrystalline samples of CeBiPd were synthesised in the HF furnace. These samples were not single-phase, but their compositions gave valuable information guiding further synthesis experiments. It was found that CeBiPd with a higher amount of Pd than in the stoichiometric compound could not be produced. It was also concluded that CeBiPd with Pd deficiency has vacancies at the Pd site. At higher temperatures the phase region of CeBiPd is narrower with respect to the Pd content than at lower temperatures.

Based on this knowledge, a series of flux growth experiments was conducted to produce CeBiPd single crystals with varying Pd content. Due to sparse information available beforehand and the relatively narrow composition range of the series, the growth parameters could not be sufficiently well controlled to tune the composition precisely. In addition to the Pd content, also the ratio of Ce to Bi varied in the produced samples. However, some samples were selected for resistivity measurements. Due to the small amount of samples no clear correlation could be found between the composition and the resistivity.

Additionally, the magnetisation and heat capacity were measured on selected samples. A superconducting transition could not be confirmed but indications of an antiferromagnetic transition were found.

To achieve a full understanding of the interplay between composition and physical properties the synthesis has to be studied in even greater detail. A way has to be found to tune the synthesis parameters for precise control of the sample composition. Then a sufficiently large amount of samples must be selected to properly compare and determine clear influences on the physical properties.

A serendipitous finding in the course of this work was the synthesis of single-crystalline

$Ce_3Ru_4Sn_{13}$. The resistivities of two samples found of this compound were measured. The resistivity displayed considerably different temperature dependencies than a previously reported polycrystalline sample.

In the Ce-Bi-Pd system an interesting microstructure was observed unintendedly. It is comprised of CeBiPd and CeBi at the core of a crystal that was synthesised with an initial composition of Ce:Bi:Pd = 3:4:2.5. It was also found in other sample batches that were synthesised using a relatively high Bi:Pd ratio in the initial composition. The two-phase core was coated by a layer of single-phase CeBiPd. The physical property measurements of this material reflected the combination of the two phases.

In order to be able to synthesise ternary intermetallic compounds with high precision their respective phase diagram has to be known in more detail. A large but rewarding endeavour would be to systematically collect knowledge about the compounds in the ternary systems Ce-Ru-Sn and Ce-Bi-Pd.

List of Figures

List of Tables

Bibliography

[1] Sundermann M, Strigari F, Willers T, Winkler H, Prokofiev A, Ablett J M, Rueff J-P, Schmitz D, Weschke E, Sala M M, Al-Zein A, Tanaka A, Haverkort M W, Kasinathan D, Tjeng L H, Paschen S and Severing A, *$CeRu_4Sn_6$: a strongly correlated material with nontrivial topology*, Sci. Rep. **5** (2015) 17937.

[2] Xu Y, Yue C, Weng H and Dai X, *Heavy Weyl Fermion State in $CeRu_4Sn_6$*, Phys. Rev. X **7** (2017) 011027.

[3] Strydom A M, Guo Z, Paschen S, Viennois R and Steglich F, *Electronic properties of semiconducting $CeRu_4Sn_6$*, Physica B **359–361** (2005) 293–295.

[4] Brüning E M, Brando M, Baenitz M, Bentien A, Strydom A M, Walstedt R E and Steglich F, *Low-temperature properties of $CeRu_4Sn_6$ from NMR and specific heat measurements: Heavy fermions emerging from a Kondo-insulating state*, Phys. Rev. B **82** (2010) 125115.

[5] Paschen S, Winkler H, Nezu T, Kriegisch M, Hilscher G, Custers J, Prokofiev A and Strydom A, *Anisotropy of the Kondo insulator $CeRu_4Sn_6$*, J. Phys. Conf. Ser. **200** (2010) 012156.

[6] Hänel J, Winkler H, Ikeda M, Larrea J, Martelli V, Prokofiev A, Bauer E, and Paschen S, *Anisotropic Thermopower of the Kondo Insulator $CeRu_4Sn_6$*, J. Electron. Mater. **43** (2014) 2440–2443.

[7] Venturini G, Chafik El Idrissi B, Marêché J F and Malaman B, *Crystal structure and electrical properties of tetragonal YRu_4Sn_6*, Mat. Res. Bull. **25** (1990) 1541–1546.

[8] Pöttgen R, Hoffmann R-D, Sampathkumaran E V, Das I, Mosel B D and Müllmann R, *Crystal Structure, Specific Heat, and ^{119}Sn Mössbauer Spectroscopy of $CeRu_4Sn_6$: A Ternary Stannide with Condensed, Distorted $RuSn_6$ Octahedra*, J. Solid State Chem. **134** (1997) 326–331.

[9] Goraus J, Ślebarski A and Fijałkowski M, *Experimental and theoretical study of CePdBi*, J. Phys.: Condens. Matter **25** (2013) 176002.

[10] Makaremi N and Nourbakhsh Z, *Structural, Magnetic, and Electronic Properties and the Topological Phase of CePdBi Bulk and Nanolayers*, J. Supercond. Nov. Magn. **28** (2015) 2133–2141.

[11] Hermes W, Linsinger S, Mishra R and Pöttgen R, *Structure and properties of $Ce_3Pd_3Bi_4$, CePdBi, and $CePd_2Zn_3$*, Monatsh. Chem. **139** (2008) 1143–1149.

[12] Bissolo M, *Single crystal growth and physical properties of the half-Heusler phase $CeBiPt_{1-x}Pd_x$*, Bachelor's thesis, Fakultät für Physik der Technischen Universität Wien (2019).

[13] Tachibana M, *Beginner's Guide to Flux Crystal Growth* (Springer Japan; 2017) 23–41.

[14] Pritula I and Sangwal K, *Fundamentals of Crystal Growth from Solutions*, Handbook of Crystal Growth II (Second Edition) (Elsevier B.V.; Tokyo, 2015) 1185–1227.

[15] Changkang C, *Phase diagram and its application to the crystal growth of high T_C oxide superconductors*, Prog. Crystal Growth and Charact. **36** (1998) 1–97.

[16] Dąbkowska H A and Dąbkowski A B, *Floating Zone Growth of Oxides and Metallic Alloys*, Handbook of Crystal Growth II (Second Edition) (Elsevier B.V.; Tokyo, 2015) 281–329.

[17] Jenkins R and Snyder R L, *Introduction to Powder X-ray Diffractometry* (John Wiley & Sons, Inc.; New York, 1996).

[18] Young R A, *The Rietveld Method* (Oxford University Press; Oxford, 2002).

[19] Rodríguez-Carvajal J, *An introduction to the program FullProf 2000* (Laboratoire Léon Brillouin, France; 2001).

[20] Goldstein J et al., *Scanning Electron Microscopy and X-ray Microanalysis* (Springer Nature; New York, 2018).

[21] Schmidt P F et al., *Praxis der Rasterelektronenmikroskopie und Mikrobereichsanalyse* (Expert-Verl.; Renningen-Mannheim, 1994).

[22] Winkler H H, *Physical properties of the anisotropic Kondo insulator $CeRu_4Sn_6$*, Ph.D. thesis, Fakultät für Physik der Technischen Universität Wien (2013).

[23] Zhang J, Zhang S, Chen Z, Lv M, Zhao H, Yang Y, Chen G and Sun P, *Pressure effect in the Kondo semimetal $CeRu_4Sn_6$ with nontrivial topology*, Chin. Phys. B **27** (2018) 097103.

[24] Mishra T, Schwickert C, Langer T and Pöttgen R, *Ternary Stannides $RE_3Ru_4Sn_{13}$ (RE = La, Ce, Pr, Nd) – Structure, Magnetic Properties, and ^{119}Sn Mössbauer Spectroscopy*, Z. Naturforsch. **66b** (2011) 664–670.

[25] Gribanova V A, Синтез, кристаллические структуры и физические свойства новых интеметаллических соединений в тройных системах Ce-Ru-Sn, Ce-Ru-In, Sm-Ru-Sn, Ph.D. thesis, Faculty of Chemistry at the Moscow State University (2017).

[26] Eisenmann B and Schäfer H, *Käfigstrukturen in intermetallischen Verbindungen: zur Kenntnis von $LaRuSn_3$, $CeRuSn_3$, $PrRuSn_3$ und $NdRuSn_3$*, J. Less-Common Met. **123** (1986) 89–94.

[27] Winkler H, Lorenzer K-A, Prokofiev A and Paschen S, *Anisotropic electrical resistivity of the Kondo insulator $CeRu_4Sn_6$*, J. Phys.: Conf. Ser. **391** (2012) 012077.

[28] Guritanu V, Wissgott P, Weig T, Winkler H, Sichelschmidt J, Scheffler M, Prokofiev A, Kimura S, Iizuka T, Strydom A M, Dressel M, Steglich F, Held K and Paschen S, *Anisotropic optical conductivity of the putative Kondo insulator $CeRu_4Sn_6$*, Phys. Rev. B **87** (2013) 115129.

[29] Das I and Sampathkumaran E V, *Electrical-resistance anomalies in a Ce-Rn-Sn phase*, Phys. Rev. B **46** (1992) 4250–4252.

[30] Canfield P C and Fisk Z, *Growth of single crystals from metallic fluxes*, Phil. Mag. B **65** (1992) 1117–1123.

[31] Fukuhara T, Sakamoto I and Sato H, *Transport and magnetic properties of $RERuSn_3$ (RE = La, Ce, Pr, Nd, Sm): a heavy fermion compound $CeRuSn_3$ and a new valence fluctuating compound $SmRuSn_3$*, J. Phys.: Condens. Matter **3** (1991) 8917–8929.

[32] Ślebarski A, Goraus J and Witas P, *Electrical resistivity of the heavy-fermion-filled cage compound $Ce_3M_4Sn_{13}$ (M = Co, Rh, Ru) under high pressure*, Phys. Rev. B **92** (2015) 155136.

[33] Kasuya T, Sera M, Okayama Y and Haga Y, *Normal and anomalous Hall effect in CeSb and CeBi*, J. Phys. Soc. Jpn. **65** (1995) 160–171.

[34] Smetana J, *Theory of Tin Whisker Growth: "The End Game"*, IEEE T. Electron Pa. M. **30** (2007) 11–22.

[35] Stanley S A, Stuttle C, Caruana A J, Cropper M D and Walton A S O, *An investigation of the growth of bismuth whiskers and nanowires during physical vapour deposition*, J. Phys. D Appl. Phys. **45** (2012) 435304.

[36] Murakami M and Kuan T S, *Thermal strain in lead thin films V: Strain relaxation above room temperature*, Thin Solid Films **66** (1980) 381–394.